Development of a Thermal Management Methodology for a Front-End DPS Power Supply

Evan A. Sewall

Thesis submitted to the Faculty of the
Virginia Polytechnic Institute and State University
in partial fulfillment of the requirements for the degree of

Master of Science
In
Mechanical Engineering

Dr. K.A. Thole, Chair
Dr. E.P. Scott, Co-Chair
Dr. J. R. Mahan

October 11, 2002
Blacksburg, Virginia

Keywords: Power Electronics, Thermal Management, Cooling,
Experimental Verification, Radiation, Component Rearrangement

Development of a Thermal Management Methodology for a Front-End DPS Power Supply

Evan A. Sewall

Abstract

Thermal management is a rapidly growing field in power electronics today. As power supply systems are designed with higher power density levels, keeping component temperatures within suitable ranges of their maximum operating limits becomes an increasingly challenging task. This project focuses on thermal management at the system level, using a 1.2 kW front-end power converter as a subject for case study. The establishment of a methodology for using the computer code I-deas to computationally simulate the thermal performance of component temperatures within the system was the primary goal.

A series of four benchmarking studies was used to verify the computational predictions. The first test compares predictions of a real system with thermocouple measurements, and the second compares computational predictions with infrared camera and thermocouple measurements on a component mounted to a heat sink. The third experiment involves using flow visualization to verify the presence of vortices in the flow field, and the fourth is a comparison of computational temperature predictions of a DC heater in a controlled flow environment.

A radiation study using the Monte Carlo ray-trace method for radiation heat transfer resulted in the reduction of some component temperature predictions of significant components. This radiation study focused on an aspect of heat transfer that is often ignored in power electronics.

A component rearrangement study was performed to establish a set of guidelines for component placement in future electronic systems. This was done through the use of a test matrix in which the converter layout was varied a number of different ways in order to help determine thermal effects. Based on the options explored and the electrical constraints on the circuit, an optimum circuit layout was suggested for maximum thermal performance.

This project provides a foundation for the thermal management of power electronics at the system level. The use of I-deas as a computational modeling tool was explored, and comparison of the code with experimental measurements helped to explore the accuracy of I-deas as a system level thermal modeling tool.

Acknowledgments

Above all, I would like to thank God for getting me to where I am today and being the source of my strength. To Karen, my advisor, thanks for all the time, teaching, encouragement, and, most of all, patience you put into this project. Working with you this past year has been a joy and privilege. To Dr. Scott and Dr. Mahan, my advisory committee, thank you for all the help, positive comments and criticism, and for being patient while I struggled through both classes and research. To Pang, Dr. B, Dr. Odendaal, Peter, Bo, Wei, Qun, Francisco, Wu, Jonah, and Brandon at CPES, I really enjoyed working together with all of you. Thanks for all the help and input on this project. To the fellas in the lab: Jesse, Eric, Erik, Sachin, Chris, Dan, Andy, Mike, Will, Andrew, and Severin. Thanks for all the laughs and for making both working and putting off work together something to look forward to. To Lyle, thanks for coming up for a fun summer and putting up with plenty of late nights of me writing late in the lab. Finally, to Mom, Dad, and Hayden, thanks for all your encouragement and for always being there to support me in everything, even from so far away.

Table of Contents

Nomenclature

A =	Surface area of a component (Equations 3.1, 3.2, 4.2, 4.5)
A_i =	Area of emitting surface i (Equations 4.4, 4.6, 4.7, 4.13, 4.14)
A_j =	Area of absorbing surface j (Equations 4.6, 4.13)
A_1,A_2 =	Cross-sectional area of a plenum (Equation 3.3)
D_{ij} =	Total radiation distribution factor from surface i to j (Equations 4.12, 4.13)
D_{ji} =	Total radiation distribution factor from surface j to surface I (Equation 4.13)
D'_{ij} =	Total, diffuse-specular radiation distribution factor from surface i to surface j (Equation 4.14)
D'_{ji} =	Total, diffuse-specular radiation distribution factor from surface j to surface i (Equation 4.6)
F_{ij} =	Radiation exchange factor (Equation 4.4)
GBVF =	Gray Body View Factor used by I-deas (Equation 4.5)
Gr_L =	Grashof Number for a characteristic length L (Equation 2.2)
h =	Heat transfer coefficient (Equations 3.2, 4.3)
I / $I_{\text{Current Supply}}$ =	Current (Equation 3.4)
$i_{b,\lambda}(\lambda,T)$ =	Total, spectral intensity of a blackbody (Equation 4.9)
$i_{\lambda,e}(\lambda,T,\theta,\varphi)$ =	Directional, spectral intensity emitted from a surface (Equation 4.9)
k =	Thermal conductivity of a material (Equation 3.1)
k_{loss} =	Loss coefficient of an exit grill (Equation 4.6)
L =	Thickness of DC heater foil surface (Equation 3.1) / number of independent variables (Equation 3.8)
N_i =	Number of rays emitted from surface i in a ray trace calculation (Equation 4.12)
N_{ij} =	Number of rays emitted from surface i that are absorbed by surface j (Equation 4.12)

ΔP =	Pressure loss across a laminar flow element (Equation 3.7) / Pressure loss across an exit grill (Equation 4.15)
P =	Power dissipated by the DC heater surface (Equation 3.4)
q_{conv} =	Total heat removed from a component by way of convection (Equation 3.2)
q''_{conv} =	Heat flux transferred from a surface by way of convection (Equations 4.2, 4.3)
q'''_{gen} =	Total heat generated by a component per unit volume (Equation 4.2)
q''_{i} =	Net radiation heat flux emitted from surface i by way of radiation (Equation 4.8)
$q''_{i,a}$ =	Radiation heat flux absorbed by surface I (Equations 4.6, 4.8)
$q''_{i,e}$ =	Radiation heat flux emitted by surface I (Equations 4.7, 4.8)
q_{ij} =	Total heat transferred from surface i to surface j (Equation 4.4)
q''_{rad} =	Heat flux emitted from a surface by way of radiation (Equation 4.2)
Q =	Volume flow rate (Equation 3.7)
Q_{gen} =	Total heat generated by a component (Equation 4.1)
Q_{in} =	Total heat transferred into a control volume (Equation 4.1)
Q_{net} =	Total heat emitted by a surface by way of radiation (Equation 4.14)
Q_{out} =	Total heat transferred away from a control volume (Equation 4.1)
Q_{st} =	Total heat stored by a component (Equation 4.1)
R =	Electrical resistance / some function of x_i (Equation 3.8)
r_s =	Specularity ratio (Equation 4.11)
R_{Heater} =	Electrical resistance of DC heater surfaces
$R_{Precision\ Resistor}$ =	Electrical resistance of the precision resistor
R_{th_cond} =	Thermal resistance to conduction through a material (Equation 3.1)
R_{th_conv} =	Thermal resistance to convection away from a surface (Equation 3.2)
R_{Wires} =	Electrical resistance of DC heater wires
Re_L =	Reynolds Number based on a hydraulic diameter (Equation 2.2)
T_{air} / T_∞ =	Air temperature (Equations 3.2, 4.3, 4.15, 5.1, 5.2, 5.3)
$T_{Baseline}$ =	Baseline component temperature (Equation 5.2)
$T_{component}$ / T_{comp} =	Component temperature (Equations 4.3, 4.15, 5.1, 5.2)

T_{Cold} = Temperature of the lower temperature component as computed by I-deas (Equation 4.5)

T_{Hot} = Temperature of the higher temperature component as computed by I-deas (Equation 4.5)

T_i = Temperature of emitting surface I (Equations 4.4, 4.7, 4.14)

T_j = Temperature of emitting surface j (Equations 4.4, 4.6, 4.14)

T_{limit} = Operating temperature limit of a component (Equation 5.1)

T_{wall} = Temperature of the enclosure wall (Equation 3.2)

u = Overall uncertainty of a measurement (Equation 3.6)

u_{bias} = Bias uncertainty (Equation 3.6)

$u_{\Delta P}$ = Overall pressure measurement uncertainty

$u_{precision}$ = Precision uncertainty (Equation 3.6)

u_Q = Overall flow rate uncertainty

V = Voltage (Equation 3.4) / component volume (Equation 4.2) / air velocity (Equation 4.15)

x_i = The independent variable used for calculating uncertainties (Equation 3.8)

Greek:

ε = Total, hemispherical emissivity used in I-deas calculations (Equation 4.5)

ε_i = Emissivity of an absorbing surface j (Equations 4.7, 4.13, 4.14)

ε_j = Emissivity of emitting surface i (Equations 4.6, 4.13)

$\varepsilon'_\lambda(\lambda,T,\theta,\varphi)$ = Directional, spectral emissivity of a surface (Equation 4.9)

ρ = Total reflectivity (Equations 4.10, 4.11) / air density (Equation 4.9)

ρ^s = Spectral reflectivity (Equations 4.10, 4.11)

ρ^d = Diffuse reflectivity (Equations 4.10, 4.11)

σ = Boltzmann's constant (Equations 4.4, 4.5, 4.6, 4.7, 4.14)

List of Tables

List of Figures

Chapter 1 – Introduction

Power electronics have made their way into nearly every part of our lives. As computers approach smaller sizes and faster speeds at an unprecedented pace, they have been integrated into information technology systems, telecommunications systems, industrial motor drives, automobiles, aircraft, and many other areas common to our everyday lives. Each year, sales of power electronic electronics equipment exceeds $60 billion and affects another $1 trillion in hardware electronics sales (Lee, 2001).

This chapter introduces the motivation for this project. Section 1.1 describes the need for system-level thermal management. The next section is the literature search of past studies relevant to the project, and the chapter concludes with an introduction of the problem statement and project goals.

1.1 Background and Motivation

Most power electronic systems in use today are custom designed and built, requiring tremendous amounts of time and resources. The use of non-standard parts to produce custom-built electronic equipment results in high costs and poor reliability. Research at the Center for Power Electronics (CPES) at Virginia Tech has focused primarily on developing and implementing Integrated Power Electronics Modules (IPEMs) that could be readily applied to a variety of different applications eventually leading to standardization of power electronics systems. IPEMs are combinations of power electronics components, often with the gate drivers and controls included, in a single package. Active IPEMs include switching components such as power Insulated Gate Bipolar Transistors (IGBTs), while passive IPEMs consist of combinations of passive components such as integrated magnetic components and capacitors. The development of active and passive IPEMs involves combining power electronic components with the necessary controllers currently designed and implemented separately. Modular component construction bypasses many initial steps in design and

allows for time-effective and cost-effective solutions to many of today's power electronics needs.

The major roadblocks in power electronics integration involve more than just electrical design. Packaging and component placement take supreme importance as thermal, mechanical, and electromagnetic design are all considered. Component steady-state operating temperatures have been recognized as one of the most crucial aspects of component reliability. Figure 1.1 shows the breakdown of primary causes of failures in electronic equipment. Critical component overheating is seen as the dominant cause of electronics failures. As a result, thermal analysis is one of the most important aspects of power electronics design today.

Thermal design at the system level presents its own challenges. IPEMs will inevitably be implemented in a system, dissipating power alongside other components. Knowledge of the thermal impact of power modules on other system components is important in helping to determine the system's overall performance, since every component's operation is crucial to the system's effectiveness in performing its desired tasks. Components that may work well in an open, well-ventilated environment may be difficult to manage when placed in an enclosure with other power-dissipating components.

For thermal analysis, software packages using finite element methods to solve for multimode heat transfer such as conduction, convection, and radiation through integrated modules have been extremely helpful in understanding components' thermal performance before constructing prototypes. Thermal modeling at the system level can be extremely helpful, although it is currently not at the point of accurate predictions of real system component temperatures. According to Lasance (2001), "The situation when all computations at the system level can be used for accurate temperature prediction is still a long way off." Simulating a power electronics device at the system level includes much less detail and involves constructing larger computational models than in component-level simulations. System-level thermal analysis can be extremely beneficial, however. Knowledge of general temperature trends and comparisons, as well as knowledge of the flow field in an enclosure, can be extremely helpful in studying system reliability. Knowing approximate component temperatures relative to other components and being

able to select a layout from a number of configurations can allow a system designer to make great strides towards excellent thermal performance in a system.

The goal of this project was to lay a foundation for system-level thermal simulation. A front-end power supply was used as a case study for the computational studies and experiments, but the goal of proper operation of the power supply was secondary to the development of a computational methodology for thermal design. Understanding system-level packaging and the locations of critical components most likely to be operating near their temperature limits is extremely helpful in circuit design, as component placement can mean the difference between proper functionality and failure. In addition, being able to computationally simulate component temperatures with confidence would allow system designers to push thermal limits and estimate the reliability of the components within the system.

The availability of accurate design tools and knowledge of thermal effects will lead to more time-efficient designs, which will constantly push the limits towards smaller, more powerful systems. Advanced design tools will also lead to more cost-efficient designing as the front-end financial investment required for costly system design is reduced.

This project was focused on power electronics computational thermal modeling at the system level. Using finite element software, a geometric model of an electronics system was modeled, simulated, and studied. The accuracy of modeling the thermal operation of the actual system was explored through several benchmarking studies. Experimental and computational data for both the flow field and component temperatures were used for quantitative and qualitative comparisons of computational predictions at the system level.

The circuit designers established the baseline component layout on the basis of including all circuit components into the given enclosure. Very little consideration, other than the inclusion of a pair of heat sinks, was given to the thermal design. A study was performed in this project in which this layout was varied seven times to study the effect changes in the flow field had on component temperatures. This study helped to obtain general thermal design guidelines useful to any electronics engineer developing a similarly sized system.

1.2 Literature Search

A search of the literature revealed many thermal studies in electronics. A few papers directly addressed the issue of modeling accuracy as it applies to electronics temperature prediction, and those papers are compared in this section. In addition, a number of studies mentioned experimental verification of computational predictions of electronic systems not related to this project. A discussion of experimental comparisons with these component predictions follows. Finally, two papers discussing component placement optimization are introduced along with mention of their applicability to this project.

A number of papers described innovative cooling methods, both in air cooling as well as liquid cooling systems. Though alternative cooling methods were not explored in this project, several references to papers describing new heat sink designs, state-of-the-art cooling techniques, and advances in liquid cooling are listed in Appendix A.

System-Level Modeling Issues

Modeling a power electronics system at the system level presents a number of challenges. These challenges have been summarized and addressed by three papers. A paper by Lasance (2001) introduced a number of topics regarding the difficulties of modeling a real system at the system level. Lee (1994) discussed the computational modeling of a computer system enclosure and the methodology used to address many of the system-level issues. Two papers written by Grimes and others (2001) addressed the modeling of cooling fans and fan flows. Each of these authors introduced modeling difficulties and offered suggestions on how the challenges were faced.

Lasance (2001) presents an all-inclusive discussion of experimental and computational comparison of thermal performance at the system level. A discussion of the complex physical phenomena that dominate the heat transfer effects and the lack of accurate component input parameters and boundary conditions results in several suggestions for accurate system-level modeling. Multigrid techniques, local zooming,

and other refinement algorithms are suggested for grid construction because of the unrealistically high number of cells needed to accurately capture the cooling effects in the entire system. Radiation studies are usually inaccurate because of inaccurate component surface properties and the presence of specular surfaces, which are not usually considered in radiation analyses. Uncertainty from both convection from the printed circuit board (PCB) and the modeling of exit vents is not understood very well, and further research is suggested. Finally, fan modeling is able to predict the formation of a flow field reasonably well, according to Lasance, but local heat transfer coefficients based on velocities local to components are still difficult to predict.

Many of the same issues were addressed seven years earlier in an experiment performed by Lee (1994). A computational fluid dynamics (CFD) study using Flotherm (Flotherm, 1994) was performed on a computer system enclosure containing six 37-W PCBs. The computational predictions were discussed and then compared to experimental results. Lee addressed vent modeling by estimating a loss coefficient to define a pressure drop across the vent leading to a constant external static pressure boundary condition. According to Lasance (2001), the accuracy of this technique has not yet been explored or verified. One case was simulated with the addition of fan swirl to determine the effect of modeling swirl in the system, and this technique showed no improvement in the temperature prediction capability of the code. The experimental temperature measurements of the air immediately above the boards and computational comparisons to those experiments were shown to agree very well. Over a range of temperature rises from 24° to 44°C, the closest comparisons were within a single degree, while the largest error was seen as a difference of 7°C between a temperature prediction and thermocouple measurement.

A paper by Grimes and others (2001) focused on the computational accuracy of modeling the cooling fans in a system. Flotherm simulations were compared to smoke-wire velocity measurements in a system. Results showed that the manufacturer's fan curve slightly over-predicted the flow rate for the entire range of operating conditions. CFD comparisons revealed that predicted flow directions matched experiments. The magnitudes of the velocities, however, were not predicted well. This is consistent with a description by Lasance (2001) on fan prediction capability: "While the flow field can be

predicted reasonably well in some applications, accurate prediction of the local heat transfer coefficients is out of the question."

Finally, in a meeting with Dr. Van Wyk (2002), an Electrical and Computer Engineering professor at Virginia Tech, the issue of power losses was discussed. He stated that the difficulties of accurately modeling system-level temperatures are increased when the uncertainty in power losses is taken into consideration. According to Dr. Van Wyk, the predicted power losses for a circuit could vary by as much as ±40% (Van Wyk, 2002)! The possible error in power losses in AC systems makes both accurate prediction and benchmarking difficult, and it provides motivation for benchmarking simulations with controlled power losses.

Predictions and Measurement Comparisons

In verifying computational accuracy, a number of experiments have been performed to benchmark computational models. Many of the studies presented in the literature differ from the converter studied in the present effort but still faced the challenge of accurate modeling of electronics and comparisons with experiments. A total of five papers in this section are discussed with comments referring to the difficulties outlined by Lasance (2001) and Lee (1994) in the previous section.

Liang (2002) and others introduced a discussion of board-mounted power (BMP) modules, which convert power from a 48-V or 24-V bus to the load-level voltages in computer or telecommunication applications. The purpose of the paper was to explore the advantages of open and potted (enclosed) modules. Flotherm temperature predictions were compared with experimental wind tunnel experiments. Computational and experimental results disagreed slightly, with differences ranging from 5°C to 10°C, but the measurement trend over the range of flow rates was consistent, as shown in Figure 1.2. Lasance (2001) explained that predicted temperatures are higher than measured temperatures in most situations because of grid resolution and boundary layer modeling. That point is observed in the BMP comparisons. Good agreement between measurements and predictions can be claimed in the comparison shown in Figure 1.2, but temperature comparisons are not exact, which may in part be expected due to inherent uncertainties.

A paper by Gusev (2000) outlines the results of development and tests of a mini radioisotope thermal generator (RTG), which is a milliwatt power source (PS). Electrical equivalents (EE) were measured and considered to be equal to the power losses, which were shown to be a function of component temperature. The losses measured experimentally were no more than 15% higher than the losses calculated from analytical calculations using electrical efficiency, physical properties, and component dimensions.

Zhang (1997) compared experimental and computational temperature measurements on an external 36-W AC/DC adapter and battery charger for a notebook computer. The paper outlines the Flotherm CFD simulations of the module and the experimental temperature comparisons. In this case, the predicted temperatures were less than the experimental values by no more than 10%. Reasons given for the temperature discrepancy were uncertainty in the physical properties of materials, lumping components together for simplicity, and the restriction of geometry within the software.
The trend of comparisons over a range of designs, however, agrees very well, as shown in Figure 1.3, which is a comparison of the predictions and measurements of the transformer core temperature. No mention was made on how the computational simulations were set up in Flotherm or how the temperature measurements were taken. The simulation of radiation effects was mentioned, however. Flotherm uses an automatic view factor calculator to find view and exchange factors. The user identifies which surfaces are involved in the radiative exchanges, and the Flotherm Exchange Factor Calculator determines the view and exchange factors, taking into account multiple reflections, shading, and automatic surface subdivision. Though radiation was included, temperature comparisons still showed slight discrepancies, indicating that radiation is not the only effect causing inaccuracy in the computational predictions.

Lall (1998) also compared experimentally measured temperatures to computational predictions for a unit dissipating 744 W. For measured temperature rises ranging from 70°C to 80°C, agreement was shown to be roughly within 4°C to 10°C. This was another situation in which the experimental measurements were consistently lower than the calculations based on CFD results.

A study of the thermal performance of a three-phase squirrel-cage induction motor fed by asymmetrical power supply voltages was discussed by Fernandez and others

(1998). A two-dimensional finite element formulation was used to predict the solid temperatures with convection correlations used to calculate the convection heat transfer. The error reported between measured temperatures and calculated temperatures was between 0.1°C and 17.6°C for approximate temperatures rises of 100°C.

The papers described in this section were typical of many contemporary thermal analysis papers in which computational predictions claim good agreement with experimental results. Varying amounts of detail were considered in each experiment, and small uncertainties overlooked in any experiment could cause errors in the results. The goal of each of the five projects mentioned above was other than that of studying the comparison between computations and experiments. Only one of the papers mentioned accounting for radiation effects, indicating that ignoring radiation effects is a common practice in electronics thermal modeling. These papers do show that good agreement can be obtained between predicted and measured results, and trends in design changes often show excellent agreement.

Component Rearrangement and System Thermal Enhancement

This project was focused on the thermal analysis of a front-end power supply constructed with discrete components. The motivation to explore component placement for improved thermal performance prompted a comparison of several different layouts. No studies of this kind were found in the literature. Two optimization studies were performed on component placement, however, but the approaches of these projects were different than the methodology of the current project.

In the first paper, Humphrey (1992) and others described the development of a computer-assisted research methodology for finding the optimal locations of N heated components inside a larger ventilated enclosure. The paper outlines the infant stages of an optimization program that searches for the optimal placement of components given a set of constraints. This study would be extremely difficult and time-consuming to apply to the converter being studied currently because of the number of components involved. The complexity of the system in the present effort and the number of components to consider in the converter makes a mathematical comparison and optimization study extremely difficult to attempt.

A second paper, by Queipo (1998), discussed the use of genetic algorithms to solve flow and heat transfer equations in search of optimal or near-optimal solutions for the minimization of the failure rate of the system of components due to thermal overheating. The maximum temperatures of several equally spaced components on a printed wiring board (PWB) were optimized. Using the appropriate boundary conditions, the conservation equations of mass, momentum, and energy could be solved to find the desired temperatures. The use of genetic algorithms was an extremely effective optimization tool for the project described in the paper, but the detail and complexity of the front-end converter and the number of arrangement possibilities coupled with the number of component temperatures to consider in the converter operation does not make it a likely candidate for genetic algorithm optimization. Simulating a significant number of possibilities would be difficult, as solution times for the front-end converter computations often exceed six hours in a single simulation.

1.3 Problem Statement

Trends towards digital telecommunications and computer systems have led to modular designs requiring extremely low voltages and high currents. A widely accepted power conversion architecture for this type of system is the distributed power system (DPS). The DPS architecture is widely accepted because of its high efficiency, high reliability, and flexibility.

A DPS system uses one intermediate step to connect line power to electronic components. A utility power line enters a building with a potential of 150 to 264 V_{AC}, a frequency of 60 Hz, and a low current (Dong, 2002). A DPS converts this to an isolated 48-V_{DC} bus. Smaller, board-level DC/DC converters step this voltage down further to the voltage required for that particular application, sometimes decreasing the potential to levels smaller than 1 V.

A diagram of the DPS architecture is shown in Figure 1.4. A front-end converter includes both Power Factor Correction (PFC) and DC/DC conversion. A PFC filter serves as an AC/DC boost converter to provide an intermediate 400-V bus. It also filters

out any noise from the power transmission lines. The DC/DC converter is a switching converter that steps the voltage down from 400 V to 48 V (Yang, 2001).

The focus of this research project is a state-of-the-art discrete front-end power supply. It serves as the link between incoming utility power and the 48-V_{DC} bus. The converter includes both a PFC filter and a DC/DC converter, as shown in Figure 1.5. The PFC converter is a single-switch parallel AC/DC converter. It is designed to combine the advantages of simple topology, clamped bulk capacitor voltage and low current stress. The bulk capacitor voltage is clamped at the input line peak voltage, regardless of load conditions. The output power is processed only one time so the switch does not need to handle the PFC current a second time, as is often the case in normal PFC converters. The converter provides near unity power factor correction, transmitting nearly all energy effectively between the source and load (Zhao, 2001).

The DC/DC converter is a novel LLC resonant converter built around two coupled inductors and a capacitor. It is a three-element resonant converter with two resonant inductors and one resonant capacitor. This converter has the advantages of low switching loss, high efficiency at high input voltage and low voltage stress on the secondary rectifier. The transformer leakage and magnetizing inductance serve as the two resonant inductors, resulting in higher efficiency, higher frequency, and fewer components. This converter is a buck converter, a voltage-reducing circuit, but it has characteristics of a boost converter, which is capable of producing output voltages that are greater in magnitude than the input voltages, making it effective as a front-end converter. At high input voltage, the converter operates with load-independent low switching loss and high efficiency. The voltage gain of the converter is insensitive to load change, which is another attractive feature for front-end power conversion (Yang, 2001).

Project Goals

The goals of this project are two-fold: accurate thermal analysis of the front-end power supply described in the previous section and enhancement of the converter's thermal performance by making changes in the converter layout. The most important goals, however, sit in the shadow of the nominal goals. The development of a

methodology for computationally predicting accurate component temperatures at the system level is a primary goal. In addition, developing a methodology for component placement is more important than actually devising the layout of this particular DC/DC converter.

The goal of accurately predicting component temperatures is aimed at overcoming a variety of different challenges in the thermal modeling of power electronics. The papers described earlier in the chapter discussed many of the issues and challenges related to actually predicting component temperatures. More specific goals in this project include verifying predicted flow patterns, studying radiation and exit vent effects, and analyzing computationally predicted temperatures in a controlled environment. Lab experiments set up to benchmark different aspects of the computational code used would help to quantitatively and qualitatively discuss the ability of computational prediction of power electronics at the system level.

Developing a computational methodology for system-level simulations is important for modeling new system designs. The goal of current research at CPES is to develop a DPS front-end converter using IPEMs. Establishing the most accurate boundary conditions and finite element configurations is important for more time-efficient modeling of future systems. Once the geometric model, finite element model, and boundary condition definitions have been established, the same modeling methodology should be easily used to quickly provide component temperature predictions for newly designed systems.

The goal of rearranging components to achieve a system layout with maximum thermal performance is secondary to developing suggestions for component placement based on flow field effects. Computationally analyzing a series of separate layouts helps not only to devise a final layout with optimum thermal performance, but also to study the effects of the flow field on component temperatures. Moving any component in an electronics enclosure changes the flow patterns in that enclosure. The magnitude of change depends on the original placement of the component and the location to which it is moved, but any changes in the flow field are capable of changing the local heat transfer coefficient of the air flowing near components, thereby changing the component operating temperature.

Uniqueness of Research

Several aspects of the research outlined in this thesis have not been addressed in the literature. The DPS front-end converter is a state-of-the-art electronic module with a power density higher than other commercially available front-end converters of the same power rating. This was also an interdisciplinary project, involving the circuit designers in the thermal analysis and component rearrangement study. The electrical operation of the circuit was considered as well as the thermal performance. Another unique part of this study is benchmarking of I-deas, a commercial code used widely in local industry. Many commercial codes are used in research projects today, but I-deas is one that is not widely discussed. Finally, a radiation study using the Monte Carlo ray-trace (MCRT) method of radiation heat transfer is introduced in this project, solving difficult issues that have plagued past radiation studies.

The DPS front-end power supply studied in this project is a state-of-the-art design built to push the limits of power density. A power density of 11 W/in.^{3} is higher than the industry standard for 1.2-kW front-end converters of the same size, which typically have power densities ranging from 7 W/in.^{3} to 10 W/in.^{3} (Dong, 2002). This makes thermal simulation difficult because of the number of components operating near their temperature limits. Since this is a new layout design, no thermal temperature predictions have been computed before this project for the new power supply unit.

Input from both electrical and mechanical engineers was used in the thermal study of the front-end converter. Throughout the project, weekly interaction with the designers of the circuit helped keep estimated power losses current and allowed consideration of electromagnetic interference (EMI) effects and electrical effects, as well as thermal performance. Many studies focus only on thermal analysis and consider no electrical characteristics, and others include thermal measurements performed by electrical engineers, who in general are not as knowledgeable in accurate heat transfer measurements as mechanical engineers. This study combined the expertise of both to ensure excellent electrical and thermal operation.

One great void in power electronics literature is an in-depth study of radiation effects on a power electronics circuit. The MCRT method for calculating radiation heat transfer that was performed on the power supply in this study is unique. The MCRT method of radiation heat transfer has the ability of including specular or even bidirectional surfaces in the analysis. An assumption made for most traditional radiation calculations assumes diffuse surfaces, which could cause significant uncertainty in analyses in which specular surfaces are present, such as flat aluminum heat sink faces or metal enclosure walls. A methodology for studying radiation in other electronics enclosures could be extremely beneficial for a number of power electronics situations in which radiation has dominant effects.

The front-end DPS power supply is used as a model on which several studies could be based to help in developing important design and analysis methodologies that could be extremely important to future designs in power electronics. Accurate computational predictions of component temperatures cannot currently be achieved with ease. A few areas of uncertainty in system-level predictions have been addressed in this project with the hope of aiding progress towards establishing accurate thermal simulation codes in the future. Many of the studies discussed in this thesis are unique or have unique components to them, and hopefully they will be helpful in continued power electronics thermal simulation.

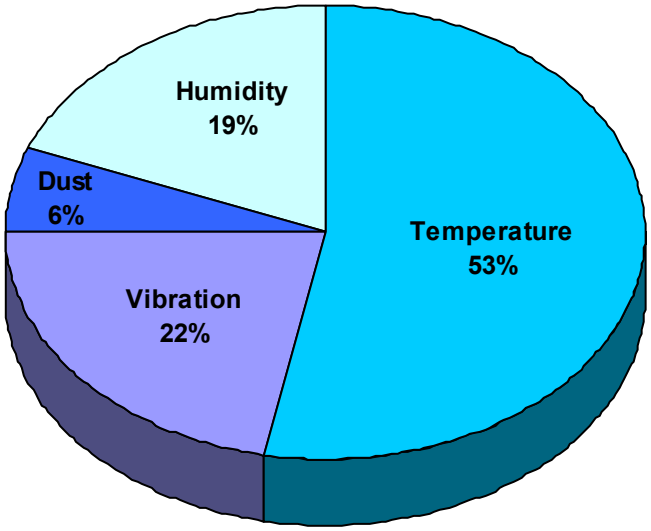

Figure 1.1. The breakdown of failures in electronics shows the need for thermal design (Soule, 1994).

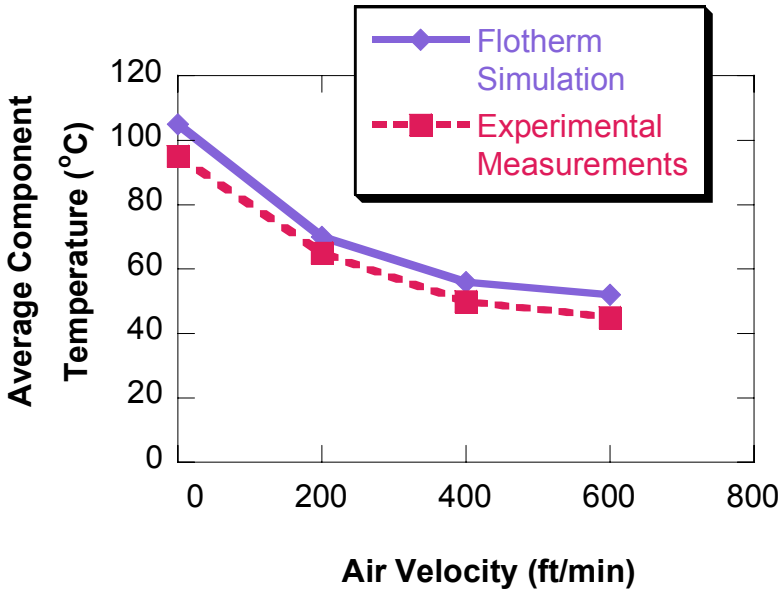

Figure 1.2. The computational and experimental comparisons show close agreement in temperatures, but the trend shows very good agreement (Liang, 2002).

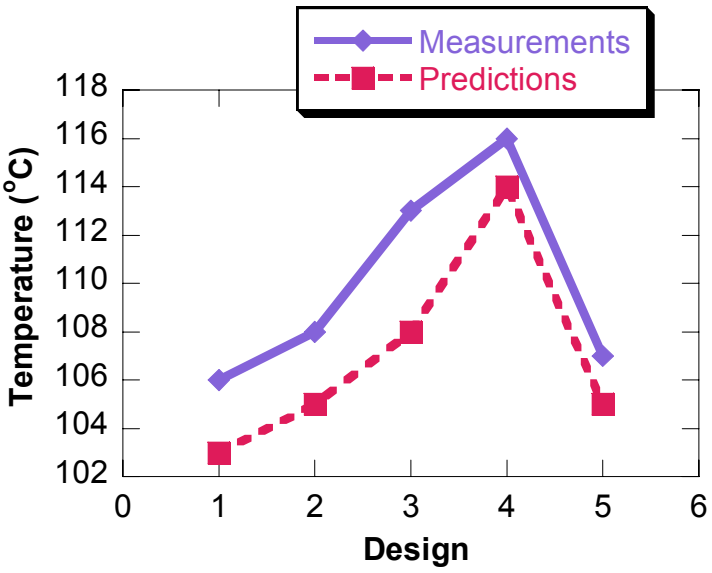

Figure 1.3. Temperature results varied slightly for each of the five models, but the general trend agreed very well (Zhang, 1997).

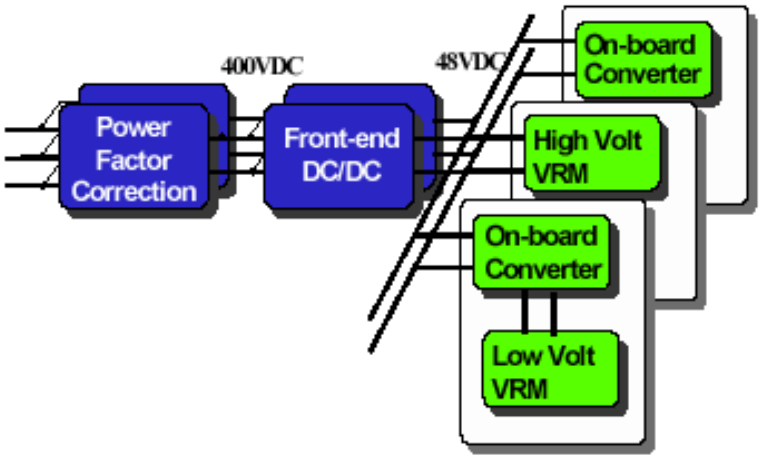

Figure 1.4. A DPS feeds a common bus to which subsystems connect to (Yang, 2001).

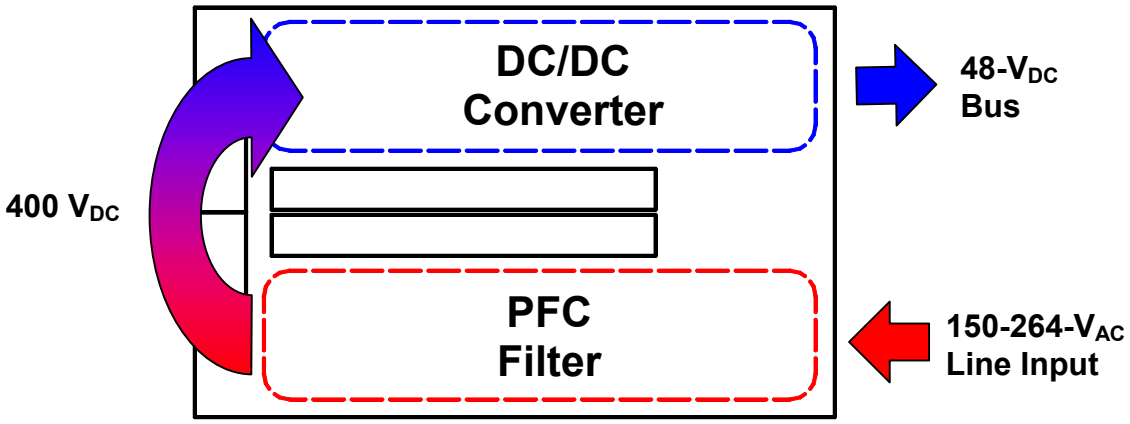

Figure 1.5. The front-end power supply links the high voltage input to a steady isolated DC bus.

Chapter 2 – Computational Methodology

The primary advantage of thermal design software is its ability to provide the estimated temperatures of components before the system is physically constructed. These steady-state temperature levels play an important role in the reliability of a component. A thermal finite-element program uses input from the designers of a circuit to simulate the thermal performance of a system and to return the steady-state temperature predictions of each component within that system. Keeping the components below their allowable temperature limits has become an increasingly important part of electronics design.

This chapter gives an overview of I-deas, Version 8 (I-deas, 2001), the software used to simulate the thermal performance of the DC/DC converter studied in this project. First, an introduction as to why I-deas was chosen over other thermal software will precede an explanation of the converter model geometry. Once the geometry has been described, the chapter will outline the assumptions and boundary conditions used in the modeling. Finally, a brief description of the I-deas solver and solution criteria concludes the explanation.

2.1 I-deas Description

As part of the work done in conjunction with CPES, Pang (2001) established the use of I-deas over other thermal design software. I-deas met several criteria established for the selection of an adequate simulation program. These criteria include finite-element heat transfer (HT), CFD, radiation analysis capabilities, compatibility with other programs, and the ability to control the program with text-based optimization software (Pang, 2001).

I-deas is a finite-element software package that contains functions for modeling, finite-element model construction, establishing boundary conditions, and running simulations, which include thermal, mechanics, vibration, and acoustic simulations. The

hierarchy is constructed as several sets of commands set up under the umbrella of the main program I-deas. The command sets used for the simulations in this project include the Master Modeler, Meshing, Electro-System Cooling (ESC), and Post Processing. The Master Modeler is used to construct a geometric model of the converter, and the Meshing commands are used to build the finite-element model based on the geometric model. The boundary conditions are applied to the finite-element model with the commands in the ESC Cooling set. The ESC Cooling commands also allow the user to set up and run the simulations, which are analyzed using the Post Processing commands.

In the early design stages, a program such as I-deas can be extremely beneficial in testing possibilities to consider which designs might work best. An accurate thermal model of the DC/DC converter being studied is extremely valuable. The power losses provided by circuit designers are very difficult to predict, however, making exact temperature results extremely difficult to provide. Reasonable approximations, however, would allow for important design decisions to be made. Since simulated temperatures as close as possible to reality are sought, the author invested much work into comparing the results output by I-deas with actual temperature and flow field measurements, as discussed in Chapter 3.

2.2 Converter Geometry

The state-of-the-art in power electronics is marked by an increase in power density, the power input into the converter divided by the volume of the enclosure. The state-of-the-art DC/DC converter designed for Eltek by CPES has a power density of approximately 11 W/in^3. The Eltek DC/DC converter currently on the market for 1.2-kW applications has a height of 1.5 U, or 6.6 cm. The improved Eltek converter, the one studied in this project, was designed for a package with a height of 1U. The challenge of the new design is to fit a converter with this power rating into a 1U package, pushing the limits of the present-day power density standards. These constraints governed the design of the enclosure, set early in the design to have dimensions of 25 cm in length $\times$16 cm in width $\times$ 4 cm in height.

The I-deas geometric model of the baseline DC/DC converter studied in this project is shown in Figure 2.1. Table 2.1 lists the components included in the converter and their estimated power losses. The number of each component corresponds to the number on the schematic in Figure 2.2. The power losses by component are given in Figure 2.3.

Constructing a useful geometric model was the first step in setting up the computational model. The I-deas Master Modeler was used to create a three-dimensional layout of the components. A box described the external boundary conditions, and after the fans and PCB were included, the components could be added individually. Component colors could be defined for display purposes. The I-deas Electro-Systems Cooling (ESC) function only solves the finite element model constructed for a single part, so the enclosure was defined as a single part and the components making up the system inside the enclosure were defined as partitions of that part.

2.3 Boundary Conditions

The system-level boundary conditions make up the system constraints that cannot be changed without making major changes to the external system and are summarized in Figure 2.4.

Two fans were permitted in the overall design to cool the system. They were specified early in the design as Panasonic Panaflo FBK04F12U fans, which have dimensions of 4 cm in width $\times$ 2 cm in length $\times$ 4 cm in height. At normal operating conditions the 12-V fans run according to the manufacturer's fan curve in Figure 2.5. The assumption that a fan curve accurately describes the behavior of the fan under normal operating conditions has been shown to be questionable (Grimes, 2001). However, since no other data are available and experimental characterization of the fan operation would require too much in time and resources, the fan curve was assumed to be accurate in this project.

The fan curve relates the volume flow rate of air (m^3/min) produced by the fan for a given pressure rise (Pa) required to force the air through the enclosure. The second

designation on the x-axis is the velocity of the air (m/s) through the enclosure when both fans are considered to be operating and half of the cross-sectional area is blocked by components. This relationship between the given volume flow rate and the expected air velocity may be written

$$\text{Bulk Velocity} = \frac{\text{Volume Flow Rate} \cdot 2\text{Fans}}{\frac{1}{2}\text{Cross-Sectional Area}} \tag{2.1}$$

For the range of velocities given above and for an estimated air temperature of 75°C, the maximum Reynolds number encountered within the enclosure would be 22,900. The average velocity in the baseline simulation was 2.45 m/s, and the average Reynolds number was 18,640. The critical Reynolds number for flow based on a characteristic length is 2300, and the Reynolds number based on the hydraulic diameter of the front-end converter is approximately 9,000. Therefore, the flow field in this converter is assumed to be turbulent. In addition, the complex geometry supports the assumption that the air is either developing or turbulent. Lee (1994) used a turbulent flow model when simulating flow through a row of printed circuit boards in a computer case. Preliminary computations overestimated air temperatures when laminar flow assumptions were made. In the present project a mixing length turbulence model was assumed.

The exit grills opposite the fans do not have a final design. Since modeling exit grills in finite element programs is difficult to achieve, the exit has been simplified immensely in this analysis. For most simulations the exit has been left completely open, but for the simulations in Chapter 5 approximately 50% of the cross-sectional area of the converter has been blocked, as shown in Figure 2.6. Modeling the exact behavior of the exiting air is not as important as providing a realistic pressure drop in this case.

Another assumed boundary condition consists of the use of adiabatic walls. Designing a rack-mounted module at the system level requires consideration of the surrounding walls. Enclosures mounted immediately adjacent to the converter could dramatically affect the component temperatures in both systems. Air flowing (or lack of air flowing) on the outside of the enclosure could affect heat transfer by convection to or

from the surroundings, and any modules in contact with the case could potentially conduct heat to or from the system. Radiation could also be a consideration for modules with significantly different temperatures. In this project, however, no information concerning the surrounding modules or rack design is provided, so all surfaces forming the enclosure are considered to be adiabatic. This is a reasonable assumption, however, for the systems in a rack of modules with similar temperatures.

The ambient air temperature entering the enclosure for all simulations was defined to be 50°C. All simulations have been computed with this as the ambient temperature because it is considered the most conservative case. This assumed inlet temperature also affects the wall temperatures in any radiation calculations. In addition to the temperature specification, the ambient air pressure is 1 atm.

2.4 Computational Model Assumptions

To construct a mathematical model sufficiently simple to be solved by the computing power required by I-deas, several simplifying assumptions were made. System-level simulations must be simpler than component-level simulations simply because the reasonable computational times are desirable. These assumptions are described in the following paragraphs.

Individual components in the DC/DC converter were modeled as solid volumes with uniform heat generation. Although this assumption does not provide data for local temperatures within a component, an energy balance on each component would still be valid. This tradeoff must be made to allow the entire system to be simulated. The assumption of modeling a component as a single volume is accurate for components such as a bulk capacitor mounted to the PCB, but it can be inaccurate in others, such as semiconductors on a heat sink. These inaccuracies on local temperatures will also affect the local heat transfer to the heat sink.

Another assumption is that all components have constant physical properties. In reality, physical properties vary as a function of temperature, manufacturing processes, impurities, and aging. The thermal conductivity of materials is an extremely difficult

property to determine for the multi-structure devices that were simulated, so values from standard tables are assumed. Most components are modeled as consisting of single isotropic materials with constant thermal conductivities. Table 2.2 contains a list of the materials used and the thermal conductivity values defined for each material.

One difficulty in modeling components mounted to a heat sink is the issue of thermal interface between the two connecting surfaces. For the simulations in this project, a perfect thermal interface was considered between the semiconductors and the heat sink. The copper plate on the back of a semiconductor allows for uniform heat distribution on the back surface, but the challenge of mounting the component lies in uniting the back component surface evenly to the heat sink face. A TO-220 package is mounted to a heat sink with a screw. Over-tightening this screw causes inconsistency in the contact pressure along the top of the package and the bottom. Uneven spreading of thermal glue or surface fissures in either surface can introduce their own inaccuracies, which vary from case to case.

The PCB in the converter is modeled as an adiabatic surface to provide a conservative calculation. PCB conduction is difficult to quantify because the board is imbedded with hundreds of thin copper traces, resulting in highly anisotropic board behavior. Most of the large heat-dissipating components in this converter are mounted with small pins soldered to the board, so a negligible amount of heat is conducted to the board. Unless otherwise stated, the simulations in this project neglected heat conduction into the PCB.

Another assumption, with regard to the heat dissipated by the magnetic components, is that all heat is generated in the windings and is only transferred to the magnetic cores through conduction. This converter includes a transformer, a boost inductor, and two EMI filter inductors that dissipate a significant amount of heat. The heat loss distribution on magnetic components is difficult to quantify. As stated earlier, simplifying the geometry eliminates the usefulness and accuracy of locating hot spots on a device but is a necessary assumption for these computations. An energy balance on the magnetic component still applies, but hot spots will not be accurately predicted.

In the flow model, a no-slip boundary condition is assumed at the walls. This condition became an important consideration in the determination of heat transfer at component surfaces.

Finally, the flow field is assumed to be turbulent with no natural convection effects. In the case of two fans drawing air into a small complex enclosure, the flow is most likely either developing or turbulent due to mixing caused by fans and complex flow blockages. The air velocity is also assumed to be sufficiently high that there are no natural convection effects around the components. The Grashof number is a measure of the ratio of the buoyancy of a fluid to the viscous forces of that fluid, and it provides a good indication of whether or not natural convection can be neglected. For a (vertical) length of 4 cm, the Grashof number was calculated to be 217,600, and the approximate Grashof number calculated in the baseline I-deas simulation was 140,000. The criterion for neglecting natural convection effects is

$$\frac{Gr_L}{(Re_L)^2} << 1 \qquad (2.2)$$

In the converter under study, this ratio is shown to be approximately 4×10^{-4} for a maximum Reynolds number case. This is in accordance with the criterion defined above, and therefore natural convection effects may be neglected.

2.5 I-deas Simulations

Once the external boundary conditions were established and simplifying assumptions were made, the geometric model could be constructed in I-deas. The finite element model could be based on the geometrical model and the thermal boundary conditions could be applied. After these conditions were established, the mass, momentum, and energy equations could be solved to calculate the node and element temperatures as well as air velocity vectors.

The second step in the simulation process was to construct the finite element model. The I-deas meshing commands were used to define material properties and apply

surface and volumetric meshes to geometric surfaces and volumes. The free-meshing commands provide the simplest approach to meshing the volumes because they are geometry-based and construct meshes that adapt their sizes to match those of previously meshed components. In Figure 2.7, a finite element model of the baseline model presented earlier illustrates the challenge of a system-level simulation, in which the elements must be distributed evenly to describe all components. A significant challenge in this project is producing a sufficiently fine mesh to provide an accurate representation of the geometric model but which is still sufficiently coarse to be solved by a computer, as mesh size is a potential source for inaccuracies. Two dimensions describing the heat sink in the DC/DC converter are fin thicknesses of 1.4 mm and a heat sink length of 150 mm, making an accurate model a challenge to build because of a drastic difference in length scales. Due to the number of long thin fins, a sufficiently small cell size to adequately resolve the heat sink's heat transfer behavior is limited by a lack of computational resources.

Table 2.3 shows the components and surfaces meshed, the materials, and the size of the elements used in the mesh. Note that surfaces meshed with a null material were included to account for flow and radiation effects not involving conduction. Once the finite element model has been constructed in I-deas, the only remaining task is to apply the boundary conditions to the components and simulate the model to obtain temperature and flow field results.

The I-deas ESC commands were used to define the model's boundary conditions. The options needed for this simulation include thermal loads, thermal couplings, surface properties, flow surfaces, flow blockages, fans/fan curves, vents, ambient conditions, and simulation utilities. Each of these commands was used to customize the model specific to the front-end converter being studied.

First, the heat loads were applied to the heat-dissipating components. The circuit designers simulated the circuit using Saber Designer (Saber, 2001), and obtained results for the power dissipated by each component. These losses translate into the heat loads applied as boundary conditions in I-deas. The loads applied in this project were all geometric boundary conditions (not finite-element-based). Geometric boundary conditions are related directly to the volumes modeled instead of the finite elements used

to describe those volumes. For most components, they were applied as uniform heat generation loads (in Watts) evenly distributed throughout the volumes. For the magnetic components the heat loads were evenly distributed throughout the copper windings, and for the TO-220 packages the heat loads were applied to the copper tab on the back side of the packages.

Thermal coupling is a boundary condition that relates two surfaces that are not directly connected through physical contact. It defines a heat transfer relationship between two finite elements not joined directly by their nodes. Several types of thermal coupling include absolute, resistive, conductive, and radiative thermal coupling. Each type of coupling allows a certain property value to be assigned to it. For instance, an absolute thermal coupling was used to relate the transformer winding surfaces to the magnet surfaces in a "single coupling calculation." A "conductance per element" of 0.5 W/K was chosen because preliminary simulations using this value resulted in a minimal temperature gradient between the cores and winding. The conductance value describes the quantity of heat that will flow from the hotter element to the cooler element per degree of temperature difference between the two elements. In electronics the exact coupling values can potentially be very difficult to determine, but they are useful in adding a lifelike "complexity" to models of actual electronic systems. They can also be easily varied to assist in determining the presence of added effects in a system.

All surfaces using thermal couplings were meshed with surface meshes the same size as the component volume meshes. The thermal couplings were still added as geometric boundary conditions. A thermal coupling could be added between the semiconductors and the heat sinks to represent the contact resistance, but in this project a perfect thermal interface was assumed. For the radiation analysis, a final thermal coupling value was applied as a radiation boundary condition. The surface meshes for components involved in the radiation analysis of the inductor are shown in Figure 2.8. The surface mesh is shown in red, and the air mesh, heat sink mesh, and enclosure wall meshes are all deleted for clarity. A more detailed radiation analysis is described in Chapter 4.

A surface property must be used to define flow blockages. A surface property is defined by the surface roughness and convection heat transfer coefficient. The option for

automatically calculating the surface roughness from surface obstructions was selected for the simulations in this project, and the heat transfer coefficient for all cases was set to be automatically calculated from local flow conditions.

Flow blockage boundary conditions define the presence of solid components in the flow field. This boundary condition was applied to every component in the converter, allowing I-deas to understand where the flow obstructions were. A convection surface was also defined through this boundary condition. Options for permeability were available, but all of the components in this converter were defined as solid objects.

The fans could also be specified in this ESC section. A single fan boundary condition was applied to each fan opening area. They were defined as inlet fan curves with behavior corresponding to the fan curve shown in Figure 2.5. Table 2.4 lists the discrete values input into I-deas as points on the fan curve. Fans generate a small amount of heat during normal operation. The data sheet provided by the manufacturer listed the fan's "rated input" as 2.04 W. To account for this, a fan dissipation load of 2 W was applied to each fan.

The option for specifying the vents is simple. This boundary condition is applied to a geometric surface on the model, and the pressure difference between the calculated pressures downstream of the fan and ambient exit pressures determines the direction of flow. The option for specifying a vent to a specific temperature or pressure is available, but for these cases a vent to ambient temperature and pressure was selected.

The ambient conditions can also be set in the ESC commands. As stated earlier in the chapter, the ambient temperature was defined as 50°C and the ambient pressure was defined as 1 atm.

The final step in the simulations was to solve the model. The simulation options could be set with the ESC commands, as well. The results available at this point included velocity, temperature, pressure, K-ε turbulence, fluid density, mass flux, heat flux, heat transfer coefficient, processed flow model, and Y+ values. For most simulations the temperature and velocity results were desired, but in some situations the pressure and mass flux results were also considered. The simulation options could also be set, though the default settings were primarily used. For the solver mode, both the "Execute Flow Solver" and "Execute Thermal Solver" options were selected, and the Mixing Length

turbulence model was chosen as the flow model instead of the laminar model or the fixed turbulence viscosity model or more complicated K-ε model. The selection for buoyancy (natural convection) was not selected because forced convection was shown earlier to dominate the heat transfer and because of the exponential increase in complexity and solution time introduced into the problem. The convergence criteria could also be specified. In these simulations a concurrent solution method was used as opposed to a sequential solution method. Temperature convergence was achieved when the temperature change was less than 0.1 and the RMS flow residuals less than 0.0002. For the temperature solver, a normalized convective heat imbalance of less than 0.01 was required, and a normalized global heat imbalance of less than 0.02 was required for the flow solver.

Solutions converged on a computer driven by a 1.7 GHz Pentium 4 processor in as little as a few minutes for simple, component level studies to as many as 6 hr. for the baseline simulations. Since natural convection calculations require simultaneous solutions of the energy and momentum equations, much more computational time was required and convergence was extremely difficult to achieve. More information on computer solution time is given in Appendix B.

After the solution has converged and the results have been loaded into the model file, the next task was to post process the results. Viewing specific results on the model volume or a cutting plane of the model allowed the post-processing analysis to be done visually. The false-color results could be compared to the legend for approximate results, and the "probe" command could be used where more exact temperatures were desired. Another method for finding temperatures was to locate the maximum temperature predicted in the model from the simulation results file.

The simulation of a front-end converter model is important because it allows us to improve the overall thermal performance. The boundary condition definitions and assumptions made have been clearly stated because of the potential for inaccuracies caused by incorrect assumptions. It is impossible, however, to model a power circuit the size of the 1.2-kW converter at the system level without making simplifying assumptions to reduce the size of the model to something that can be solved computationally.

In this chapter the process of setting up and solving the finite element model as well as analyzing the temperature and flow field results is explained. Being able to effectively use thermal design software provides significant advantages to a power system designer by aiding in understanding the thermal performance of new designs. Applying the proper physical boundary conditions from well-informed assumptions is the first step in ensuring that the thermal performance results obtained best describe the physical system being studied.

Table 2.1. Component Power Loss Breakdown

Number	Description	Power Loss
1	EMI Inductor 1	2 W
2	EMI Inductor 2	2 W
3	Bridge Rectifier	15 W
4	PFC MOSFET 1	5 W
5	PFC MOSFET 2	5 W
6	PFC Output Capacitor	2 W
7	Boost Inductor	8 W
8	Boost Diode 1	1.5 W
9	Boost Diode 2	7 W
10	Boost Diode 3	1.5 W
11	DC/DC Input Capacitor	2 W
12	DC/DC MOSFET 1	10 W
13	DC/DC MOSFET 2	10 W
14	Transformer	15 W
15	Secondary Diode 1	8 W
16	Secondary Diode 2	8 W
17	DC/DC Output Capacitor 1	1.5 W
18	DC/DC Output Capacitor 2	1.5 W

Table 2.2. Material Thermal Conductivity Values

Material	Thermal Conductivity (W/mK)
Null	0
Aluminum	170
Copper	400
Plastic	2
Ferrite	5
PCB	10
Steel	15
Balsa Wood	0.05

Table 2.3. Finite Element Mesh Characteristics

Component	Material	Size
Fan Surfaces / Vent Surfaces	Null	4.0 mm
Heat Sinks	Aluminum	1.8 mm
Inductor Windings	Copper	2.0 mm
Inductor Core	Ferrite	4.0 mm
Capacitors	Aluminum	4.0 mm
EMI Transformer Package	Plastic	4.0 mm
EMI Transformer Winding	Copper	4.0 mm
EMI Plug	Plastic	4.0 mm
Transformer Windings	Copper	4.0 mm
Transformer Cores	Ferrite	4.0 mm
Trans. Winding/Core Interface Surfaces	Null	4.0 mm
TO-220 Backs	Copper	1.5 mm
Semiconductor Packages	Plastic	2.0 mm
Radiation Surfaces	Null	---*
Air Volume	ESC_Air	3.0 mm

*Radiation surfaces meshed to match volume size

Table 2.4. FBK04F12U Fan Curve

Volume Flow (m^3/min)	Pressure Rise (Pa)
0.00	140.0
0.05	90.0
0.10	50.0
0.15	40.0
0.20	37.5
0.25	12.5
0.27	0.0

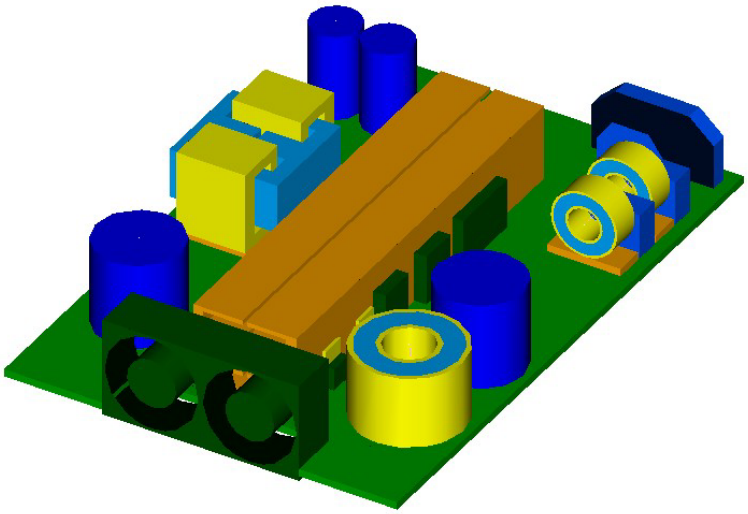

Figure 2.1. The I-deas-based baseline model of the DC/DC converter served as a starting point for the parametric study and component-level studies.

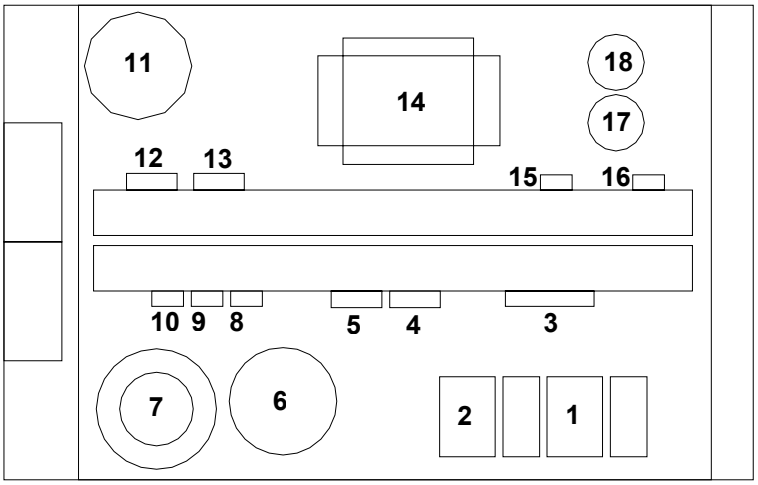

Figure 2.2. The DC/DC converter contains eighteen power-dissipating components.

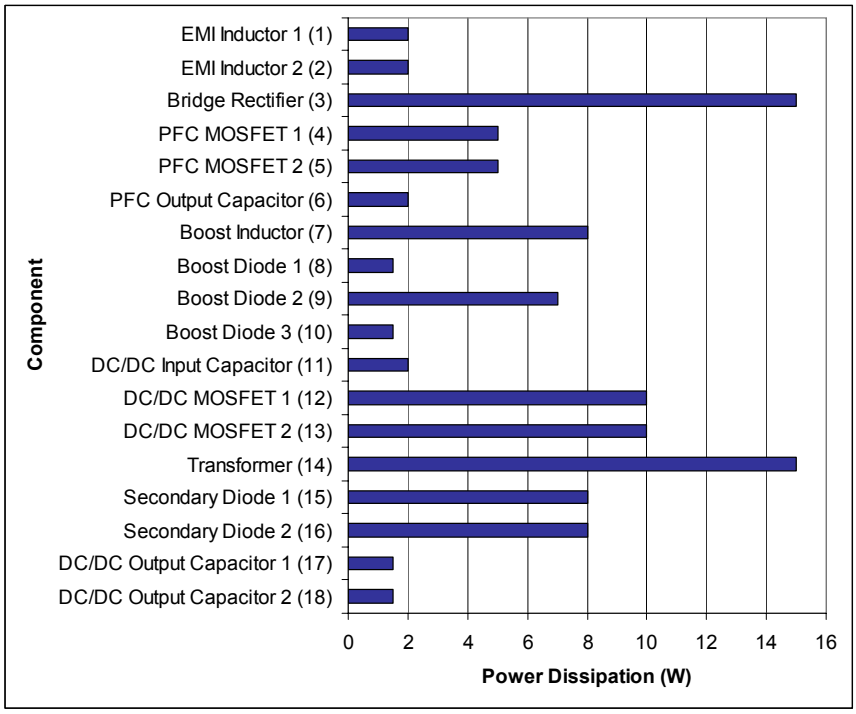

Figure 2.3. The power losses of the components correspond to the numbers on the converter diagram in Figure 2.2.

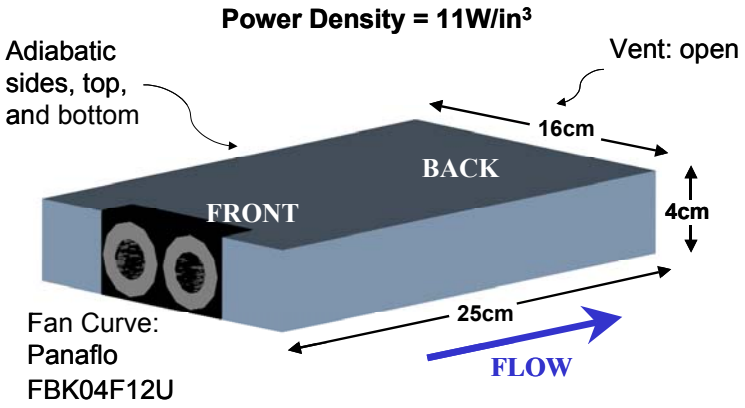

Figure 2.4. The system-level boundary conditions establish the constraints to the internal thermal design.

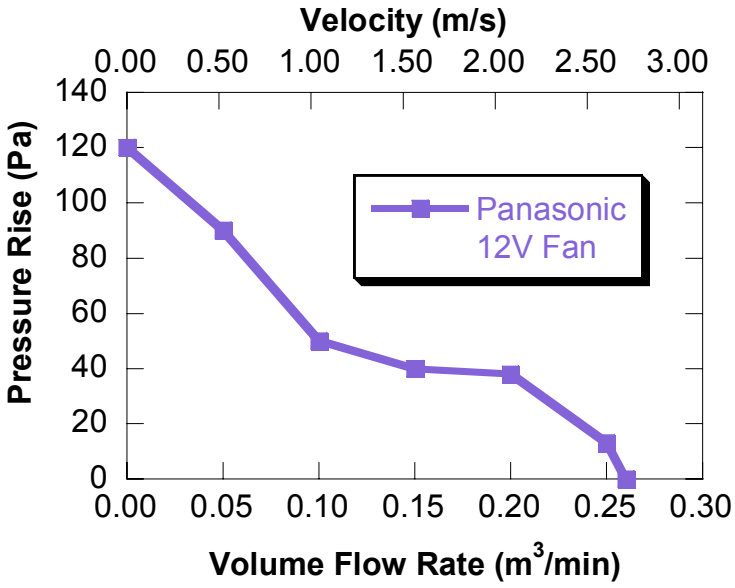

Figure 2.5. The fan curve specified by Panasonic is used as the inlet boundary condition.

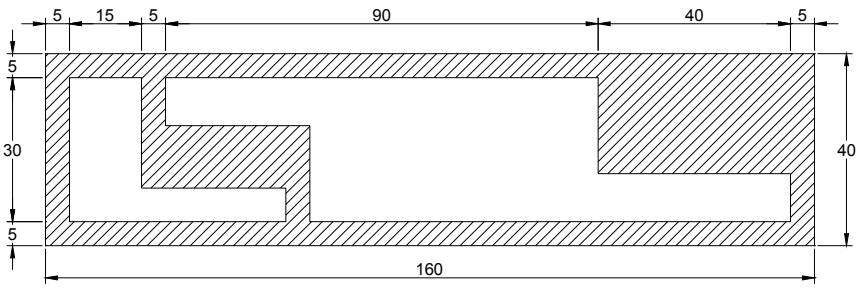

Figure 2.6. A partially-opened exit grill (looking from outside the box) was used in some of the I-deas models (dimensions in mm).

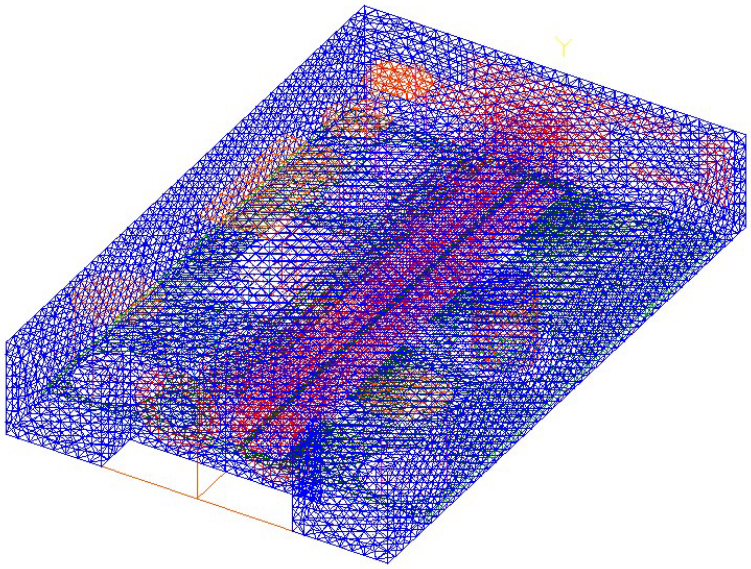

Figure 2.7. A system level finite element simulation requires a significantly large number of elements for the finite element model.

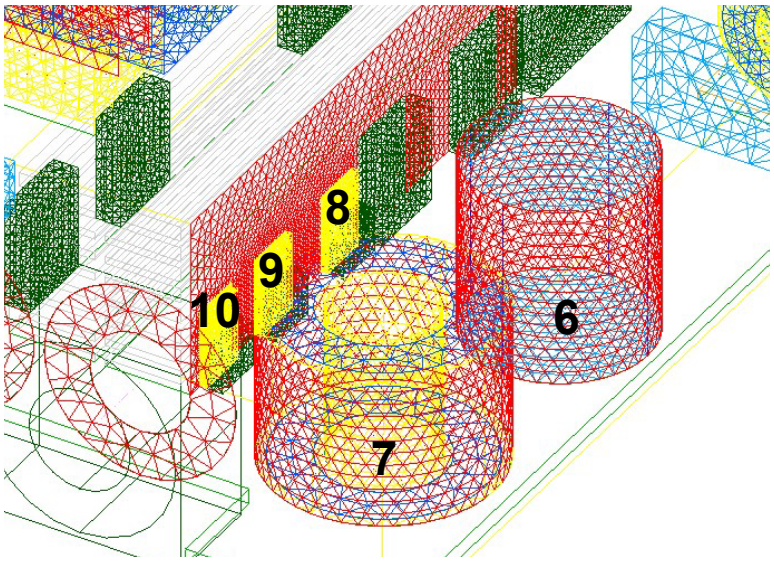

Figure 2.8. The surfaces of components were meshed to include thermal couplings, such as radiation, shown here in red. The components are numbered corresponding to Figure 2.2.

Chapter 3 – Experimental Verification

Benchmark experiments are needed to ensure accurate temperature predictions for power electronic systems. Uncertainties that make predictions difficult for a system include modeling interfaces between semiconductors and heat sinks; predicting complex flow field interactions; calculating accurate volume flow rates described by the fan curve; knowing accurate power dissipations; choosing the correct boundary conditions; and simulating effects of radiation, exit grill effects, and conduction into the PCB. In particular, the power dissipated by a component is difficult to predict because it is a function of switching frequency, material properties, nearby components, and operating temperature. The issue of power dissipation is a major source of uncertainty, sometimes predicted with an accuracy no better than ±40%, but it was not addressed in this project as that is the responsibility of the circuit designers (Van Wyk, 2002). As such, it is not desirable to use actual power synchronous systems to benchmark predictive codes. Rather, it is important to create a more controlled environment and benchmark against experimental data acquired in this environment.

The accuracy of I-deas simulations determines the program's usefulness as an analysis tool for thermal predictions. Benchmarking the I-deas code assists in recognizing the possible uncertainty of simulations when compared to real systems and in showing which parameters give the best comparison to experimental data when modeled in I-deas. A number of experiments were performed to compare with simulation data and to display the ability of I-deas to predict component temperatures in operating situations.

This chapter begins with an overview of the four different experiments that were completed to address the predictive accuracy. The following sections move on to explain each of the experiments in detail, presenting both computational and experimental results and comparing the two whenever possible.

3.1 Test Cases

Table 3.1 outlines the four experimental conditions simulated, the type of instrumentation used, and the goals sought by each one. In the first case, two working circuits, each of which consisted of one-half of the converter's major heat-dissipating components, were measured for steady-state component temperatures by using thermocouples. The temperatures measured were full of uncertainties resulting from the fans used, the power lost by each component, PCB conduction, and electrical interference due to threading thermocouple wires through an AC system. As such, the comparisons between the experimental temperatures and simulated temperatures were difficult to draw conclusions from.

The uncertainty in quantifying the thermal resistance between a semiconductor and the heat sink it was mounted to was addressed by the second experiment in Table 3.1 by using experimental data taken by Pang (2001). She mounted two power MOSFETs to a heat sink and used an infrared (IR) camera and thermocouples to analyze the temperature rises resulting from dissipating a known power in the MOSFETs.

The goal of the flow visualization experiment, Case 3, was to show the validity of flow field predictions shown by I-deas. The complex flow field has important implications in the heat transfer occurring in the circuit, and I-deas' prediction of the major patterns in this flow field is important but difficult to verify.

The final comparison was between a known constant heat flux dissipated by a component-sized heater in a complex but controlled flow field with the computed predictions of that heater's temperatures in I-deas. By dissipating a known value of heat by a heater placed inside an insulated enclosure with a controlled mass flow rate, the uncertainty of power dissipation could be bypassed. The fan curve uncertainty, system heat transfer, and PCB conduction effects were also bypassed when designing this experiment.

3.2 Test Circuits

For a full computational analysis, the major information needed from the circuit designers is the circuit layout and the heat losses (power dissipation) of each component. Since the converter is divided into two sections, a PFC filter and a DC/DC converter, the CPES designers (Yang, 2001 and Zhao, 2001) working on this project constructed a working test circuit for each side to test the operation of the major components. The test circuits had no microelectronic components, which would normally control many of its minor operations, but the major components that were present in the experiment were responsible for the majority of the heat loss. This made the circuit ideal for a thermal analysis. The methodology of the thermal experiment was simple. Thermocouples were glued onto the major heat-dissipating components and the circuits were tested with a 1 kW power input. A Panaflo fan model was mounted onto each board and operated at 12 V. The circuit was covered with a cardboard cover to contain the cooling flow. A digital thermocouple readout with six inputs displayed the temperatures, which were recorded by hand. The resolution of the meter was 1°C. Temperatures were recorded at intervals of 5 minutes until three consecutive measurements showed no temperature changes, indicating steady state. I-deas simulations of the same circuit configurations reported component temperatures that could be compared with the experimental values.

The first circuit tested was the PFC filter, which serves as the input to the system. The function of this side is to rectify the signal from AC to DC. The circuit was designed and built by Zhao (2001) and is shown in Figure 3.1. A model of this circuit was built in I-deas and simulated to compare with the circuit, and it is shown in Figure 3.2. The DC/DC converter was designed and built by Yang (2001). It is shown in Figure 3.3. This circuit was also simulated in I-deas. Figure 3.4 shows the I-deas model built to represent this circuit.

The test methodology for the PFC filter included making six thermocouples and gluing them to five places in the circuit and mounting one near the fan intake to measure inlet air temperature. The DC/DC converter was tested in a similar way, except a handheld digital thermometer was used to measure inlet air temperatures. The thermocouples used were Type K and made with 24 AWG wire. The thermocouple

locations are listed in Table 3.2. A thermally conductive glue used for the thermocouples was Loctite 384 (mixed with the activator Loctite 7387), a tough acrylic adhesive.

The inability to predict the exact power loss during the operation of the circuit greatly impeded the testing done for comparison purposes. The reason for this inability was that the operating point power losses were difficult to predict, and also the circuits operated at reduced power (1 kW) and each was isolated from the other half. Too many unknown power losses prevented the development of a meaningful simulation. A comparison was made, however, between the circuit temperatures and the temperature predictions, and the results would show the difficulty in trying to model unknown parameters and provide a motivation for further experimentation under controlled conditions. Table 3.3 lists the temperature measurements for the thermocouples described by Table 3.2. The inlet air for the PFC Filter was measured by thermocouple 6, but the inlet air for the DC/DC converter was measured by a handheld thermometer and was not included in Table 3.2. The inlet air temperature for the DC/DC converter was 24°C, the same as the inlet temperature for the PFC filter measurement, and this value was used as the outside air boundary condition for the I-deas simulations, as well. The comparisons in Figure 3.5, however, are temperature increases above the inlet air temperature for both the experiments and computations.

The comparisons in Figure 3.5 indicate that measuring electronics temperatures and comparing them to computational predictions is not an easy task. Differences as high as 25°C occurred for the EMI Inductor, but one positive note is that the air outlet temperature was correctly predicted. The success of using thermocouples to measure electronics is impeded by an inability to accurately predict the power loss, along with a number of other secondary effects. These results led to an exploration of a simpler, more controlled environment in which temperature measurements could be taken with more confidence and computational simulations can be performed with fewer unknown variables.

3.3 MOSFET IR Camera Tests

Pang (2001) performed a series of detailed simulations with a component level focus. In her work, she set up a controlled experiment in which she mounted two power MOSFETs to a heat sink and placed the assembly inside a box with a fan blowing air through it. By placing a DC voltage across the MOSFETs in a reverse bias configuration, she controlled the power dissipated by the diodes so an exact value could be simulated in I-deas. The enclosure she built allowed her to view the top of the heat sink with an IR camera, providing results calibrated by thermocouples in view of the camera (Pang, 2001). An I-deas model of the heat sink is shown in Figure 3.6. The purpose of this test was to investigate how simulation temperature results were affected by the thermal interface between the MOSFETs and the heat sink.

Analytical results were obtained by calculating an average Nusselt number by using a correlation for laminar flow across a flat plate. The average heat transfer coefficient could be calculated from the Nusselt number, and the thermal resistance from the heat sink to the air could be determined as shown in Figure 3.7. Using the resistance network in Figure 3.7, the author used the calculated thermal resistances and the resistances given by the data sheets to solve for the surface, case, and junction temperatures on the surface of the heat sink. The locations of the four temperatures solved for are pictured in Figure 3.8. The complete calculations of the temperatures are given in Appendix C.

In Pang's baseline case, each semiconductor dissipated 4.3 W. Since two devices dissipated power, a value of twice this power was used in the analytical calculations. This power dissipation would be in parallel since the two devices are mounted next to each other, but in a one-dimensional analysis they are treated as a single source with a value equal to the sum of their heat losses. The four temperature results for the baseline case in which 8.6 W were dissipated are listed in Table 3.4. A local air temperature of 24°C was assumed in the calculations. Once the calculations were established, it was trivial to find the temperature distributions for different values of power dissipation.

Six different thermal interface modeling options were considered for the I-deas simulations. Four different simulations were executed for each of four heat loads of 2.0

W, 4.3 W, 6.0 W, and 10.0 W per MOSFET. Table 3.5 outlines the interface configurations considered. Each configuration represented a different way thermal couplings were used within the code to represent the thermal interface.

The IR camera image, Figure 3.9, was taken of the top surface of the heat sink/MOSFET configuration for a DC power loss of 4.3 W across each diode. The ambient temperature during the experiment was 24°C, and the MOSFET temperature rise above ambient at the MOSFET case measured by a thermocouple between the semiconductor and heat sink was 13°C. When the power was increased to 7.0 W per MOSFET instead of 4.3 W, the case temperature rise was 21°C.

Figure 3.10 compares the temperature results of one simulated case and analytical calculations with the experimental data. The simulation termed "Case 2" used a thermal resistance of 0.80°C/W between the heat sink and the MOSFET, as shown in Table 3.5. The other five cases all had lower temperature results than Case 2, but they were also very similar to each other. A comparison of the simulated cases listed in Table 3.5 is shown in Figure 3.11.

The result of this study is that the modeling of Case 2 compared most closely to the experimental data. The other five cases, however, were the most consistent when compared to each other and had only slightly lower temperatures when compared to the experiments. Although good agreement was achieved for Case 2, there are inaccuracies in modeling the contact between the components and mounting surfaces due to individual mounting cases. As such, the simulations executed in this project modeled no thermal resistance between the semiconductors and the heat sink (Case 1 in Table 3.5).

3.4 Flow Visualization

One noticeable characteristic of the I-deas flow field results is the re-circulating vortices settling in behind large components and in the corners of the enclosure. Figure 3.12 shows a two-dimensional vector plot of the flow field in a flow plane 2 cm above the PCB. A variety of flow patterns are indicated, including stagnant recirculation in corners, vortices behind components, and curved streamlines directed by components. Note that

flow field vectors are colored according to *velocity*, not temperature, and a highly concentrated region of vectors (such as between the heat sinks) indicates a higher grid density than in other regions, not increased volume flow. Recirculating patterns and high velocities between components affect the local heat transfer coefficients near components. A potentially great amount of uncertainty could result if these flow field patterns are not predicted correctly. Therefore, this flow visualization study was constructed to observe some of the patterns found in simulations.

The experimental setup in Figure 3.13 showed results that verified the accuracy of these simulations in the flow directions shown in the simulations. The test consisted of using an atomizer to vaporize olive oil and guide it into the fans of the converter. A model of the converter was set up in a Lexan box the same size as the front-end converter enclosure and populated with most of the major components, including the two fans driving the flow. The box exit was left open. A white light was shone into the box through a slit formed by two rows of electrical tape, and a digital camera took five-second video clips of a few different sections of the circuit.

The I-deas system level simulations showed a pair of opposing vortices forming behind the transformer, as shown in Figure 3.14, so this was decided on as one of the first sections to observe in this study. Figure 3.15 is a still frame of one of the video clips of the flow past the transformer. The opposing vortices seen in the simulation can be seen in the open space behind the transformer. Their location is not immediately behind the component as the simulation showed, but the shape and approximate region were predicted accurately.

Another comparison can be seen in the corner of the enclosure, near the entrance. The fans form a recess where flow recirculation occurs instead of passing directly through the box. A vector plot of this flow field is shown in Figure 3.16. The swirling flow is more apparent in Figure 3.17, which is a view of the velocity vectors 1cm away from the front of the enclosure. Figure 3.17 is the view of an observer standing to the left of Figure 3.16. This same vortex was seen in the experiment, as well. The white circular pattern in Figure 3.18 is a vortex formed between the walls in the corner and the bulk capacitor. The vortex was again predicted by the computational predictions. The formation of a vortex in the corner rotating in the same manner shown in I-deas indicates

that the CFD simulations in I-deas are reliable for predicting the presence of recirculating patterns and flow around obstructions.

The comparison of the flow visualization experiments and the I-deas simulations shows that the predictions of the flow patterns in I-deas are accurate. The vortices predicted by the simulations were present in the experiments, and there were no swirling patterns or other predicted anomalies that could not be seen by the flow visualization. This was strictly a qualitative experiment. No velocity field measurements were taken. Also, the velocity and mass flow rate of air was still unknown at this point and needed to be studied. A study performed by Grimes (2001) concluded that computational velocity predictions decrease in accuracy when the fans are blowing air into an enclosure due to the uncertainty in the fan curve. A need to remove this uncertainty to assess the predictions formed the basis for the next section, in which the velocity through the converter was controlled and measured, allowing temperature results to be compared to an I-deas model with known parameters.

3.5 Controlled DC Heater Experiments and Simulations

The final series of experiments in this project sought to obtain a close comparison of experimental temperature measurements with computationally simulated temperatures in a controlled environment. The inaccuracies in given power dissipation, volume flow rate, interaction between components, PCB conduction, and system heat loss were all addressed in the design of these experiments. By introducing a DC heater instrumented with thermocouples into the model used in the flow visualization experiments, a known volume flow rate of air would allow accurate modeling of the physical system. The system model with the heater included is shown in Figure 3.19. Table 3.6 summarizes the inaccuracies expected and the specific way that problem was addressed.

Experimental Design and Construction

The component constructed for this experiment had the capability of both dissipating a known uniform heat flux across all four of its faces and of measuring its outside surface temperature at twelve different places. It is shown in Figure 3.20. The outside walls of the heater are made of resistive steel foil 0.05-mm thick with a thermal conductivity of 15.1 W/mK. Copper bus bars were soldered to either end of each side to provide a constant current distribution across each surface. A constant current through the walls caused them to heat up uniformly in such a way that the only temperature differences along the sides would be a result of convection.

Three Type E thermocouples made from 30-gauge wire were attached to each wall and numbered with the configuration in Figure 3.21. They were centered vertically and distributed evenly across each side horizontally, allowing measurement of twelve temperatures across a vertical mid-plane 2cm above the base of the converter. A dimensioned side view of the component, Figure 3.22, shows the overall component size and thermocouple locations. Dimensions shown are in millimeters.

One issue to consider in the thermocouple measurement accuracy was the distribution of temperature across the thickness of the foil. Though this resistance would be very small, any kind of significant thermal resistance would cause uncertainty between the thermocouple bead temperature and the outside wall surface. The thermal resistance of the foil and the convection resistance are given as

$$R_{th\_cond} = \frac{L}{kA} \tag{3.1}$$

and

$$R_{th\_conv} = \frac{1}{hA} = \frac{(T_{wall} - T_{\infty})}{q_{conv}} \tag{3.2}$$

The thermal conductivity and physical dimensions of the component wall determined the thermal resistance of the wall, which was calculated to be 0.003 K/W. The convection thermal resistance of the outside wall was determined by the heat generation and

temperature differences to have a value in the range of 6.9 K/W for low power and 17.1 K/W for high power dissipation. The convection thermal resistance is more than three orders of magnitude greater than the conduction resistance, and therefore the thermocouple temperature may be assumed to be the same temperature as the outside wall.

Balsa wood was used as a backing for each wall, as well as the base and top. Omegabond 400 Powder, a high temperature air set cement from Omega Engineering Inc., was used to cement the thermocouples between the balsa wood backing and the foil heaters. This bonding agent makes a good thermocouple adhesive because it is heat conductive, resistant to thermal shock, electrically insulating, and adherent to a number of surfaces. The middle of the component was filled with shredded Styrofoam for insulation, and the corners, top, and bottom were filled with epoxy for structural integrity and insulation. The thermal conductivity values of the materials used are given in Table 3.7.

Figure 3.23 is a picture of the test rig in which good control and measurement of the flow rate could be achieved through the converter model. According to the schematic in Figure 3.24, the blower was connected to a 0.6-m length of 5-cm PVC pipe, which directed air through a laminar flow element (LFE). The LFE, from Meriam Instrument Company, was a model 50MC2-2 with a nominal volume flow range of 100 standard cubic feet per minute (scfm) over an 8′′ H_2O pressure differential. The 1/4′′ (6 mm) National Pipe Tapered Threads Standard (NPT) pressure connections of the LFE connected to a pressure transducer via two rubber tubes. The transducer indicated the pressure drop across the LFE, which could be correlated to an air volume flow rate by a calibration curve, graphed in Figure 3.25. The equation describing the calibration curve describes the volume flow rate in ft^3/min (cfm) as a function of pressure in inches of H_2O.

The air exiting the LFE proceeded through another 0.6-m section of 5-cm PVC pipe and into a plenum, which decreased the air velocity before it would exit into the converter enclosure. The plenum had a cross-sectional area of 558.7 cm^2, and the 5-cm PVC pipe had a cross-sectional area of 20.0 cm^2. From the continuity equation,

$$V_1 A_1 = V_2 A_2 \tag{3.3}$$

we see that the air velocity decreased by a ratio of 1:28 as it entered the plenum. For a volume flow rate of 20 cfm, the plenum velocity was 0.17 m/s. This prevented any "jet-like" effects occurring from the high-speed PVC pipe to the low-speed enclosure flow. A splash plate in Figure 3.26 was mounted in the plenum entrance to further reduce the jet-like effects of the pipe exit. The air passed through the converter model after leaving the plenum and exited directly into the ambient after passing over the components. The PVC pipe downstream of the LFE and the plenum were both carefully sealed to ensure that all of the air measured passed through the converter model. The plenum connection was sealed internally with Silicone sealant. The vertical corners of the plenum and the seams at the base were also sealed with Silicone sealant. The top of the plenum was sealed with ¼-in. foam weatherstripping so it could be easily removed when the screws were removed. The side where the enclosure connected to the box was cut to fit the box profile tightly, and the seams between the plenum and Lexan enclosure were sealed internally with tape.

Experimental Methodology

The experimental methodology consisted of starting the blower, turning on the power supply, and allowing the heater sides to reach their steady-state temperatures, which usually took slightly longer than an hour. The heater was connected to the power supply with the circuit shown in Figure 3.27.

A 1-Ω precision resistor was connected in series with the heater so the current could be accurately calculated by measuring the voltage across the precision resistor and dividing by the resistance. One issue considered was the resistance of the wires. Since the heater resistance was so small, the wires and heater introduced a voltage divider effect. This became important when the voltage drop across the heater was measured because the voltage across the wire leads would provide an inaccurate measurement of the power actually dissipated by the walls of the heater. The power dissipated by the heater could be calculated as

$$P = VI \tag{3.4}$$

During the testing, four layouts were considered. Most of the measurements were taken with the heater placed directly behind the PFC bulk capacitor, but three other component layouts were also considered. The four layouts are shown in Figure 3.28.

The experiments were conducted according to the test plan outlined in Table 3.8 to determine the heater temperatures for several different situations. The experiment number, the layout number, the volume flow rate, and the mass flow are presented for each case.

The data acquisition (DAQ) hardware used was a National Instruments PCI-MIO-16XE-50 DAQ system, which was connected to an SCXI-1102 Module. The thermocouples were connected into the SCXI-1102 Module, which amplified the signal with a gain of 100. The DAQ system had an input voltage range of ±10 V, and it recorded data in a differential mode with 16-bit resolution. The resolution of this system, which is the smallest detectable change in voltage, is 3.1 μV as calculated using

$$\text{Resolution} = \frac{\text{Voltage Range}}{\text{Gain} \times 2^{\text{bits of resolution}}} \tag{3.5}$$

The difference in thermocouple output voltage for a single degree change at a temperature near 45°C is approximately 63 μV. These two values indicate that a voltage change of 3.1 μV represents a change of 0.05°C. Therefore, the resolution of the measurements taken is ± 0.05°C.

Uncertainty Analysis

An uncertainty analysis was performed on the heater power measurements, the pressure measurement, and the temperature measurements. The uncertainty of the volume flow rate was determined for the 20 cfm case. The pressure drop through the LFE was measured by a pressure transducer, and the pressure drop was correlated to a volume flow rate via a calibration curve. For a volume flow rate of 20 cfm, an average pressure drop of 1.52′′ H_2O was recorded. A series of several samples resulted in a

precision uncertainty of 0.03′′ H_2O, whereas a bias uncertainty of 0.01′′ H_2O was given from the transducer data. Combining the two uncertainties with

$$u = \sqrt{u^2_{bias} + u^2_{precision}} \tag{3.6}$$

produces an overall uncertainty. The result is an overall uncertainty of 0.03′′ H_2O. The calibration curve that represents the conversion of pressure drop in inches of H_2O to volume flow rate in cfm is given as

$$Q = 13.0873\Delta 3 - 0.0565010\Delta P^2 \tag{3.7}$$

The uncertainty in the volume flow rate can be found with the Kline and McClintock (1953) derivative method, which is extremely helpful for finding the propagation of uncertainty in variables to the result. The general form of this method is

$$u_R = \pm\sqrt{\sum_{i=1}^{L}\left(\frac{\partial R}{\partial x_i}\bigg|_{x=\bar{x}} u_{xi}\right)^2} \tag{3.8}$$

where L represents the number of independent variables, and R represents a result of some function of independent variables, x. The velocity is related to the pressure measurements by

$$u_Q = \pm\sqrt{\left(\frac{\partial(13.0873\Delta P - 0.0565010\Delta P^2)}{\partial \Delta P}\right)^2} \cdot u_{\Delta P} \tag{3.9}$$

The pressure drop uncertainty propagates through the calculation and results in a volume flow rate uncertainty of 0.37 cfm. The final volume flow rate indicated by the pressure transducer is 19.84 ± 0.37 cfm (1.9% uncertainty).

The uncertainties affecting the DC heater power measurements come from inaccuracy in measuring the current through the circuit and the voltage across the heater.

A Fluke 75III hand-held digital multimeter was used to measure the voltage across the heater faces and across a 1-Ω precision resistor. The uncertainty of the multimeter is 0.3% of the reading plus one least significant digit of the measurement range. The uncertainty of the 1-Ω resistor is 1%. The precision resistor was used to measure the current, which was then multiplied by the voltage across the heated surfaces to find the power dissipation. This calculation was only done in this manner for the lowest three power dissipation levels. For the case in which 3.69 W were dissipated, the current was greater than 10 A, which would overload the precision resistor. Instead, the 1.69-W case was used to calculate the resistance of the heater, which could be combined with the heater voltage to find the power loss. The Kline and McClintock (1953) method was again used to calculate the uncertainty propagation through the power dissipation calculations. The heater voltages, currents, and uncertainties are given in Table 3.9.

The uncertainty in the thermocouples was also considered. The bias uncertainty in thermocouples is typically 0.2°C. This is lower than the uncertainty data given by Omega, Inc., but it is a more specific rule of thumb based on experimental experience. Five thermocouples, the middle thermocouple on each side of the box plus the inlet air thermocouple, were sampled 10 times each to find a standard deviation value from which the precision uncertainty could be calculated. For a 95% confidence interval a multiplier of 2.228 was obtained from the student "t" distribution to obtain the precision uncertainty. The bias and precision uncertainties could be combined into one overall uncertainty per thermocouple using

$$u = \sqrt{(u_{bias})^2 + (u_{precision})^2} \tag{3.10}$$

Table 3.10 lists the thermocouples with the uncertainties associated with them. The greatest uncertainty given was that of thermocouple 4-2, which is on the back side of the heater element. This is a location where the flow field is not as steady as it is surrounding the rest of the heater and uncertainty would be expected to be higher. The typical thermocouple uncertainty steadily lies around 0.20°C.

Experimental Results

The cases listed in Table 3.8 were simulated in I-deas. The inlet temperatures were subtracted from both the experimental results and computations, allowing temperature rises above ambient to be compared for the two sets of results. Figure 3.29 shows a comparison of Case 10 in Table 3.8. Three temperatures in degrees Celsius are given for each thermocouple location. These represent an experimental temperature rise, a computational temperature rise, and the difference between the two. The difference between the predictions and experiments was found by subtracting the computational temperature from the experimental temperature. Therefore, a positive difference indicates that I-deas under-predicted the experimental temperature, and a negative number indicates over-prediction.

The experimental temperature results for every test case in Table 3.8, along with the computational results and comparisons, are given in Appendix D. The results are shown in a manner similar to Figure 3.29, and many of the trends discussed in this section can be observed from a number of the test cases.

As can be seen from the comparisons, the smallest error between the predictions and experiments occurs on the front face of the heater and the upstream sides of the side walls. The predicted temperatures do not vary as widely as the experimental temperature results. Though comparisons are close on the front face, difference increases as locations closer to the downstream side of the heater are observed. The experimental temperature rise nearly doubles between the front and the back, while the computational temperature rise remains more constant throughout the range of thermocouple locations.

A comparison of the experimental and computational differences for Cases 2-5 is shown in Figure 3.30, and the same comparison for Cases 7-10 is shown in Figure 3.31. The differences in Figure 3.31 are not as great as in Figure 3.30. With an increase in air velocity, and therefore an increase in Reynolds Number, the predictions of component temperatures agree more closely with the experiments. Natural convection has a smaller effect at higher flow rates, and the flow field is more predictable in the 20cfm cases.

The differences between the temperatures in Figure 3.33 range from 0.2°C to 12.8°C. A range of compared values this broad is typical throughout the cases tested. A consistency among thermocouple locations, however, shows some locations are more

difficult to predict than others. For example, a comparison of the temperature rises for each thermocouple for Case 7 of Table 3.8, in which 0.31W of power is dissipated, is plotted in Figure 3.32. Case 10 is plotted in Figure 3.33. The amount of power dissipated in Case 10 is approximately 12 times greater than the power dissipated in Case 7. As might be expected, the temperature difference scales, as well. The scales in Figure 3.32 and Figure 3.33 are different by a factor of 12, but the general trend is similar for both comparisons. Even though some of the predictions may not compare well with the experiments, general trends in predicted temperatures have shown to be consistent, which is an extremely important requirement for the reliability of parametric studies in which temperature changes over several cases must compare well to each other.

Another comparison shows the temperature differences at each thermocouple location plotted versus the power dissipation. Figure 3.34 and 3.35 show the thermocouples that compare the best with the computational predictions, and a comparison between the two graphs gives another indication of the increased accuracy of comparisons for the high Reynolds Number case. The thermocouples along the front of the heater compared best with the predictions, and those along the back wall showed the greatest inaccuracy. On the side walls, thermocouples 1-3 and 3-1, the two closest to the front face, showed a better comparison than the other two thermocouples on each wall.

The uncertainty analysis indicated that the uncertainty in the power dissipation of the heating element was 0.05W. A simulation with a flow rate of 20 cfm and a power dissipation of 3.74 W (Normal dissipation plus uncertainty) showed a slight increase in the heater wall temperatures. The temperature differences, however, were within the uncertainty of the thermocouples, and this verifies that the thermocouples dominate the uncertainty in the measurements and no new accuracy due to the power dissipation uncertainty can be explored. The temperature comparisons shown in the same manner as in Figure 3.29 are shown in Figure 3.36. A more complete uncertainty analysis on the simulations would include not only the power dissipated by the heater but also all other input parameters to the model, such as fan flow rate, material properties, and geometric properties. This would potentially show enough uncertainty in the simulated temperatures to allow the simulated and experimental temperatures to match each other.

This chapter has outlined the experiments performed to benchmark the code I-deas to determine suitable operability and temperature prediction. Studies were set up to test circuits directly, compare with previously performed work, qualitatively identify complex flow effects, and to compare I-deas predictions with a controlled experiment. Results for all cases were varied, and some predictions were extremely close to experiments and compared very well, while a few others showed major discrepancies from the experimental work. Overall, the final experiment provided a good apparatus for studying the prediction capability of I-deas for a number of flow surfaces.

Table 3.1. Experimental Test Results

Case	Title	Instrumentation	Goals
1	Test Circuits	Thermocouples	Compare I-deas system level predictions with experimentally measured temperatures
2	MOSFET / Heat Sink*	IR Camera	Study semiconductor / heat sink interactions and validate the assumption of perfect contact
3	Flow Visualization	Digital Camera	Verify the existence of vortices predicted by I-deas
4	Controlled DC Heater	Thermocouples	Compare simulated temperatures to experiments run under the same conditions

*Experiments performed by Pang (2001)

Table 3.2. Thermocouple Locations

#	PFC Filter		DC/DC Converter	
1	Heat Sink Middle	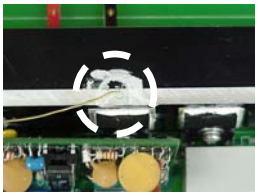	Secondary Diode	
2	Heat Sink Front	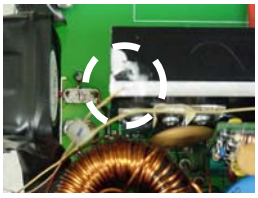	MOSFET 1	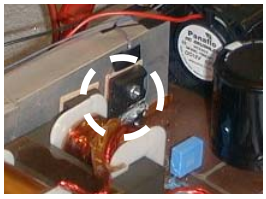
3	EMI Inductor	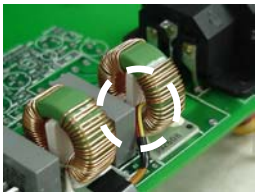	Bulk Capacitor	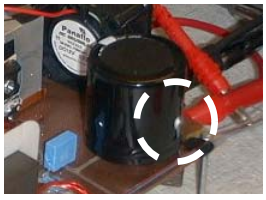
4	Boost Inductor	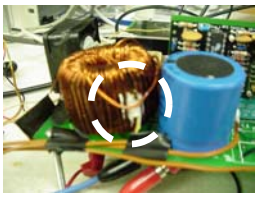	Output Capacitor	
5	Bulk Capacitor	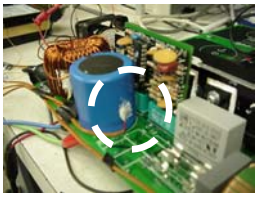	Transformer Winding	
6	Inlet Air	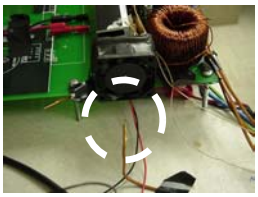	Outlet Air	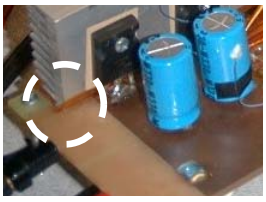

Table 3.3. PFC Filter and DC/DC Converter Test Circuit Measurements and Simulations

PFC Filter				DC/DC Converter		
#	Measured (°C)	Predicted (°C)		#	Measured (°C)	Predicted (°C)
1	42	55		1	56	45
2	38	50		2	31	47
3	81	56		3	27	44
4	68	61		4	46	67
5	42	43		5	59	67
6	24	22		6	34	32

Table 3.4. Analytical MOSFET Temperature Calculations for the Baseline Case

Location	ΔT (°C)
Junction (T_J)	17.7
Case (T_C)	13.5
Surface (T_S)	11.4
Heat Sink (T_{sink})	6.9

Table 3.5. MOSFET Parametric Study Case Descriptions

Case	Gap (mm)	Resistance (°C/W)	Conductance (W/mK)	Heat Source	Materials
1	-----	-----	-----	Uniform	Steel
2	0.15	0.80	-----	Uniform	Steel
3	0.15	0.80	-----	Bottom	Plastic
4	0.15	-----	1.3	Bottom	Plastic
5	0.15	0.80	1.3	Bottom	Plastic
6	0.15	-----	1.3	Middle (Si)	Cu,Si,Plastic

Table 3.6. Inaccuracies Addressed by Experimental Setup

Number	Inaccuracy	Solution
1	Unknown power dissipation	DC resistive heater
2	Fan curve unreliability	Used blower instead of fans
3	Heat transfer between components	No other components heated
4	PCB conduction	Box base made of insulative Lexan
5	Boundary heat transfer	Sides and top made of Lexan
6	Disturbed flow field	Thermocouples run out along base

Table 3.7. Heater Material Properties

Material	Thermal Conductivity (W/mK)
Steel foil	15
Balsa wood	0.05
Styrofoam	0.01
Epoxy	0.2

Table 3.8. Experimental Test Cases

Experiment #	Layout	Flow rate (cfm)	Power (W)
1	1	10	0.00
2	1	10	0.31
3	1	10	0.94
4	1	10	1.69
5	1	10	3.69
6	1	20	0.00
7	1	20	0.31
8	1	20	0.94
9	1	20	1.69
10	1	20	3.69
11	1	5	3.69
12	1	10	3.69
13	1	15	3.69
14	1	20	3.69
15	1	20	3.69
16	2	20	3.69
17	3	20	3.69
18	4	20	3.69

Table 3.9. Heater Power Measurements and Uncertainties

Case	Voltage (V)	$u_{voltage}$ (V)	Current (A)	$u_{current}$ (A)	Power (W)	u_{power} (W)
0.31W	0.104	0.000	2.99	0.03	0.31	0.00
1.04W	0.189	0.001	4.98	0.06	0.94	0.01
1.69W	0.241	0.001	7.02	0.08	1.69	0.02
3.56W	0.356	0.002	10.37	0.13	3.69	0.05

Table 3.10. Thermocouple Uncertainty Analysis

Thermocouple	Temperature (°C)	u_{bias} (°C)	$u_{precision}$ (°C)	u (°C)
1-2	46.7	0.20	0.04	0.20
2-2	42.7	0.20	0.03	0.20
3-2	43.5	0.20	0.03	0.20
4-2	50.0	0.20	0.13	0.24
Air	24.0	0.20	0.08	0.22

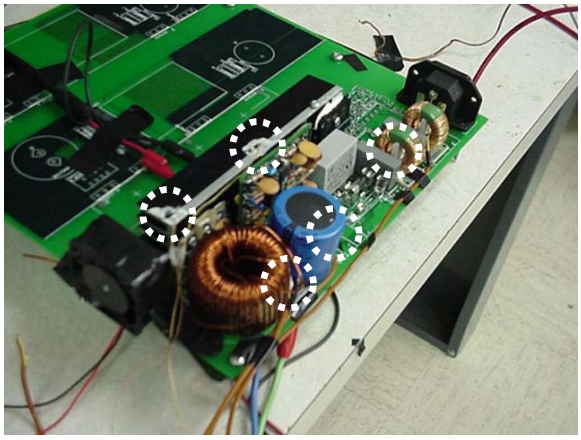

Figure 3.1. The PFC filter, designed by Zhao (2001), served as a rectifier for the incoming AC signal. Temperature measurement locations are circled.

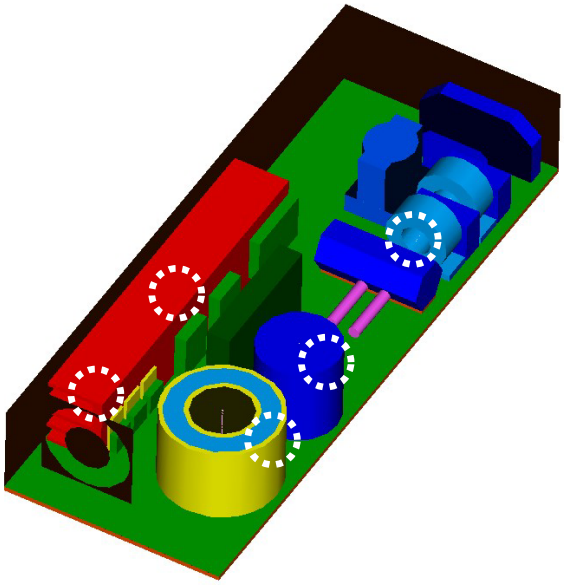

Figure 3.2. A model of the PFC filter was drawn and simulated in I-deas. Temperature comparison locations are circled.

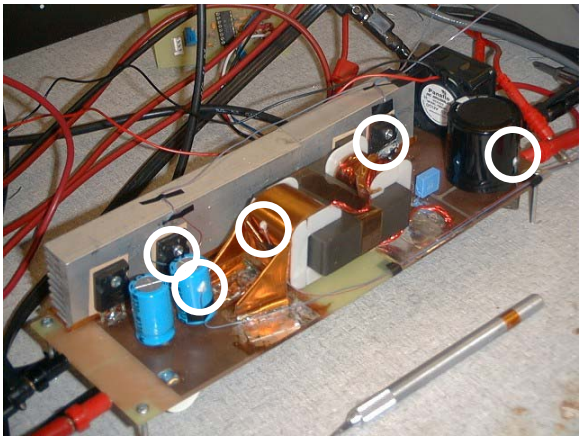

Figure 3.3. The DC/DC converter, designed by Yang (2001), steps the DC voltage output by the PFC down to a useful DC signal. Temperature measurement locations are circled.

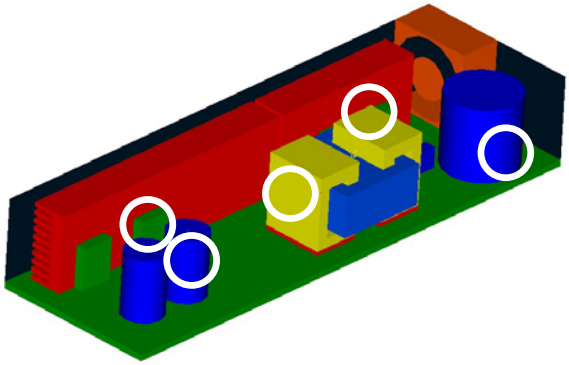

Figure 3.4. The DC/DC converter I-deas model, designed by Yang (2001), was drawn and simulated to compare with the test circuit. Temperature comparison locations are circled.

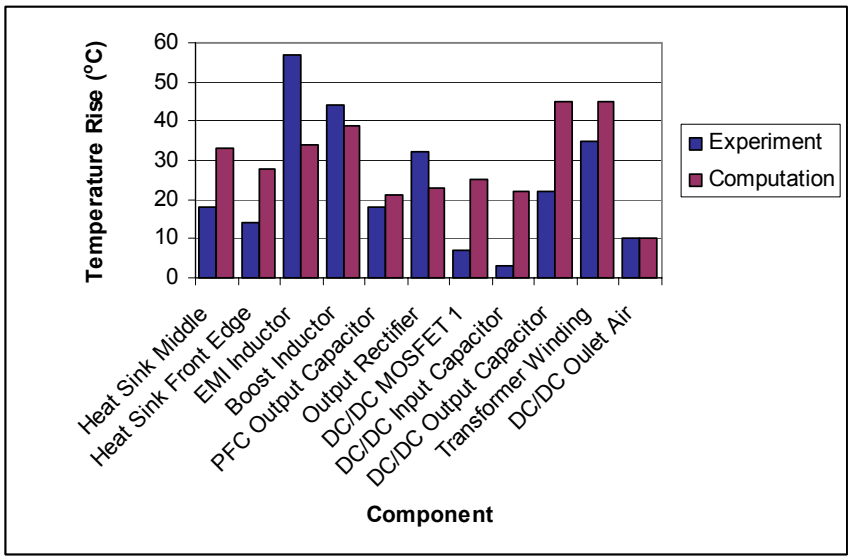

Figure 3.5. The temperature measurements and I-deas temperature predictions did not compare very well for the test circuit components.

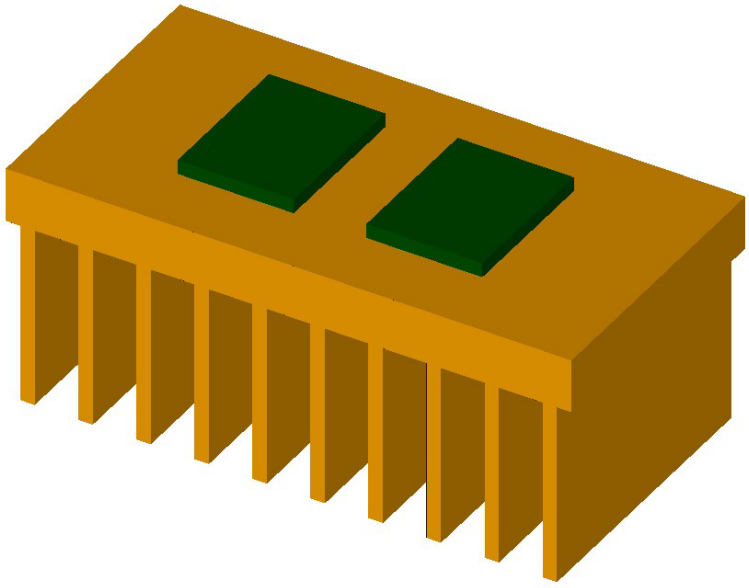

Figure 3.6. A simple configuration was set up to study the variations in simulating the thermal interface between a MOSFET and heat sink.

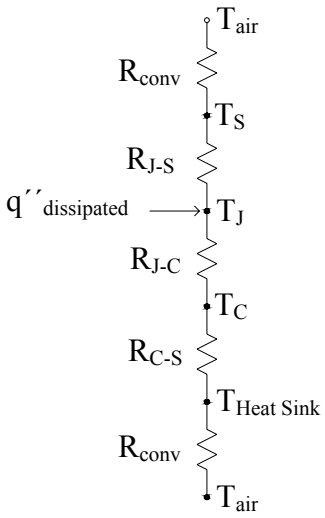

Figure 3.7. A resistance network is a convenient way to solve for the temperatures distributed throughout the semiconductor / heat sink configuration.

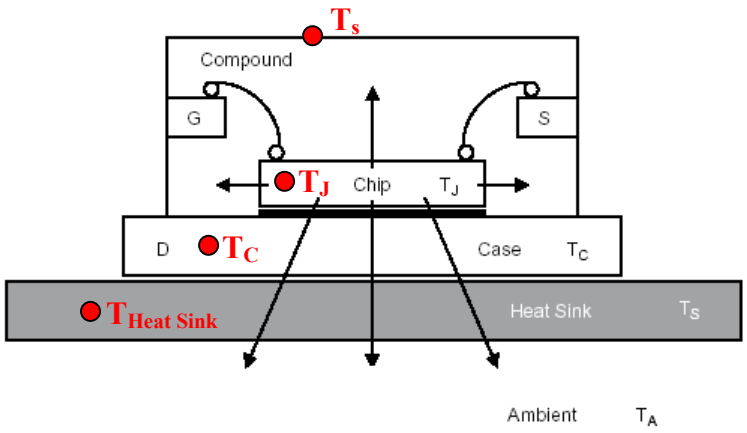

Figure 3.8. The most important temperatures to know on a semiconductor are the surface, case, and junction temperatures.

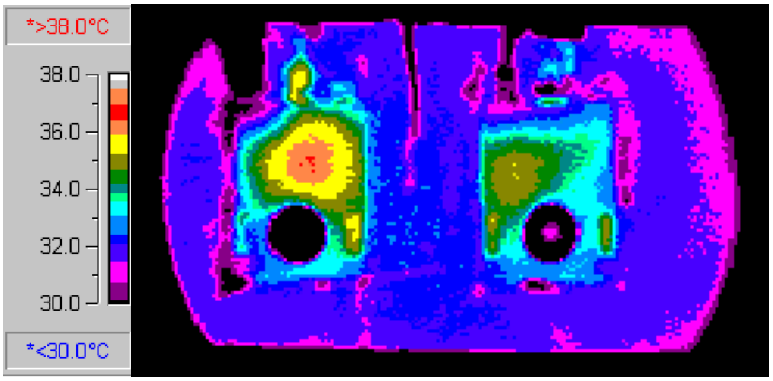

Figure 3.9. The IR camera showed a maximum temperature of approximately 37°C on the surface of the MOSFET.

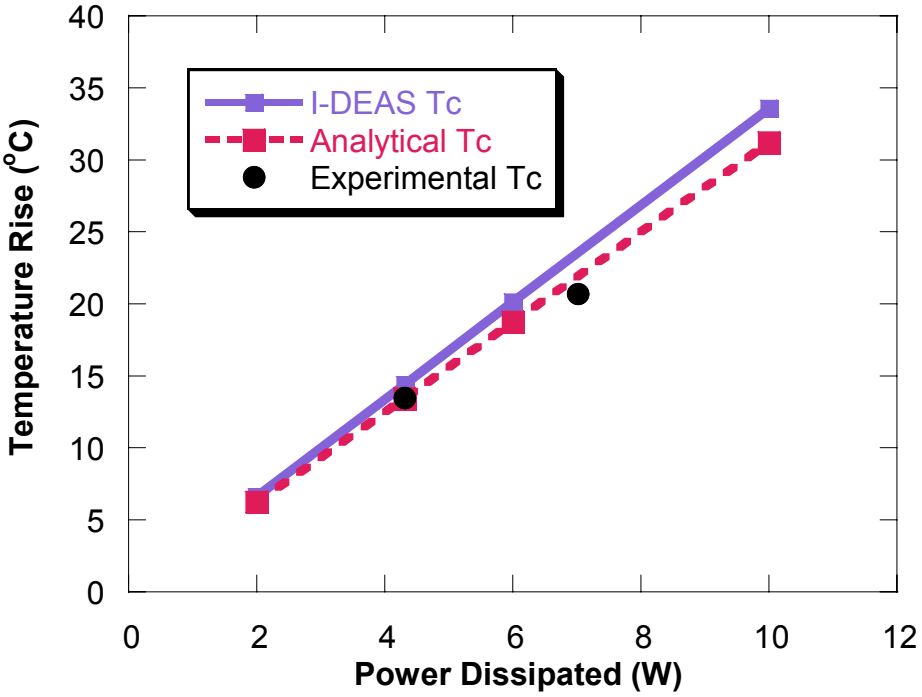

Figure 3.10. One of the simulated cases and two of the calculations compared very closely to the experimental data.

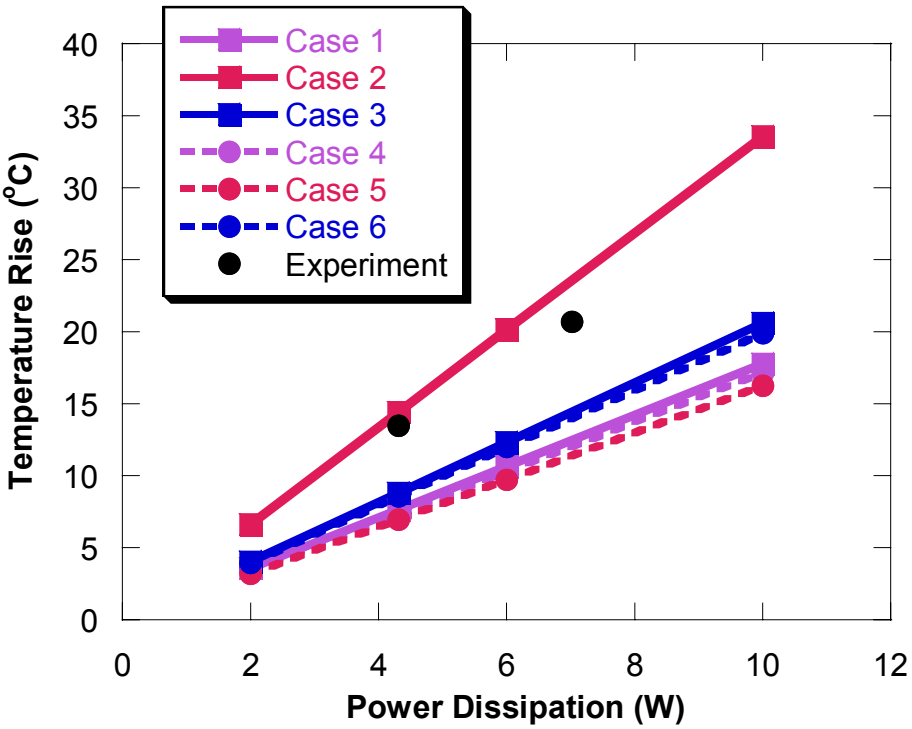

Figure 3.11. The other simulated cases were similar to each other but did not compare as well to the experimental data as Case 2 (Refer to Table 3.5).

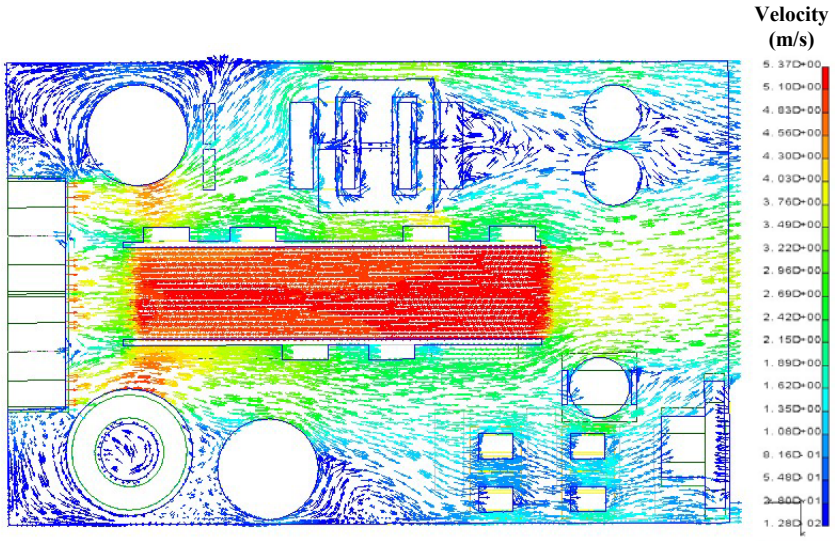

Figure 3.12. A plane 2cm above the base indicates the presence of complicated flow field patterns.

Figure 3.13. The experimental setup consists of the Lexan box, an atomizer, a power supply for the fans, a light, a tripod, and a digital camera.

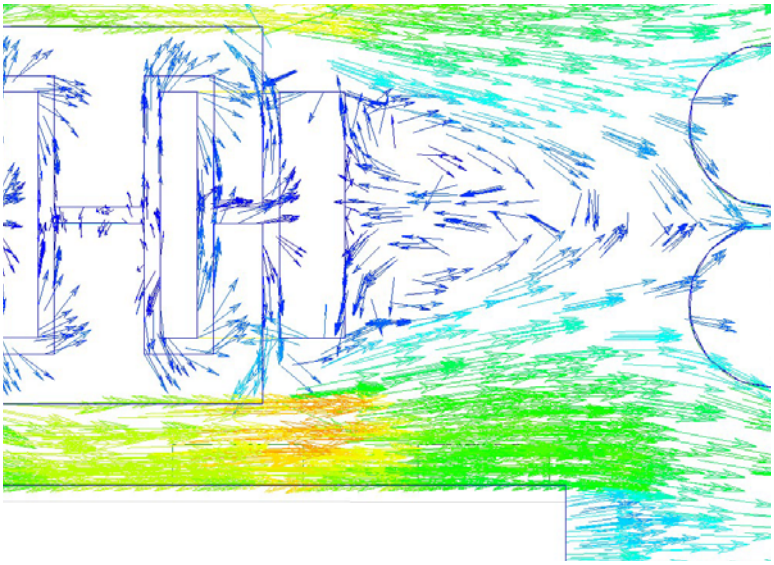

Figure 3.14. The simulations indicated the presence of a pair of vortices located directly behind the transformer.

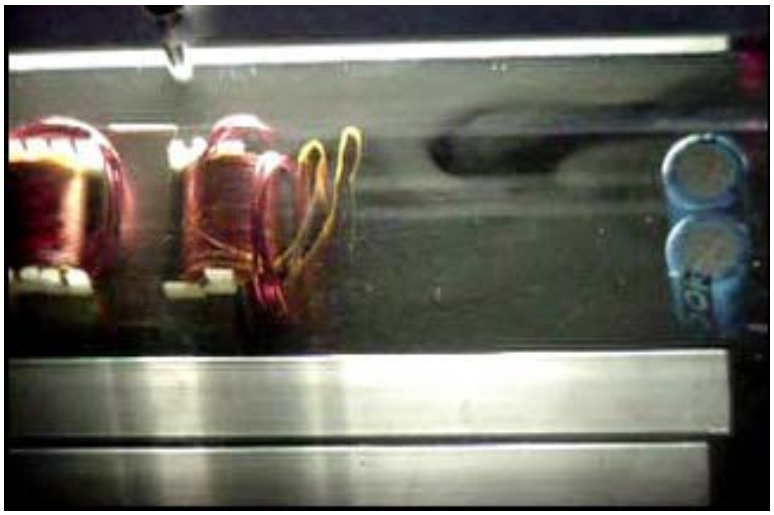

Figure 3.15. Flow visualization indicates the presence of a vortex in approximately the same location as the vortices in the simulation.

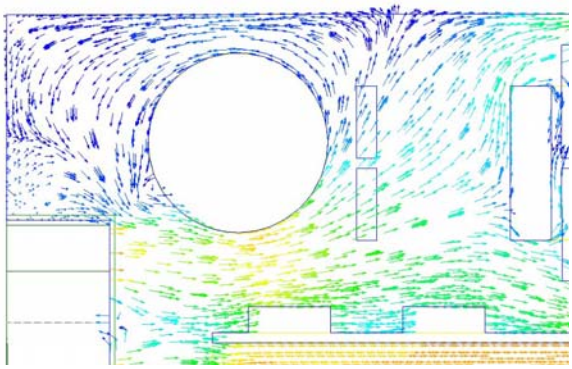

Figure 3.16. The presence of swirling flow in the corner of the enclosure could impede cooling of nearby components.

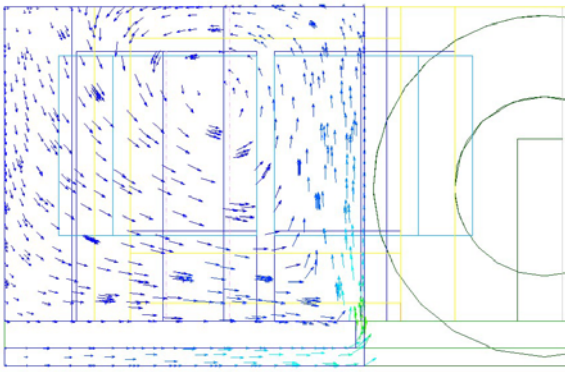

Figure 3.17. A front view (from the left side of Figure 3.18) reveals a presence of vertical swirling in the corner of the enclosure.

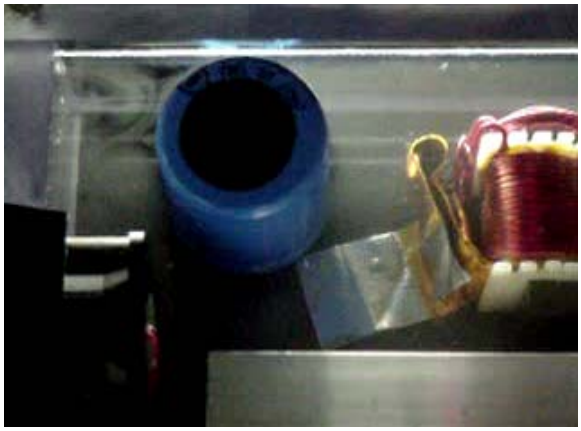

Figure 3.18. The vortex in the enclosure corner was predicted by the I-deas CFD simulation.

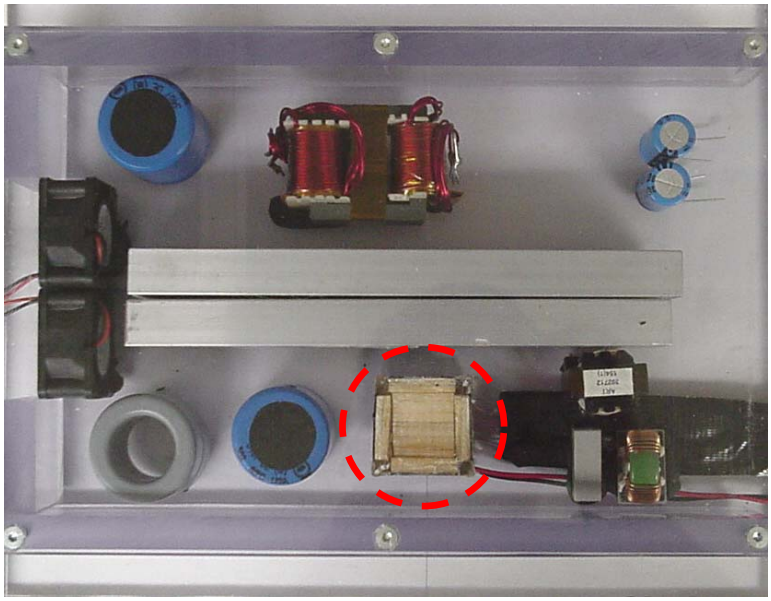

Figure 3.19. A DC heater component was introduced into the system to study temperature prediction of a component in a realistic flow field.

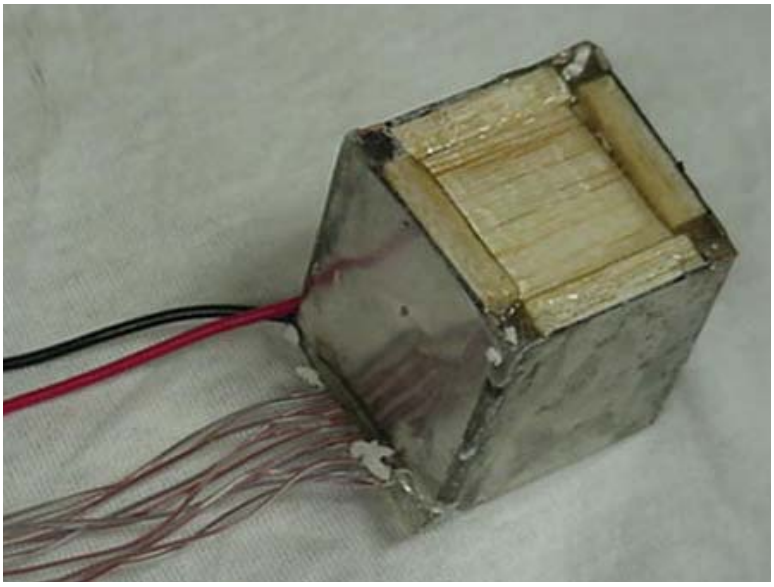

Figure 3.20. The DC heater could measure the wall temperatures resulting from a constant known heat flux.

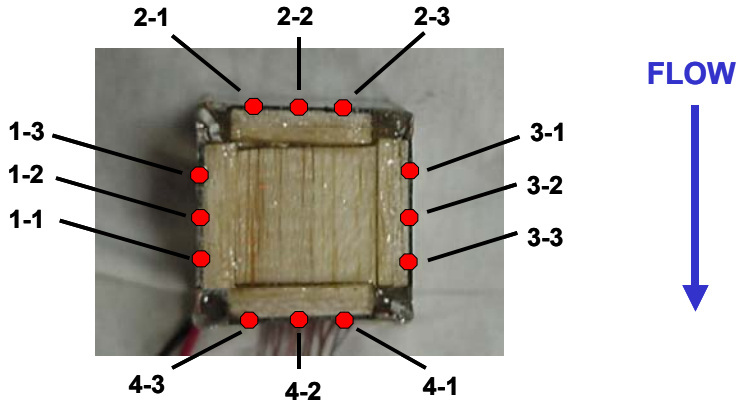

Figure 3.21. The twelve thermocouples (top view) were arranged to allow the temperature distribution across a side to be measured.

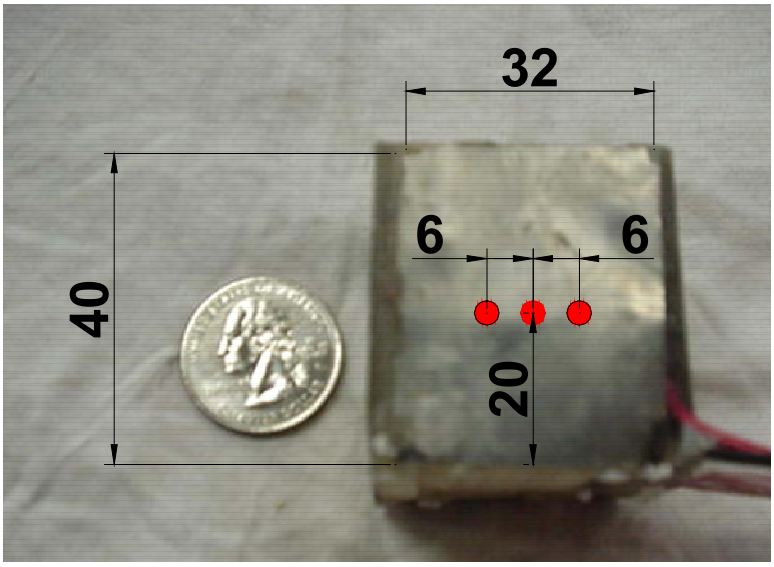

Figure 3.22. Three thermocouples are centered vertically on each side of the component (Dimensions in mm).

Figure 3.23. The experimental setup used a blower to introduce a known flow rate into the enclosure instead of using the system fans.

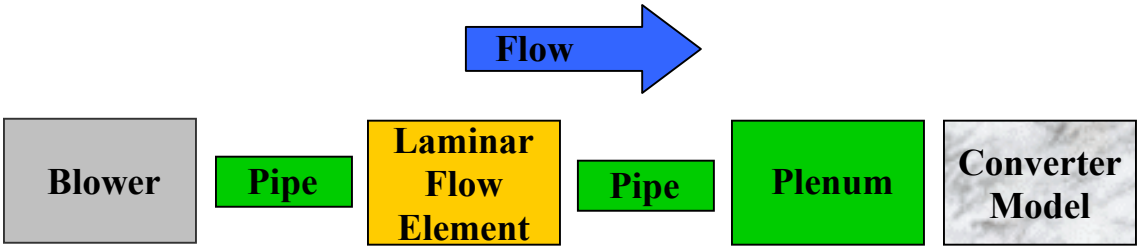

Figure 3.24. A blower forces air through a measurement system and into the model of the front-end converter.

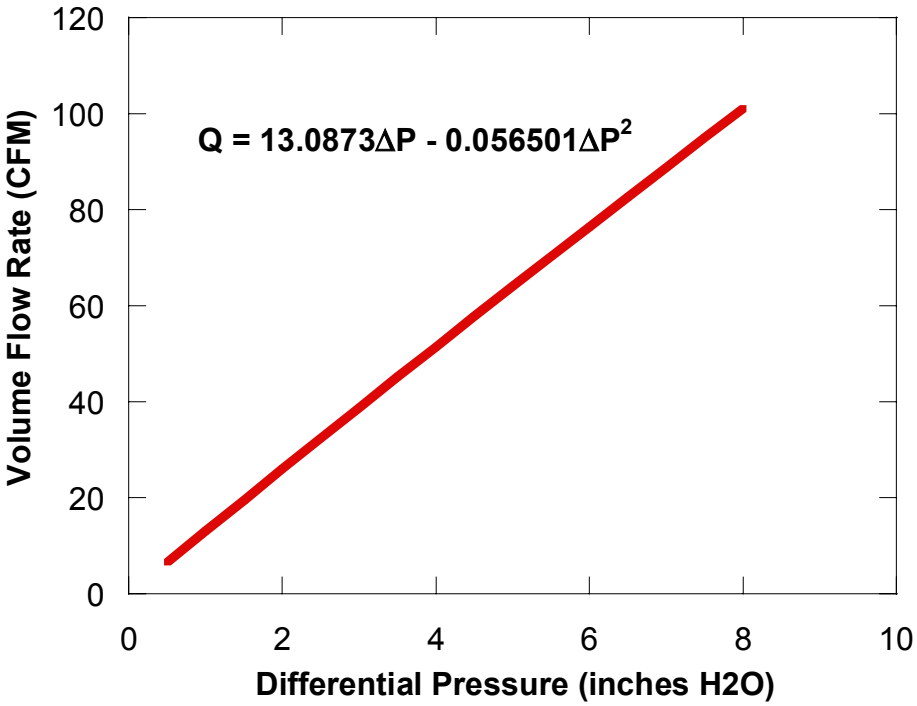

Figure 3.25. The calibration curve relates the volume flow rate to the pressure drop across the LFE.

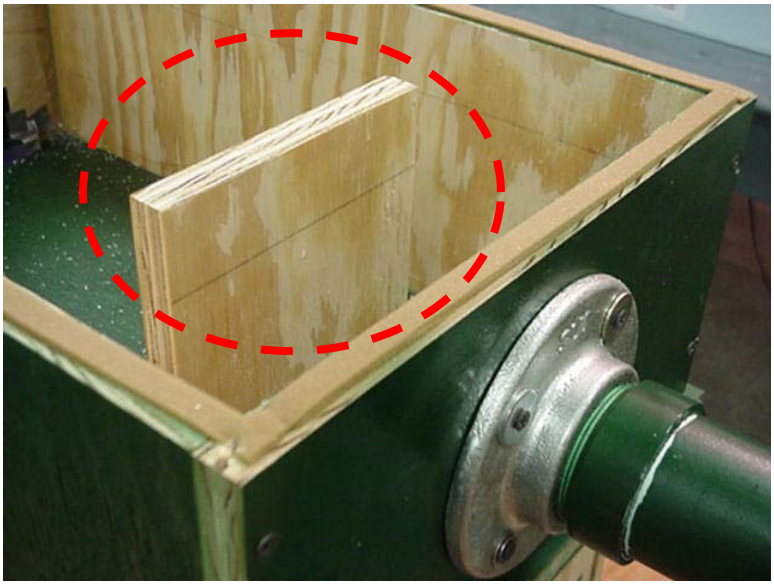

Figure 3.26. A splash plate receiving the flow from the PVC pipe helped to decrease the air velocity.

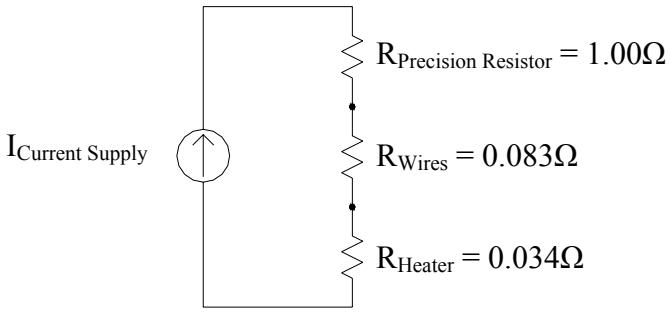

Figure 3.27. A current source connected to a precision resistor and the DC heater allowed the heat flux to be varied with current.

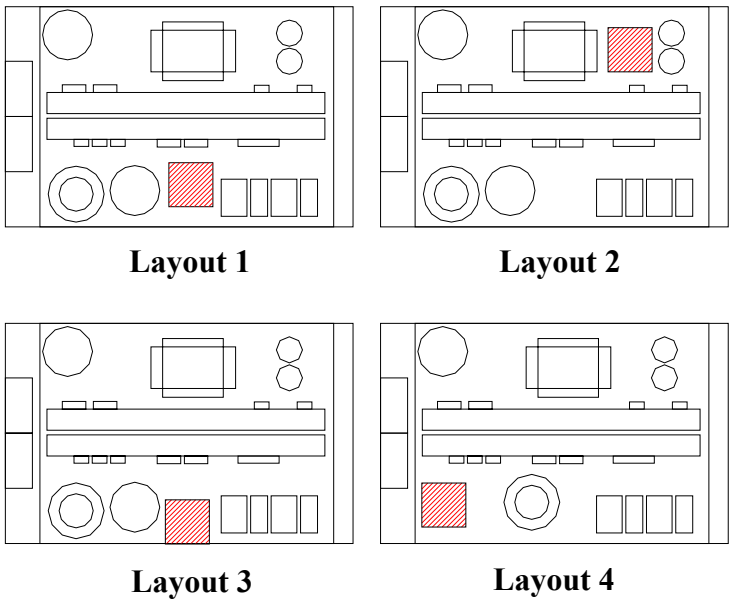

Figure 3.28. The four component layouts were tested to observe I-deas prediction of different configurations.

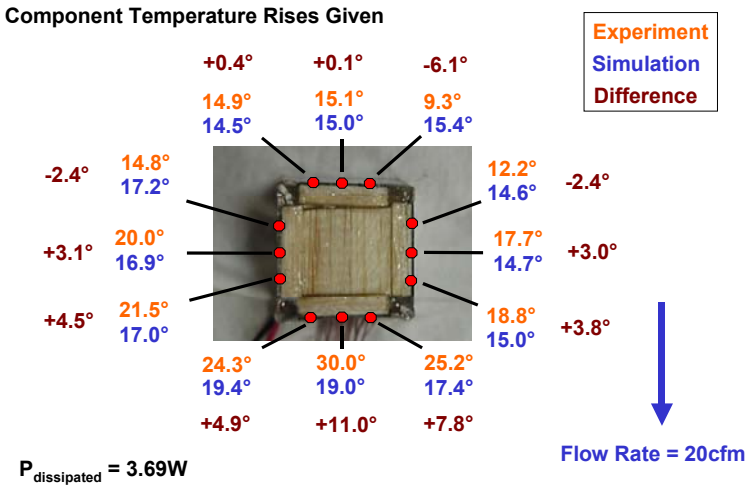

Figure 3.29. A comparison of predicted and experimental temperatures shows a range of differences.

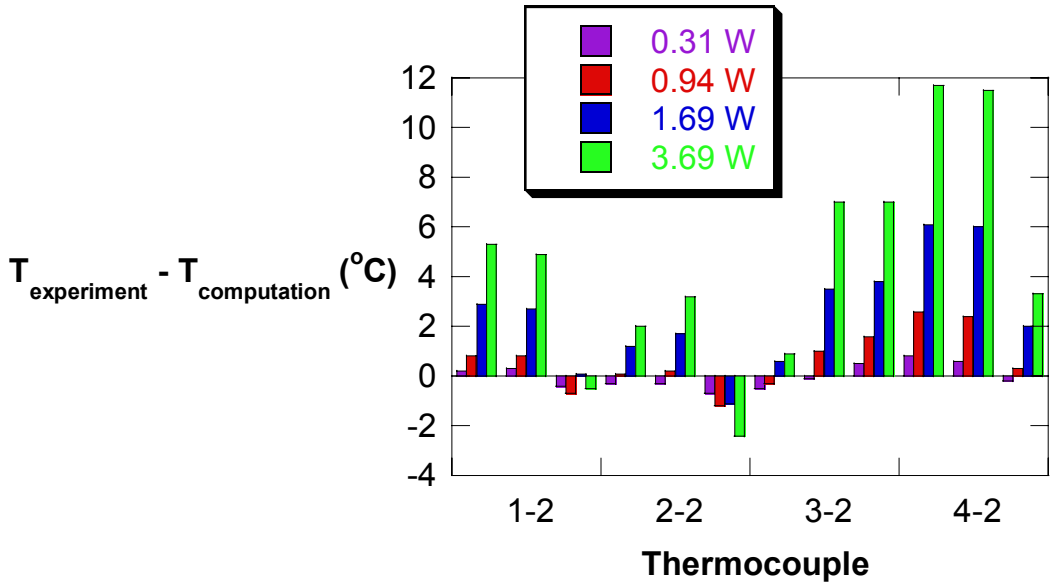

Figure 3.30. The temperature comparisons for the cases with a volume flow rate of 10cfm show a range of differences.

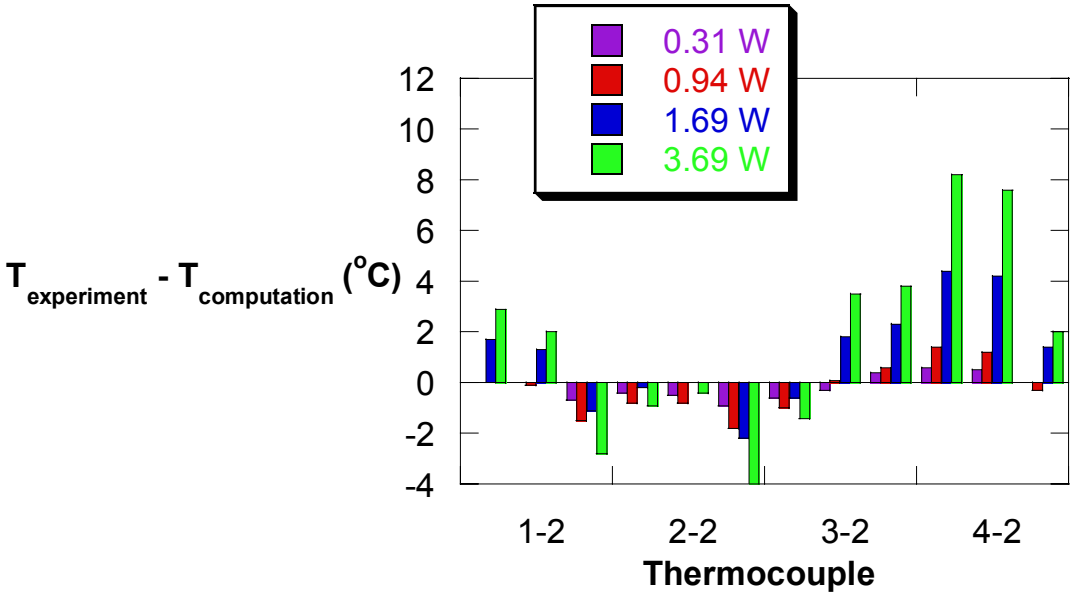

Figure 3.31. The comparisons for the 20 cfm case were slightly smaller than those for the 10 cfm case.

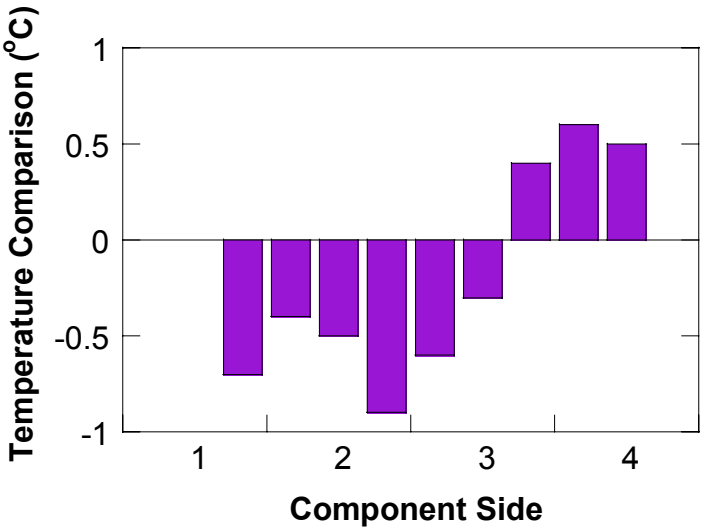

Figure 3.32. 0.31 W of power were dissipated in Case 7.

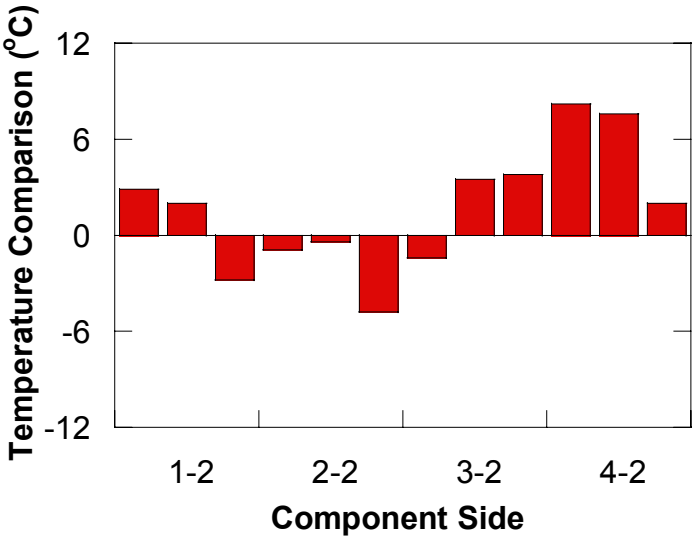

Figure 3.33. 3.69 W of power were dissipated in Case 10.

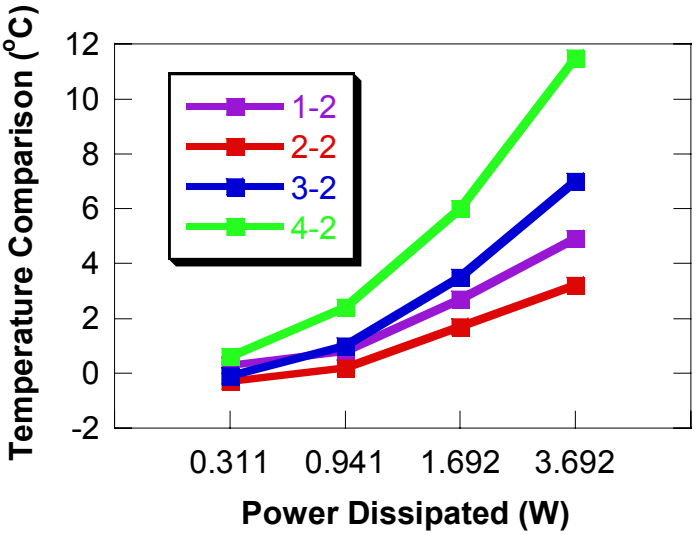

Figure 3.34. The cases with a flow rate of 10cfm showed a range of differences between experiments and computational temperature predictions.

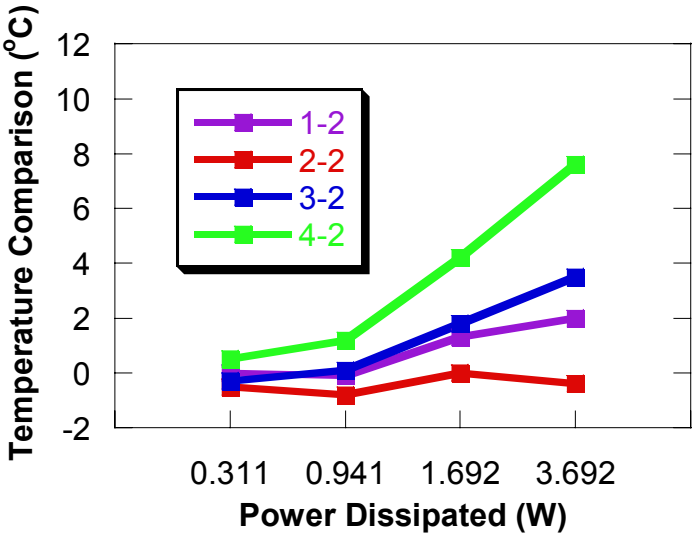

Figure 3.35. The 20cfm cases showed smaller temperature differences when the experiments and predictions were compared.

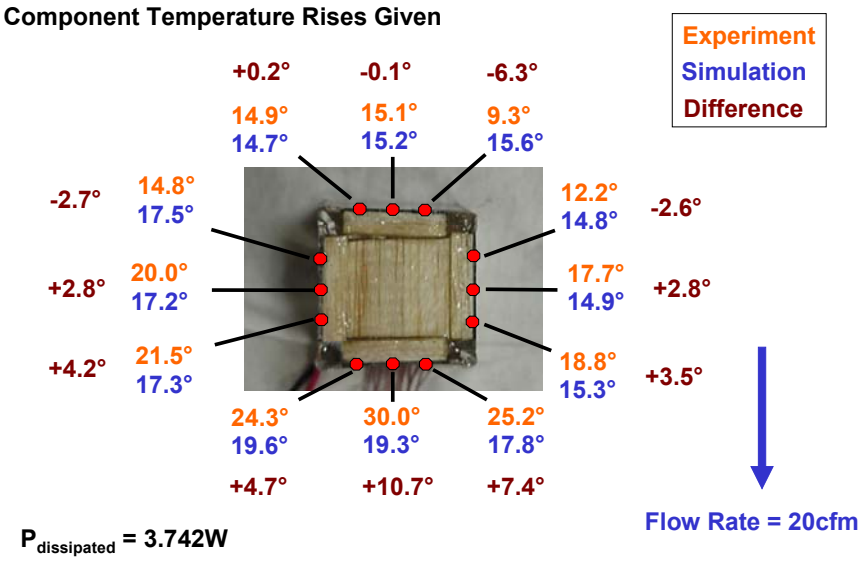

Figure 3.36. Considering the uncertainty in the power dissipation, the simulation with a slightly-increased power loss shows a slight improvement in temperature predictions.

Chapter 4 – Radiation and Exit Grill Effects

Radiation is one of the most ignored effects in the thermal analysis of power electronics. Electronics systems have extremely complex geometries, and since radiation is dependent on all components in a system, a radiation analysis is an intimidating task to undertake. One approach for understanding the impact of radiation upon a system is called the Monte Carlo ray-trace (MCRT) method for radiation analysis. This method is discussed in this chapter and used to find the radiation effects for the front-end converter studied in the project.

A second effect that causes uncertainty in component temperature prediction is exit grill effects. The additional pressure losses across the grill are difficult to model. A computational study of different modeling methods is discussed, comparing the sensitivity of temperature and velocity fields to changes in exit vent modeling.

This chapter begins with a radiation analysis of the converter described in Chapter 2. First, the traditional method of radiation heat transfer is described. A brief description of this net exchange method is followed by an explanation of the MCRT method of radiation analysis and the code used to perform the analysis. An analysis is done using the MCRT method directly to determine radiation heat transfer from each component, and the MCRT code is used to obtain the shape factors for the critical components to be included in an I-deas simulation. Simulation results of exit grill effects are also discussed later in the chapter. Four different cases were explored, and the component temperatures for each modeling variation were compared to each other to examine the temperature sensitivity to exit grill modeling.

4.1 Radiation

Three modes of heat transfer move the heat generated by an electronic component away from that component and into the system. They are conduction, convection, and radiation, and they are illustrated in Figure 4.1. If the heat generated is not transferred to the surroundings, it will be used to increase the temperature of the component. This is shown by the equation for an energy balance for a component,

$$Q_{in} + Q_{gen} - Q_{out} = Q_{st} \tag{4.1}$$

where Q_{in} is the energy transferred to the component from the system [W],

Q_{gen} is the energy generated by the component [W],

Q_{out} is the energy transferred to the surroundings [W], and

Q_{st} is the energy stored by the component [W].

Very little heat is transferred to the components from any external sources. If the air temperature upstream is greater than the component temperature or the temperature of the PCB is greater than that of the component, heat would be transferred to the component, but this heat transfer, if present, is expected to be small so the value of Q_{in} is assumed to be zero. The quantity Q_{gen} is the given amount of power dissipated by each component and is assumed constant throughout system operation. The quantity Q_{out} is determined by the presence of convection and radiation heat transfer (conduction is assumed to be negligible). The quantity Q_{st}, the energy stored, represents the change in internal energy of the control volume. The value of this term becomes zero as components reach steady state. The steady-state energy balance equation for a component in terms of heat fluxes is

$$q'''_{gen} V - q''_{conv} A - q''_{rad} A = 0 \tag{4.2}$$

where q'''_{gen} is the volumetric heat generation of the component [W/m^3],

V is the volume of the component [m^3],

q''_{conv} is the heat removed by convection [W/m^2],

A is the surface area of the component [m^2], and

q''_{rad} is the net radiation heat transfer from the component [W/m^2].

In equation 4.2, the heat generated is equal to the heat removed by convection and radiation. Heat removed by conduction into the PCB is neglected. If the net radiation heat transfer is positive and heat is transferred away from the component, the component temperature would be lower and the value of the convection heat transfer would be smaller as well. The convective heat flux is dictated by the flow field and temperature difference, as described by

$$q''_{conv} = h(T_{component} - T_{\infty}) \tag{4.3}$$

where h is the heat transfer coefficient [W/m^2K]. The heat transfer coefficient, h, is a function of the flow field only, and it remains constant whether radiation is included in the analysis or not. Radiation and convection are closely coupled, however. In electronics situations, the heat transfer of components shown to have significant radiation heat fluxes will not be dominated by either effect. When radiation heat transfer is introduced into a convection analysis, a component temperature might be found to change. This change affects both the convection and the radiation heat transfer from the component, making it extremely difficult to solve for the component temperature since the convection heat transfer and radiation heat transfer were solved using different methods. Therefore, the goal of the radiation analysis will be to discover which components transfer a significant amount of heat to the surroundings by way of radiation. These components will then be included in the I-deas analysis.

Net Exchange Method

The net exchange method is the traditional way of performing a radiation heat transfer analysis. In this method, the amount of radiation leaving a surface is compared to the amount of radiation arriving at another surface by a view factor.

Using the view factor, the radiation heat flux from one surface, surface i, at a known temperature to another surface, surface j, at a known temperature can be found. Finding the total amount of radiation absorbed by or emitted from a surface involves summing the net radiation exchange between the surface in question and every other surface within the system. If the heat fluxes for the surfaces are known, this involves inverting an n x n matrix for n number of surfaces to find the surface temperatures.

Several assumptions, listed in Table 4.1, must be made before the net exchange method can be used to solve heat transfer problems. Most of these assumptions can be made without causing significant uncertainty in the final temperatures, but some are very risky to make and can lead to inaccurate results.

The physical principles behind any method for radiation heat transfer are the same, but the MCRT method describes some of the physics slightly differently than the net exchange method. Though it makes so many simplifying assumptions, the net exchange method is valuable to know in this case because it can be input into I-deas via the gray body view factor (GBVF), which is determined by the geometrical relationship between components. This one parameter governs the radiation heat transfer between any two surface meshes in the finite element model. The equation solved by I-deas describing the magnitude of the radiative conductances created between two surfaces is

$$\text{Conductance} = \sigma \, \text{GBVF} \, \varepsilon \, A \, (T_{hot}^2+T_{cold}^2)(T_{hot}+T_{cold}) \qquad (4.4)$$

The view factors can be found with a method similar to the one described in the next section. The I-deas simulation results for the power supply in this project will be discussed later in this section.

Monte Carlo Ray-Trace (MCRT) Method of Radiation Heat Transfer Modeling

The MCRT method for radiation heat transfer analysis is a statistical method in which the relationships among surfaces are characterized by the total radiation distribution factor, D_{ij}, which is defined as the fraction of radiation *emitted* from surface i that is *absorbed* by surface j. This is different from the net exchange method in that the exchange method view factor is defined by the radiation *leaving* a surface that *arrives at*

another surface. The radiation distribution factor contains all directional and spectral information relevant to the ultimate disposition of thermal radiation emitted from a given surface element. In this project, the total, diffuse-specular radiation distribution factor, D'_{ij}, was used, which is defined as the fraction of total radiation emitted diffusely (in all directions) from surface element i that is absorbed by surface element j, due to direct radiation and to all possible diffuse and specular (in a specific direction) reflections within the enclosure (Mahan, 2002).

If the surface temperatures for all surfaces are known, the radiation heat flux absorbed by element i is given by

$$q''_{i,a} = \frac{1}{A_i} \sum_{j=1}^{n} \varepsilon_j A_j \sigma T_j^4 D'_{ji} \tag{4.5}$$

where A_i is the area of surface i [m^2],

ε_j is the emissivity of surface j,

A_j is the area of surface j [m^2],

σ is Boltzmann's Constant [W/m^2K^4],

T_j is the temperature of surface j [K], and

D'_{ij} is the total, diffuse-specular distribution factor.

The radiation emitted from surface i is defined by

$$q''_{i,e} = \frac{\varepsilon_i A_i \sigma T_i^4}{A_i} \tag{4.6}$$

where ε_i is the emissivity of surface i,

A_i is the area of surface i [m^2],

σ is Boltzmann's Constant [W/m^2K^4], and

T_i is the temperature of surface i [K].

The net radiation heat transfer from a surface is simply the difference between the values given by equations 4.5 and 4.6 as

$$q''_i = q''_{i,e} - q''_{i,a} \tag{4.7}$$

By using this simple analysis, the radiation heat transfer from each component can be found. In the converter simulation, the dominating effect in heat transfer is convection. Knowing exactly how much heat is transferred by way of radiation gives an excellent indication of how much attention should be paid to the radiation effects. If a very small percentage of the heat generated by a component is dissipated as radiation, it can be confidently ignored, but if radiation heat transfer is a significant fraction of the total heat transfer, it should be analyzed more closely (Mahan, 2002).

MCRT Analysis Using FELIX

The MCRT analysis of the converter was implemented with the code FELIX, Functional Environment for Longwave Infrared eXchange (Nevárez-Ayala, 2002). FELIX is a statistical ray-tracing program that emits rays, representing energy bundles, from random locations on emitting elements and uses material properties as probabilities to determine which surfaces absorb the rays. The success of the analysis depends on emitting a statistically significant number of rays so that an entire system is sampled properly. Considering two surfaces i and j, the ratio of the number of rays absorbed by surface j to the total number of rays emitted by surface i is an approximation of the radiation distribution factor, which can be used in the heat transfer analysis described in the previous section.

The AutoCAD model used for the MCRT analysis is pictured in Figure 4.2. A model drawn in AutoCAD describes only the surfaces of the components, which was exported into FELIX. Radiation properties are all surface properties. These surfaces could then be assigned physical properties.

Two physical properties were assigned to each surface, emissivity and specularity. Directional, spectral emissivity is the ratio of the spectral intensity emitted from a surface in direction θ,ϕ to the intensity of a blackbody at the same temperature and wavelength, as described by

$$\varepsilon'_{\lambda}(\lambda, T, \theta, \varphi) = \frac{i_{\lambda,e}(\lambda, T, \theta, \varphi)}{i_{b\lambda}(\lambda, T)} \tag{4.8}$$

The hemispherical, total emissive power is the total power emitted by a surface element at a given temperature into the hemispherical space above that surface element per unit surface area. The hemispherical, total emissivity is the ratio of hemispherical, total emissive power of a real surface to the hemispherical, total emissive power of a blackbody at the same temperature with the same area. This hemispherical, total emissivity is the property value input into FELIX (Mahan, 2002).

The other property assigned to surfaces in FELIX is the specularity ratio, which determines the reflected direction of an incident ray. Recall that one of the assumptions made in the net exchange method was that all surfaces are diffuse. No common real surfaces are completely diffuse, and some surfaces are extremely specular. Figure 4.3 illustrates the difference between diffuse reflection and specular reflection and a combination between the two. Specular reflection can be observed in a room simply by looking for the reflection of a ceiling light on a gray tabletop. Though most of the visible radiation incident to the tabletop is reflected diffusely, it is still possible to see a blurred reflection of the ceiling light at the angle of reflection opposite the light's angle of incidence. Even when light was reflected off of a diffuse surface like the tabletop, a greater fraction of light was reflected specularly than in any other direction (Mahan, 2002).

In FELIX, the specularity ratio, r_s, is defined as the ratio of the specular component of reflectivity to the overall reflectivity. The overall reflectivity is the sum of the specular component of reflectivity and the diffuse component of reflectivity, as given by

$$\rho = \rho^s + \rho^d \tag{4.9}$$

The specularity ratio is

$$r_s = \frac{\rho_s}{\rho} = \frac{\rho^s}{\rho^s + \rho^d} \tag{4.10}$$

In Figure 4.3, drawing (a) shows a specularity ratio between 0 and 1, drawing (b) indicates a specularity ratio of 0, and drawing (c) indicates a ratio of 1. This input allows the radiation properties of surfaces to be modeled much more accurately than they could by the net exchange method (Mahan, 2002).

In the MCRT analysis, a given amount of radiation is divided into a large number of discrete energy bundles, N_i. Each energy bundle is emitted as a ray and traced through the system to its absorption point at surface j, where the variable N_{ij} is incremented. Dividing the two numbers approximates the radiation distribution factor, D_{ij}, as

$$D_{ij} \cong \frac{N_{ij}}{N_i} \tag{4.11}$$

The user determines the total number of rays emitted in a simulation in FELIX. This allows quick, simple simulations to be run to explore general trends and rough approximate values for the radiation distribution factors before more detailed, time-consuming simulations are performed using a higher number of rays. The accuracy of a model depends on the simplicity of the geometry, but it is recommended that 10,000 rays be emitted from each surface element to result in radiation distribution factors estimated to three significant figures (Mahan, 2002).

A pseudo-random number generator is used to determine all decisions made during the analysis in FELIX. A good random number generator is capable of quickly producing numbers that appear random but are uniformly distributed in long, disjoint sequences with periods long enough that no parts of the sequence are repeated. The random number sequence must also be repeatable, which is possible in FELIX by controlling the two seeds, or starting points, for the random number generator (Mahan, 2002).

A pair of random numbers determines the coordinates of the point of emission of a ray on a surface. The ray is either emitted normal to the surface or diffusely (as

determined by the user), in which case another pair of random numbers would determine the direction of emission. Random numbers continue to make decisions such as whether a ray is reflected or absorbed, whether reflection is diffuse or specular, and direction of reflection. Figure 4.4 is a flow chart that traces a ray from emission to absorption (Mahan, 2002).

The reader must be aware that even though the decisions are made by random numbers, the radiation distribution factors obtained are not random. The decisions ultimately made by random numbers are shaped by the parameters input as surface properties. For example, a surface with an emissivity (absorptivity) of 0.8 indicates that an incident ray has an 80% chance of being absorbed. If the random number R_α is 0.37792612, then the ray would be absorbed, but if the random number R_α were 0.99136781, the ray would be reflected. Even though a random number was used to make the decision, the outcome is dictated by the emissivity of the surface (Mahan, 2002).

Table 4.2 outlines the emissivity, specularity ratio, and emission of each component for the converter that was studied. The emitting components were all selected as emitting diffusely.

Once the model geometry has been imported, the boundary conditions are set, and the emitting surfaces have been determined, the simulation is ready to begin. An initial test with an emission of a low number of rays can be done to insure the model has been set up correctly. In Figure 4.5, the converter model in FELIX with 100 test rays emitted shows that most rays are emitted from the proper surfaces and are absorbed by other components within the structure with the few exceptions of rays emitted from surfaces lying in the same planes as the boundaries. Notice the blue surfaces are the "positive" surfaces, which were the ones considered by FELIX.

The ray trace included 5×10^6 emitted rays, and the simulation took 8 hr. and 52 min. to complete on a computer driven by an Intel Pentium II 400MHz processor. The model contained 29 total surfaces, and the radiation distribution factors were written to a results file with 841 numbers, which included 29 factors for each surface. The radiation distribution factors from non-emitters are zero, and many others are negligibly small. For this model, the highest 12 distribution factors were considered for each emitting surface.

From these numbers, the radiation heat transfer from each component could be easily calculated.

The last information needed to find the heat transferred from the components via radiation is the component temperatures. These temperatures came from the I-deas baseline simulation and are listed in Table 4.3.

Using the heat transfer definitions given earlier and the reciprocity rule for radiation distribution factors,

$$\varepsilon_i A_i D_{ij} = \varepsilon_j A_j D_{ji} \tag{4.12}$$

the heat transferred away from or to each component could be found. The total radiation heat transfer from surface *i* was found by using

$$Q_{net} = \varepsilon_i A_i \sigma (T_i^4 - \sum_{j=1}^{n} T_j^4 D'_{ij}) \tag{4.13}$$

For each component, the 12 highest radiation distribution factors were chosen out of the 37 possibilities to represent all of the receiving surfaces. These factors were substituted into equation 4.14 to calculate the heat flux from each of the receiving surfaces (surface j's) to the component of interest. The total emitted heat flux was also calculated, and the difference of these two values is the total heat flux from the component. This heat flux is multiplied by the component surface area to find the total heat transfer away from the component. One example of this spreadsheet calculation, the radiation heat transfer for the inductor, is given in Table 4.4. The radiation distribution factors and the rest of the component radiation heat transfer calculations are listed in Appendix E.

The sum of the 12 distribution factors in Table 4.4 is 0.981. Thus, only 1.9% of the total radiation emitted from the inductor was absorbed by the 19 surfaces not considered. The radiation heat transfer for every component is listed in Table 4.5. Radiation is only responsible for a small part of the heat generated by the component, so

the component heat generation and percentage of radiation heat transfer are also included in the table.

Four of the components in Table 4.5 transfer more than 10% of their heat generated by way of radiation. The rest emit an insignificantly small amount. All of the heat transfer values are positive, however, indicating that whether the amount of heat radiated is significant or not, there is a loss of energy due to radiation in every component. The negative heat transfer values would all be seen on surfaces such as the enclosure walls (assumed to be adiabatic in this project), fans, and other components dissipating little or no heat.

Once the radiation heat transfer from each component has been found, the next step would be to find the component temperatures resulting from this. This is difficult, however, because neither convection nor radiation dominates the heat transfer. Simply solving for a new component temperature by including the radiation heat transfer would not be correct because a new component temperature would affect the flow field and other components downstream. Because of this tight coupling between convection and radiation, the best approach is to use FELIX to help determine which radiation heat transfer rates are significant, as shown in table 4.5, and then to include the GBVFs of these components into I-deas for a net exchange analysis.

I-deas Radiation Analysis

Even though the net exchange method is not as accurate or as easy to use as the MCRT method, it is still a valuable tool because it is easier to implement in existing software. I-deas includes radiation analysis that allows a radiative thermal interface to be included between two surfaces. The emissivity of materials can be defined within the program, and the GBVF can be input as a parameter. The radiation conductance is described by

$$\text{Conductance} = \sigma \, \text{GBVF} \, \varepsilon \, A \, (T_{hot}^2+T_{cold}^2)(T_{hot}+T_{cold}) \qquad (4.4)$$

The only parameters needed are the GBVFs.

The GBVFs are simple to find using FELIX. The same analysis on the converter described in the first part of this chapter can be simulated with all surfaces assigned as blackbodies ($\varepsilon = 1$). This bypasses all reflections and specularity of surfaces and gives radiation distribution factors that are identical to the view factors. Since the radiation thermal coupling values must be input individually into I-deas, only the most significant values will be considered. Three components in particular will be the focus of the I-deas radiation analysis, the inductor and the DC/DC output capacitors. They were the two components with the highest percentage of heat dissipation due to radiation. The significant view factors for the three components, any factors with values greater than 0.05, are listed in Table 4.6. The other significant view factors are also included in Appendix E.

The surfaces involving radiation heat transfer as indicated by Table 4.6 were meshed in I-deas and simulated using the view factors as inputs for the radiation thermal couplings. The component temperature results could be compared to the baseline temperature predictions and the radiation effects could be studied.

The baseline temperature predictions for the inductor and surrounding components are shown in Figure 4.6. The temperatures in all four comparison figures correspond to the color bars on the right side of the page. The radiation emitted by the inductor was absorbed mostly by boundaries, such as the PCB, enclosure walls, or fans. Very little was absorbed by the nearby bulk capacitor, as seen in the lack of temperature change of the component. This indicates that even though the inductor had a significant amount of heat loss due to radiation, it did not significantly affect the surrounding components.

Radiation thermal couplings were input into I-deas using the values from Table 4.6 as parameters. The temperature results comparable to Figure 4.6 but with radiation effects included are shown in Figure 4.7. The same comparison can be made for the output capacitors in the front-end converter. The baseline case for the two capacitors and surrounding components is shown in Figure 4.8. The simulation of the DC/DC output capacitors with radiation effects included is shown in Figure 4.9. In this comparison, the capacitor temperatures decreased significantly and the diode temperatures increased

slightly. This shows the potential effects components have on each other due to radiation heat transfer. The component temperature rise comparisons are summarized in Table 4.7.

The two components determined to transfer a significant amount of heat to the surroundings by way of radiation both decreased in temperature. The enclosure walls, sides, and exit were assumed to have constant temperatures of 50°C, which is a conservative estimate, and the two critical components were near these surfaces. The majority of the heat transferred by radiation was transferred to these surfaces and not to the other components, causing little or no change on surrounding component temperatures.

Radiation heat transfer analysis on power electronics systems is difficult to perform. In this section, I have described the two methods for performing the analyses, the advantages and disadvantages of each, and the contribution of each one to predicting final component temperatures with both convection and radiation included in the analysis. As a result of the analysis of the front-end converter, we saw that three of the critical components, the inductor and the two DC/DC converter output capacitors, decreased in temperature while the temperature of surrounding components remained unchanged. Therefore, for the remainder of this project, radiation heat transfer was ignored on the basis that the temperatures predicted would be conservative and those components considered significant in the radiation analysis would have slightly over-predicted temperatures as a result of ignoring radiation.

4.2 Exit Vent Effects

Exit grills seem like trivial boundary conditions at a first glance, but it turns out that they cause flow effects that are extremely difficult to model computationally. Local blockage effects can impact component temperatures, especially for those components located immediately near the exit. The effects of exit grills are an important matter that should be considered and understood as well as possible in a thermal simulation.

The accuracy of modeling the effects of exit vents on the predicted flow field is not extremely well known. Several approaches have been attempted. In the majority of

the simulations performed in this project, no exit grill was used and the flow simply exited directly into ambient air. This is advantageous for temperature comparisons because the inaccuracy caused by modeling the vents is ignored, but it is not sufficient for accurate temperature predictions. Modeling complex exit vent designs can be difficult because of the high number and small size of exit hole openings. Once they are modeled, however, computational results still may not be reliable because of the difficulty of modeling effects produced by the flow field interactions with the complex vents. Another approach involves calculating the pressure drop across the vent and simulating a head loss coefficient in the computations. According to Lasance (2001), however, the accuracy of this method has not been explored thoroughly.

A simple computational study was performed and is discussed in this chapter. Comparisons between three different exit vent designs are discussed. The designs are listed in Table 4.8.

The flow field for the baseline case is shown on a flow plane 2cm above the base of the model in Figure 4.10. Velocity vectors are colored by velocity, not temperature, and a higher density of arrows indicates a greater density of grid points, not an increase in fluid density or volume flow rate. The maximum air velocity in the enclosure is 5.37m/s.

The second model studied shows more variation at the exit. A drawing of the exit vent is shown in Figure 4.11. The rectangular holes, each with a height of 3.2mm and width of 6mm, were modeled in I-deas. The design of the exit vent is a preliminary grill design for the converter studied in this project.

Figure 4.12 shows the flow field of that model on a flow plane 2cm above the base. The flow shows more realistic obstruction effects as it approaches the exit grill. It is more uneven, and it also includes a pressure drop that decreases the overall fan velocity. The maximum air velocity encountered in this model is 4.88m/s, a 9.1% decrease from the open model case.

The next set of models were simulated the same as the baseline model except with a loss coefficient assigned to the exit vent. The pressure drop resulting from this coefficient is described by

$$\Delta P = k_{loss} \frac{1}{2} \rho V^2 \tag{4.14}$$

A series of six models were considered, with loss coefficients ranging from 1.0 to 3.5 in increments of 0.5. Figure 4.13 shows the flow on a 2cm flow plane for the loss coefficient = 1.5 case. The flow characteristics change slightly for each case, but all are similar in appearance to the case shown in Figure 4.13. The volume flow rate through the enclosure for each value of loss coefficient is listed in Table 4.9.

An increase in loss coefficient slightly decreases the flow rate through the enclosure, but the changes in component temperatures were not significant enough to pursue further work in the present study.

Three cases were studied to investigate the sensitivity of component temperatures to exit grill modeling. Temperature results varied slightly, but overall very little change was observed in component temperatures. This justifies the use of an open exit vent model for the computations in this project.

Table 4.1. Net Exchange Assumptions

Assumption	Description
1	Isothermal surfaces: each individual surface is a constant temperature
2	Opaque surfaces: no radiation transmission through surfaces
3	Gray surfaces: spectral absorptivity and emissivity are independent of wavelength
4	Diffuse surfaces: radiation is emitted and reflected equally in all directions
5	Uniform surface radiosity: radiation emitted from and reflected by a surface leaves at a constant rate
6	Nonparticipating medium: the air neither absorbs nor scatters any of the radiation in the enclosure

Table 4.2. Component Surface Properties

Surface	Description	ε	r_s	Emitter?
1	Enclosure Base	0.80	0.80	
2	PCB	0.80	0.80	
3	Fans	0.98	0.00	
4	Heat Sinks	0.40	0.80	
5	Inductor	0.90	0.00	✓
6	PFC Output Capacitor	0.90	0.60	✓
7	Boost Diode 1	0.90	0.20	✓
8	Boost Diode 2	0.90	0.20	✓
9	Boost Diode 3	0.90	0.20	✓
10	PFC MOSFET 1	0.95	0.00	✓
11	PFC MOSFET 2	0.95	0.00	✓
12	PFC Diode Bridge	0.95	0.00	✓
13	EMI Plug	0.98	0.00	
14	EMI Capacitors	0.90	0.20	
15	EMI Inductors	0.90	0.00	✓
16	EMI Transformer	0.95	0.20	
17	DC/DC Input Capacitor	0.90	0.60	✓
18	Transformer Windings	0.90	0.00	✓
19	Transformer Magnets	0.90	0.40	
20	DC/DC MOSFET 1	0.90	0.00	✓
21	DC/DC MOSFET 2	0.90	0.00	✓
22	Secondary Diode 2	0.90	0.00	✓
23	Secondary Diode 1	0.90	0.00	✓
24	DC/DC Output Capacitors	0.90	0.60	✓
25	Enclosure Left Side	0.50	0.75	
26	Enclosure Right Side	0.50	0.75	
27	Enclosure Front	0.50	0.75	
28	Enclosure Exit	0.25	0.75	
31*	Enclosure Top	0.50	0.75	

*Surfaces 29 and 30 were null surfaces added accidently

Table 4.3. Predicted Component Temperatures

No.	Description	T(°C)	No.	Description	T(°C)
1	Enclosure base	50	16	EMI transformer	50
2	Printed circuit board	70	17	DC/DC input capacitor	69
3	Fans	50	18	Transformer windings	89
4	Heat sinks	92	19	Transformer magnets	89
5	Inductor	108	20	DC/DC MOSFET 1	99
6	PFC output capacitor	73	21	DC/DC MOSFET 2	100
7	Boost diode 1	69	22	Secondary diode 2	96
8	Boost diode 2	72	23	Secondary diode 1	98
9	Boost diode 3	71	24	DC/DC output capacitors	89
10	PFC MOSFET 1	83	25	Enclosure left side	50
11	PFC MOSFET 2	86	26	Enclosure right side	50
12	PFC diode bridge	98	27	Enclosure entrance	50
13	EMI plug	50	28	Enclosure exit	50
14	EMI capacitors	60	31	Enclosure top	50
15	EMI inductors	73			

Table 4.4. Radiation Heat Transfer from Inductor

Surface i	#	Surface j	#	D_{ij}	T_j(°C)	q''_a(W/m^2)
Inductor	5	Enclosure Base	1	0.0279	50	16
		PCB	2	0.1174	70	83
Tmax (°C):		Fans	3	0.1129	50	63
108		Heat Sinks	4	0.0355	92	32
		Inductor	5	0.1670	108	180
Area (mm^2):		PFC Output Cap	6	0.0942	73	69
5582		Boost Diode 1	7	0.0148	69	10
		Boost Diode 2	8	0.0109	72	8
Emissivity:		Boost Diode 3	9	0.0060	71	4
0.90		Enclosure Right Side	26	0.1317	50	73
		Enclosure Entrance	27	0.0518	50	29
q''_e (W/m^2):		Box Top	31	0.2104	50	117
1076				Total D_{ij}:		**q''_a (W/m^2):**
				0.981		**684**
					Q_{net}:	**2.188W**

Table 4.5. Radiation Heat Transfer from Components

Component	Power Dissipation (W)	Radiation Heat Transfer (W)	% Radiation
Inductor	8.0	2.2	28%
PFC Output Capacitor	2.0	0.1	5%
Boost Diode 1	1.5	0.0	0%
Boost Diode 2	7.0	0.0	0%
Boost Diode 3	1.5	0.0	0%
PFC MOSFET 1	5.0	0.1	2%
PFC MOSFET 2	5.0	0.1	2%
PFC Diode Bridge	14.5	0.3	2%
EMI Inductors	4.0	0.4	10%
DC/DC Input Capacitor	2.0	0.1	5%
Transformer Windings	15.0	1.9	13%
DC/DC MOSFET 1	10.0	0.2	2%
DC/DC MOSFET 2	10.0	0.2	2%
Secondary Diode 2	8.0	0.1	1%
Secondary Diode 1	8.0	0.1	1%
DC/DC Output Capacitors	3.0	0.7	23%

Table 4.6. View Factors Between Components

Emitting Surface	Receiving Surface	View Factor
Inductor	PCB	0.10
Inductor	Fans	0.08
Inductor	PFC Heat Sink	0.06
Inductor	PFC Output Capacitor	0.06
Inductor	Enclosure Right Side	0.21
Inductor	Enclosure Entrance	0.07
Inductor	Enclosure Top	0.35
DC/DC Output Caps	PCB	0.25
DC/DC Output Caps	Enclosure Left Side	0.18
DC/DC Output Caps	Enclosure Exit	0.12
DC/DC Output Caps	Enclosure Top	0.21

Table 4.7. Radiation Temperature Comparisons

Component	ΔT without Radiation (°C)	ΔT with Radiation (°C)	Change (°C)
Inductor Radiation			
Inductor	48.4	41.0	-7.4
PFC Output Capacitor	22.1	21.8	-0.3
Boost Diode 1	19.3	19.4	+0.1
Boost Diode 2	21.6	21.6	0.0
Boost Diode 3	21.3	21.3	0.0
DC/DC Output Capacitors Radiation			
DC/DC Output Cap 1	39.7	33.7	-6.0
DC/DC Output Cap 2	38.1	32.3	-5.8
Secondary Diode 1	50.0	51.6	+1.6
Secondary Diode 2	51.5	53.4	+1.9
Transformer Winding	88.9	88.9	0.0

Table 4.8. Exit Vent Designs

Case	Description
1	Open with no obstruction
2	Detailed model with many small openings
3	Open with loss coefficient of 1.5 based on approach velocity

Table 4.9. An increase in loss coefficient decreased the flow through the enclosure, causing a slight increase in temperature.

Loss Coefficient	Volume Flow Rate (m^3/s)	Mass Flow Rate (kg/s)	Maximum Velocity (m/s)	Average Velocity (m/s)
0.0	0.00856	0.00934	6.42	2.45
1.0	0.00848	0.00895	6.36	2.42
1.5	0.00843	0.00920	6.33	2.41
2.0	0.00839	0.00915	6.30	2.40
2.5	0.00834	0.00911	6.26	2.39
3.0	0.00830	0.00906	6.23	2.37
3.5	0.00825	0.00900	6.19	2.36

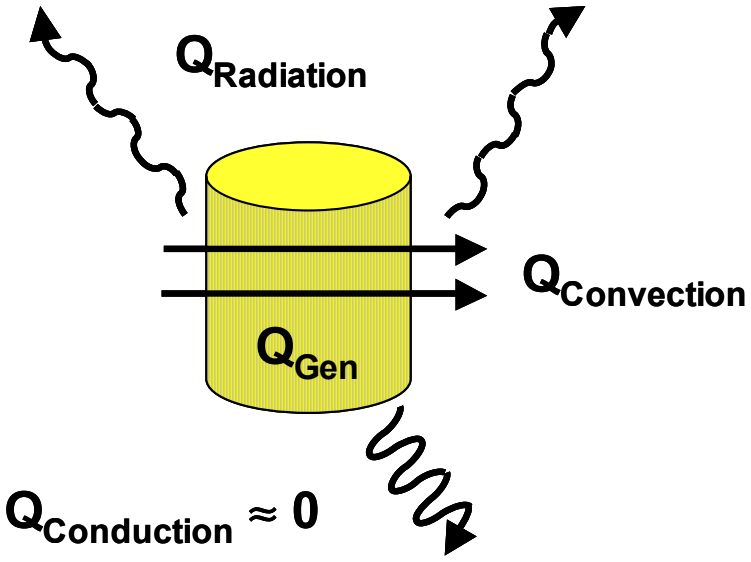

Figure 4.1. The heat transferred from a component must either heat the component or be carried away by one of three modes of transfer.

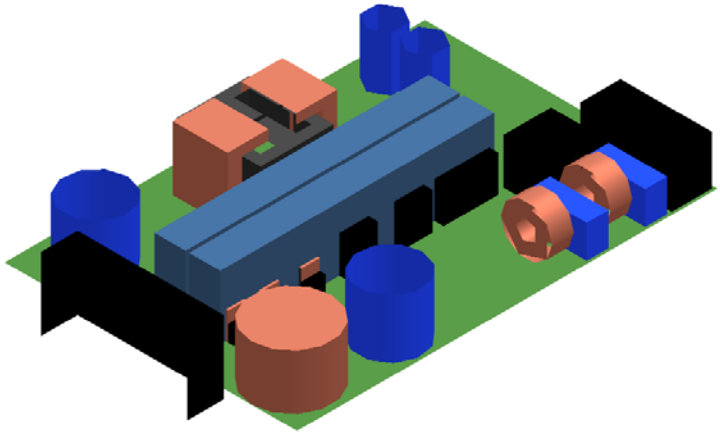

Figure 4.2. A drawing of the front-end converter was drawn in AutoCAD and exported into FELIX for the ray trace analysis.

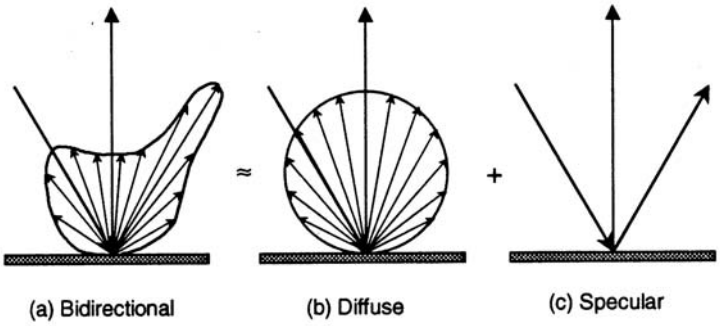

Figure 4.3. Nearly all reflections have a specular and a diffuse component (Mahan, 2002).

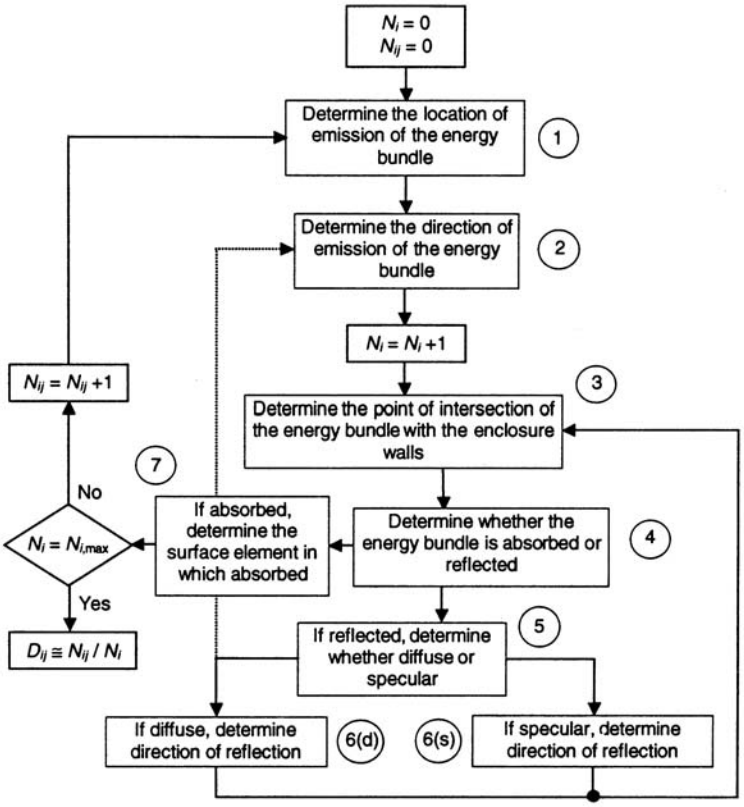

Figure 4.4. Each energy bundle emitted follows a path determined by several decisions made by random numbers (Mahan, 2002).

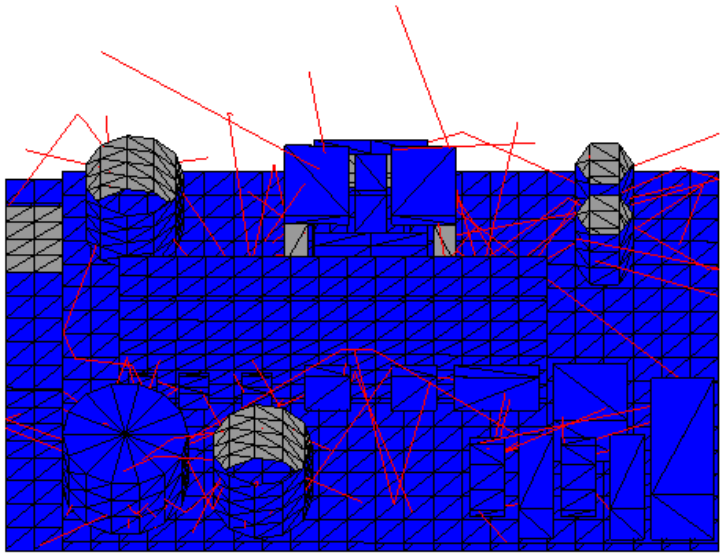

Figure 4.5. The rays emitted appear to be tracing correctly, indicating that the detailed simulation is ready to run.

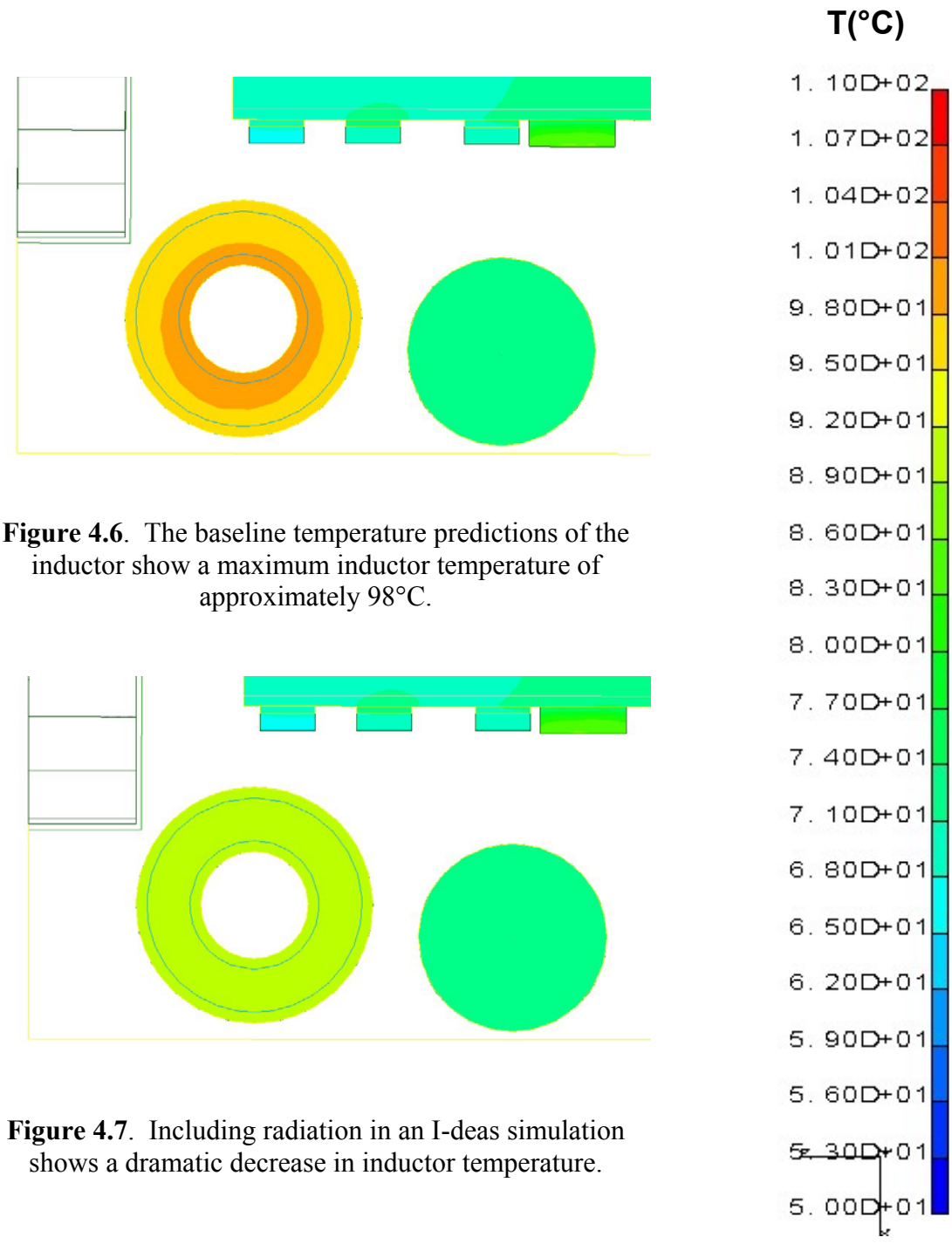

Figure 4.6. The baseline temperature predictions of the inductor show a maximum inductor temperature of approximately 98°C.

Figure 4.7. Including radiation in an I-deas simulation shows a dramatic decrease in inductor temperature.

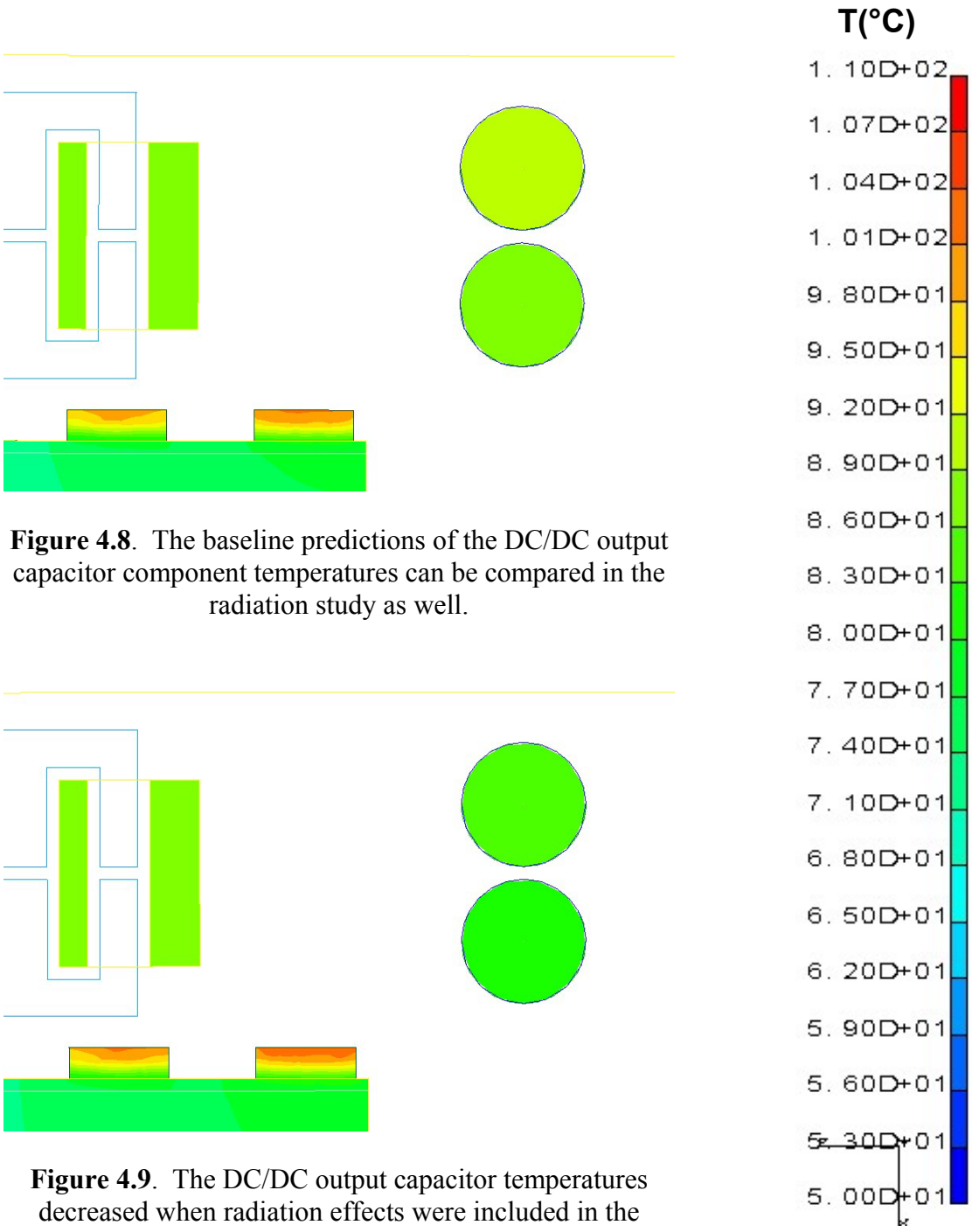

Figure 4.8. The baseline predictions of the DC/DC output capacitor component temperatures can be compared in the radiation study as well.

Figure 4.9. The DC/DC output capacitor temperatures decreased when radiation effects were included in the simulation.

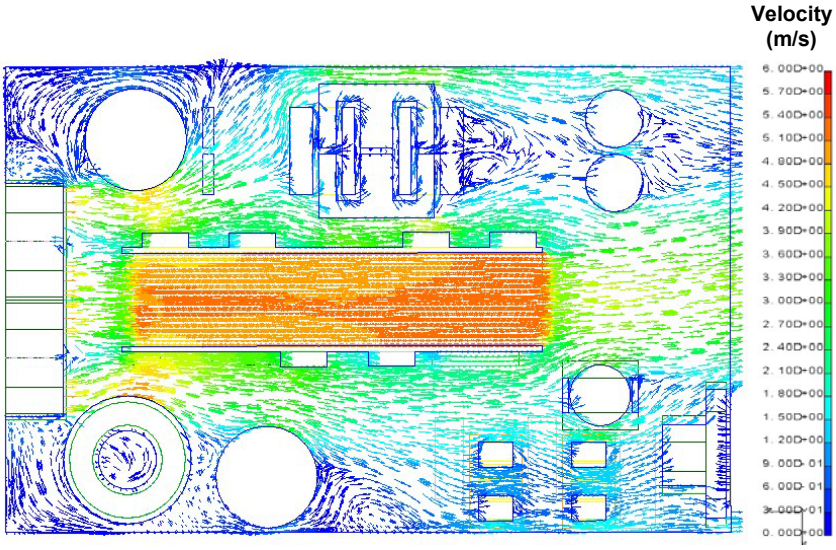

Figure 4.10. Flow field vectors for the baseline case show no obstructions at the converter exit.

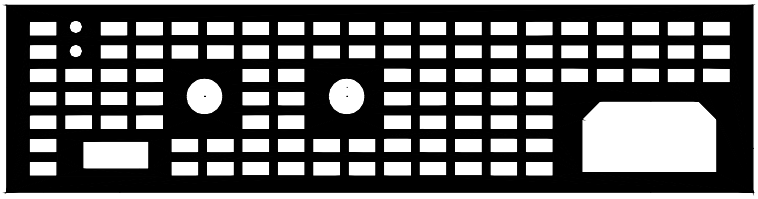

Figure 4.11. A more complicated exit vent was modeled in I-deas with the hope of finding a more accurate airflow model.

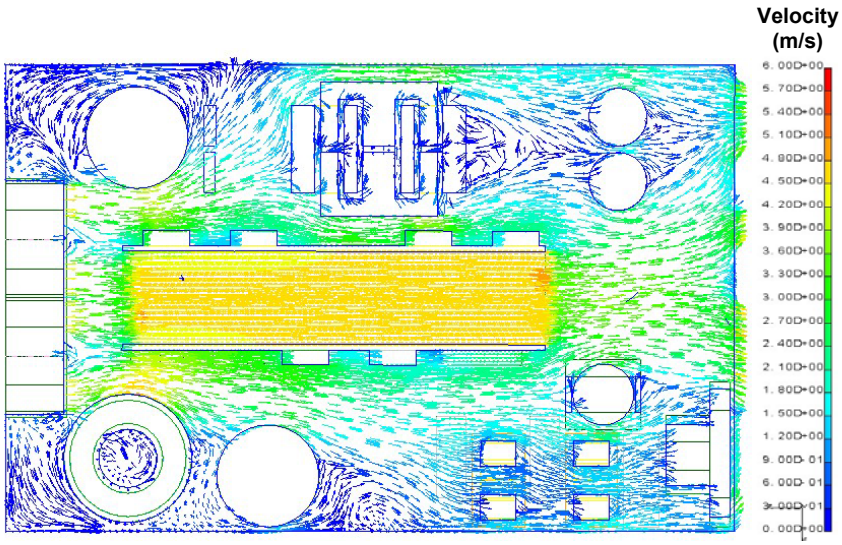

Figure 4.12. The detailed vent model shows jets forming at the exit and was found to have a maximum flow velocity of 4.88m/s.

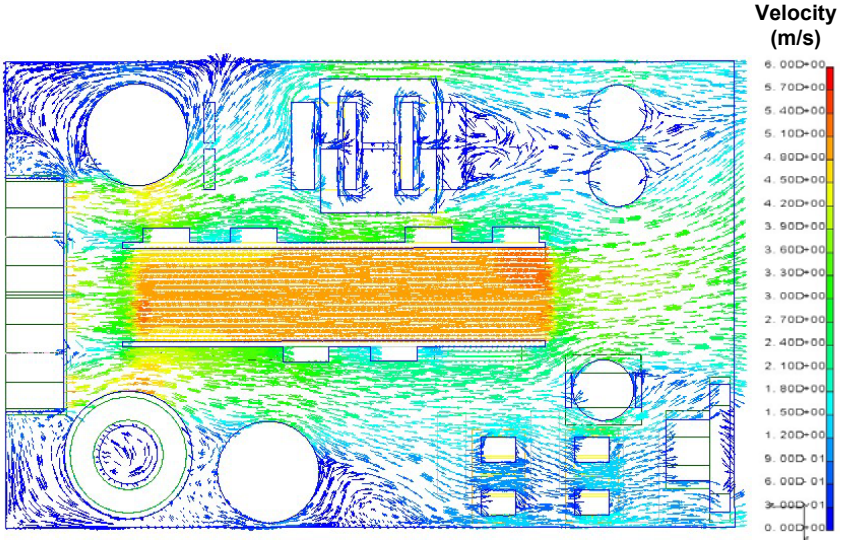

Figure 4.13. The air velocity with a loss coefficient of 1.5 shows results similar in appearance to the baseline model.

Chapter 5 –Component Rearrangement

The most valuable capability of thermal design and simulation software in use today is the analysis of numerous design possibilities with a minimal investment of time and resources. Upon completion of the thermal simulation of the DC/DC converter, a parametric study was performed in which the components were rearranged in seven different configurations and the results were analyzed to determine the effects component placement had on predicted component temperatures. Though power electronics simulations today are still on their way to being able to predict exact component operating temperatures, comparing simulations with each other gives a good indication of the trade-offs between component placement strategies. This chapter describes the results of the parametric study of component placement performed on the DC/DC converter with the goal of deriving a final layout that would operate with the best possible thermal performance while staying within the constraints for proper electrical operation.

This chapter begins with a description of the converter built for Eltek, which was used as the subject of this study. The baseline simulation results are presented, including component temperatures, thermal, and flow fields. The parametric variations of the layout were compiled in a test matrix. Section 5.3 describes the various layouts in the test matrix and the motivation for simulating each case. Section 5.4 is a presentation of the simulation and comparison of the component temperature results. Finally, the chapter concludes with a description of the final component layout suggested for optimum thermal performance.

5.1 Converter Description

The converter designed for Eltek by CPES is a front-end power converter used for telecommunications applications. The rack mounted power supply is designed for use with other telecommunications equipment in a configuration like the one pictured in Figure 5.1. The 1.2kW converter takes an AC input in the range of 150 – 264V and converts it to a DC output of 48V. A front-end power supply such as this one is designed and built to be robust and reliable, often operating in high temperatures. The components have high power losses and will overheat if they are not properly cooled.

The converter is divided into two halves, one built to rectify the signal from AC to DC and the other to step the DC voltage down to a lower potential. The two schematics are shown in Figures 5.2 and 5.3.

The purpose of the PFC filter is to convert the incoming AC signal to a DC voltage and to filter any noise inherent in power transmission. Power flow proceeds from left to right in the schematics shown in Figures 5.2 and 5.3. The diode bridge converts the incoming AC signal into a positive AC signal. Power then passes through the boost inductor and power MOSFETs, which serve as a switching power converter used to step the voltage up to $400V_{DC}$. The boost inductor, an energy storage device, generates a large amount of heat due to eddy currents formed in the magnets and conduction through the coils. Semiconductor switching also dissipates a large amount of power. Modern converters are designed to achieve higher efficiencies by minimizing losses even though the losses that occur are inevitable during operation of even the best converters.

The DC/DC buck converter is a switching converter that switches in such a way that only a small portion of the high DC input voltage drops across the load. Using switching to step down DC power has advantages over a voltage divider because the power is conserved instead of dissipated. A switching DC/DC converter is also designed to produce a constant output with minimal ripple effects.

An I-deas drawing of the system is shown in Figure 5.4. The numbered components in Table 5.1 correspond to the components in the layout, which is shown in Figure 5.5.

The three-dimensional model drawn in I-deas would serve as the geometric model for which the finite element model is constructed. The boundary conditions are assigned as heat loads applied to individual components.

The heat dissipated by each component is given in Figure 5.6. Table 5.2 lists the power dissipations (same as in Figure 5.6), but it also includes the heat generation of each component and the component's temperature limit as provided by the manufacturer. The high-voltage AC signal causes tremendous losses as is passes through the bridge diode, which dissipates power by switching and by a constant voltage drop during operation. The MOSFETs on the PFC filter side also switch at a high frequency, though their losses are not as high as the rectifier's losses because the heat generated is due mostly to switching instead of conduction resistance, which is smaller in a MOSFET than in a magnetic component. Magnetic components have several types of losses that can be extremely difficult to quantify because both core losses and copper winding losses contribute to the heat generation. On the DC/DC converter side, MOSFET and diode switching contribute to the losses. The transformer used to step down voltages has tremendous core and winding losses.

The components with the greatest heat loads are the magnetic components and the semiconductors. The MOSFETs and diodes, however, are mounted to the heat sinks and are not as difficult to manage as the inductor and transformer. The transformer dissipates 15W of power, while the inductor dissipates 8W at steady state operation. Each of these components is free standing and relies on the surrounding flow field to cool it. Careful attention must be paid to these components during the analysis.

5.2 Baseline Predictions

The baseline case was simulated in I-deas. The Panasonic fan curve introduced in figure 2.5 was used to determine the volume flow rate, and the enclosure exits were modeled as openings with 50% of the area blocked around the edges, as shown earlier in Figure 2.6. The walls were considered adiabatic, and perfect thermal couplings were assumed between the heat sinks and the components mounted to them. Radiation was

neglected in these studies. The mixing length turbulence model with a no-slip boundary condition was used in all of the computations.

The temperature predictions are shown in Figure 5.7. The temperature scale ranges from 50°C (inlet temperature) to 110°C, with the maximum temperature observed on the transformer and one of the secondary diodes. This maximum temperature is in the range of 98°C to 101°C, which is only slightly below the maximum allowable temperature.

One should note that the layout in this diagram differs slightly from other layout pictures. This study was done before the EMI filter was added, the PFC capacitor was switched with the boost inductor, and the DC/DC output capacitors were rotated 90°. These changes have minimal effects on the temperatures, however, because the EMI filter dissipates a small amount of power and the other components cause only slight changes in the flow patterns.

Figure 5.8 gives the predicted baseline temperature rises above an inlet temperature of 50°C. For example, the inductor temperature rise was predicted to be 46.8°C, which corresponds to an absolute surface temperature of 96.8°C. From these results, it is clear that the components with the highest temperatures are the transformer, secondary diodes, and inductor. The transformer is closer than the other three components to its permissible temperature limit stated earlier, even though it did not have the highest volumetric heat generation. This undesirable temperature rise is indicative of the flow rate passing by the transformer.

Figure 5.9 shows a top view of the flow field around the transformer. I-deas predicted the flow field for the entire converter, and those velocity vectors through the enclosure are shown in Figure 5.10. In the figure, the density of arrows represents the cell density and the velocity magnitude is indicated by the vector color. The flow field predictions show an increase in air velocity in the heat sink channel. A lack of resistance in flow past the heat sink fins causes more air to flow through it than around the outside where the free standing components act as blockage. Some of the vortices and recirculating areas can also be observed in the flow field predictions.

The thermal field can be predicted by I-deas and can be seen in Figure 5.11.

The highest air temperature can be seen exiting the heat sink channel. This serves as a measure of the ability of the heat sinks to transfer heat to the air flowing through the channel. The coolest areas show the lack of high-power components. Knowledge of the thermal fields can be helpful in finding ways to place components for optimized thermal operation.

5.3 Test Matrix Design

A parametric study was performed to determine a component layout in which all components would operate with temperatures significantly lower than their allowable limits. The initial layout configurations ignored the electrical constraints and focused only on thermal performance. Based on this assumption, a number of alternative layouts were devised to achieve a component arrangement that would result in cooler component temperatures. The electrical design would be considered after the layout design with the best thermal performance was achieved. Seven alternative cases were devised and these cases were simulated in I-deas. The predicted component temperatures for these cases were then analyzed to determine how changes in placement affected component temperatures. Some of the results obtained were unintuitive and will be discussed in Section 5.4. The knowledge gained from the I-deas simulations and guidelines for optimum electrical operation were then combined to come up with a single circuit layout suggestion for improved thermal performance that fit within the electrical constraints.

Table 5.4 lists the eight cases studied including the baseline case. A circuit layout is pictured, along with a description of the layout. The components are numbered according to the descriptions in Table 5.3.

The first layout considered, Case 1, was set up with the high-power components placed as near as possible to the fans. The idea was to make the air impinge on the components and cool them most, allowing the warmer air to continue on and cool the low-power components.

Case 2 was designed to force more air through the sides instead of directly down the heat sink channel. By placing the majority of the fan area to the side of the heat sinks

instead of directly in front of them, most of the air would be forced past the larger components, with only a small amount moving through the heat sinks cooling the semiconductors.

Case 3 was created simply by moving the fans to the other side of the enclosure. The flow direction remained the same, and the fans were set to suck air out of the box instead of blowing into it. This setup would create an area of low pressure inside the box, causing outside air at a higher pressure to be drawn into the entrance opening.

The fourth layout, Case 4, was formed by reversing the layout. Everything except for the system fans was rotated, and the flow direction remained the same. The fans still blew air across the components, as in the majority of other cases, but air was moved from the original exit towards the original inlet.

Cases 5 and 6 were very similar to each other. The heat sinks were spread apart, and the transformer was placed between them. The other components were simply shifted over to the open side, where they created a field of staggered cylinders. One concern was that the air would not pass over the heat sink fins (Case 5). Therefore, a blockage was placed behind the transformer in Case 6 to force the air between the heat sinks.

Case 7, the final variation, was derived by eliminating one of the heat sinks. All of the semiconductor components were mounted on a single heat sink to create an open passage on the other side.

With eight different simulations and thirteen component temperatures to compare for each simulation, a method was devised for comparing the layout designs. First, by studying the temperature contours, a maximum temperature for each component was found. The ambient temperature of 50°C was subtracted from this temperature to find the temperature rise. The temperature increase above ambient could then be compared for each layout.

One method of comparing the component temperatures to their temperature limits was by comparing that component's temperature rise above ambient to the temperature rise of the component's temperature limit, T_{limit}, above ambient. A factor defined as a % margin was defined to help quantify this comparison:

$$\%\ \text{margin} = \frac{T_{limit} - T_{comp}}{T_{limit} - T_{air}} \cdot 100\% \tag{5.1}$$

If the value of the % margin were found to be positive, the component would be within its desired temperature limit. If it were negative, however, the component would be over its temperature limit. A higher percentage gave a good indication that a component was well within its temperature limit, but a component shown to have a small % margin was approaching its temperature limit and should be carefully studied.

Another measure defined to compare the layout designs was a factor called % enhancement. It is defined as

$$\%\ \text{enhancement} = \frac{T_{Baseline} - T_{comp}}{T_{Baseline} - T_{air}} \cdot 100\% \tag{5.2}$$

This formula provided a quantitative comparison between a component's temperature and the same component's temperature from the baseline simulation. This was an improvement factor intended to tell how a component's placement compared to the baseline prediction. A positive value would indicate an improvement and also a decrease in a component's temperature relative to the baseline.

5.4 Test Matrix Results

Table 5.5 lists the temperature rise above the ambient of each component for each test matrix case. The highlighted numbers are the lowest simulated temperatures for each component out of all of the cases. Though some of the cases produced lower component temperatures than others, it is difficult to determine which case, if any, produced the best results.

Another way to approach these results is to find the % margin for the component temperature in each case, a comparison between the component temperature and the temperature's limit. Table 5.6 shows the % margin for each component temperature in

the test matrix. The highlighted areas indicate areas where the % margin is below 30%. All of the values are positive, indicating that all components were predicted to operate below their temperature limits, but the components with a % margin of less than 30% were considered to be the critical components, operating close to the temperature limits. The majority of these critical values are either describing the operation of the transformer or secondary diodes. Other than in Case 8, however, the secondary diodes operate farther below the temperature limit than the transformer does. Therefore, the transformer was established as the critical component. Therefore, closer consideration should be taken of it for the remainder of the study.

Table 5.7 lists the % enhancement for the component simulations. Highlighted numbers indicated a negative value of % enhancement, or a lack of improvement over the baseline. The high number of highlighted regions in Table 5.7 indicates that the baseline layout performed well thermally compared to the alternative cases. The transformer temperature, however, was predicted as operating dangerously close to its operating temperature limit. The trade-offs must be considered at this point.

Figure 5.12 shows a comparison of the % margin of the three components having the highest volumetric heat generation, including the transformer, one of the secondary diodes, and the inductor. The secondary diode and inductor stayed well below their temperature limit for the majority of the cases, but Cases 5 and 6 were the only two in which the transformer performed well, thermally. Recall that those two cases, nearly the same as each other, were the ones in which the transformer was placed between the heat sinks and directly in front of the fans. Case 1 also showed positive results. The idea of moving the transformer directly in front of the fans was used in all three cases. There was enough room for the air to pass by the transformer in Cases 5 and 6, and the configuration provided an ideal environment for the transformer.

The transformer is only one component in the converter, however. Looking at the other components in Cases 5 and 6, not all components show the same improvement. Figure 5.13 is a graph of the % enhancement for the thirteen components in the converter for the two cases. This situation shows a necessity for considering the trade-offs. The transformer and DC/DC capacitors were the only components in these layouts that showed significant improvement over the other components, but the transformer was also

shown to be the most critical component in these simulations, making these layouts worth considering. The components predicted to be at the highest temperature were the components on the outside of the heat sinks. A greater portion of the air was directed on to the transformer and through the heat sink channel, allowing very little flow through the PFC filter side. The changes made to produce this layout were accepted as improvements, however, and a final layout suggestion considering electrical design was based off of these layouts.

Another way of approaching these results was to focus on each component individually, deducing reasons for why it behaved the way it did. This gave many insights into flow field effects that could not be seen simply by staring at lists of temperatures. For example, the transformer temperatures were compared to each other for each case. Table 5.8 lists the case number, the temperature change from the baseline temperature as described by equation 5.3, and the reason for the change in temperature.

The results for each component were analyzed in this way, and the results found were helpful in determining a few general conclusions regarding the flow field through the converter. Constricted flow paths were shown to increase air velocity around components, increasing local heat transfer coefficients and decreasing component temperatures. This was demonstrated by Case 1, in which the heat sink was shifted towards the inductor, constricting the channel formed between the heat sink and enclosure wall and decreasing the inductor operating temperature. Other cases in which the inductor was in a wider channel, such as Cases 2 and 7, resulted in higher inductor temperatures. A comparison of the baseline case and Case 2 showed the importance of fan placement. Simply by shifting the fans over a small distance, the components mounted to the heat sink increased in operating temperature while free-standing components resulted in lower operating temperatures. Another trend deals with the placement of semiconductors mounted upstream and downstream of others on the same heat sink. Air traveling through a heat sink passage increases in temperature, becoming less effective in dissipating heat from the downstream components.

Another important result observed in the test matrix studies was the effect of individual component placement on the entire flow field. The difference between Case 5 and Case 6 shows the impact of blocking the downstream path of air. First, the air was

contained to the heat sinks, cooling the semiconductors well, but the constriction forced more air into the other side of the enclosure, cooling the free-standing components. Though the DC/DC input capacitor temperature remained the same for both cases, the temperature of the other four free-standing components, the PFC capacitor, inductor, and the two DC/DC output capacitors, was decreased in Case 6. The addition of the blockage was decided against in the final design because of the possibility of blocking all of the flow to any components in that region, but a variation of this type of design could definitely be considered. The exercise of studying each component and the impact of the surrounding flow field on the components was beneficial in understanding the complex cooling effects occurring throughout the converter.

At the beginning of the chapter, I mentioned that electrical considerations would not be considered until later. Some of the layouts defined for the test matrix are feasible from an electrical standpoint because of the components being required to remain in close proximity to each other. The test matrix results were invaluable for understanding how the flow field affected the component temperatures, however. Once a final design is being considered, however, the electromagnetic and electrical constraints must also be considered. For the electrical design, there are three criteria that must be met. Those three are shown in Figure 5.14. The three constraints are the following: the PFC output capacitor must be in close proximity to the boost diodes and PFC MOSFET, the DC/DC input capacitor must be connected to the DC/DC MOSFETs, and the DC/DC output capacitors must be connected to each other and located near the enclosure exit.

Based on the test matrix results and the electrical constraints governing the design, a new layout was suggested. It is very similar to the ones described in Cases 5 and 6. The transformer is located between the heat sinks and in front of the fans so it will encounter as much flow as possible. The DC/DC heat sink is mounted near the enclosure side wall, allowing a small channel for air across the semiconductor packages but relying on flow through the channel to cool the components mounted to it. The inductor and output bulk capacitor on the PFC side are in the middle of an open passage, where the open channel allows a smaller pressure drop and higher flow rate. The transformer is mounted behind the capacitor because the capacitor is aerodynamic and will not obstruct the flow field as much as the larger cross-section of the transformer. The DC/DC output

capacitors are staggered slightly, and the components in the PFC filter experienced very few changes. Though Case 6 showed a greater improvement in component temperatures, the wall behind the transformer was left off because such a design might completely cut off the flow of air over board mounted microelectronics, causing failure of low-power components. The final layout suggestion is shown in Figure 5.15.

In addition to an improved layout, a number of general guidelines for power electronics systems designers are defined for thermal consideration of future electronics designs. The first of these is to contain the air to within the heat sink. In areas where extruded fins are used as a heat sink, preventing air from escaping by positioning the sink near a wall or obstruction will help to keep components cool. Another recommendation is to place high-power free-standing components near the fans without blocking them. An adequate supply of air is the most effective coolant of those large components. In addition, free-standing objects near the fans might be in danger of overheating if placed too near the fans and off to the sides, as in the case of the bulk capacitors in the baseline design of this chapter. Finally, the wake behind large free-standing components is a good position to place other large components because of the increased velocity due to a jet effect from passing by the upstream component as well as the lower air temperature as opposed to the higher air temperature immediately behind the large upstream components.

This exercise has shown the capability of I-deas to bypass extensive testing to come up with an improved thermal design. Several cases were observed, and a final design could be based off of what was learned from the simulations. Once the baseline case was simulated, a test matrix was devised which consisted of a way to vary the layout in a methodical manner for the purpose of studying the predicted temperature results from the changes. Using the layout that produced the most favorable results as a beginning point, lessons learned from other simulations were implemented to produce a final layout suggestion.

Table 5.1. Converter Components by Number

Number	Description	Number	Description
1	Diode Bridge	10	DC/DC MOSFET 1
2	PFC MOSFET 2	11	DC/DC MOSFET 2
3	PFC MOSFET 2	12	Transformer
4	PFC Output Capacitor	13	Secondary Diode 1
5	Boost Inductor	14	Secondary Diode 2
6	Boost Diode 1	15	DC/DC Output Capacitor 1
7	Boost Diode 2	16	DC/DC Output Capacitor 2
8	Boost Diode 3	17	EMI Filter
9	DC/DC Input Capacitor		

Table 5.2. Component Temperature and Power Characteristics

No.	Component Name	Power Diss. (W)	Heat Gen. (W/in^3)	Temp. Limit (°C)
1	Diode Bridge	14.5	99.0	125
2	PFC MOSFET 1	5	50.50	125
3	PFC MOSFET 2	5	50.50	125
4	PFC Output Cap	2	0.97	105
5	Boost Inductor	8	5.43	150
6	Boost Diode 1	1.5	15.15	150
7	Boost Diode 2	7	70.7	150
8	Boost Diode 3	1.5	15.15	150
9	DC/DC Input Cap	2	0.97	105
10	MOSFET 1	10	101	125
11	MOSFET 2	10	101	125
12	Transformer	15	4.07	110
13	Secondary Diode 1	8	500	125
14	Secondary Diode 2	8	500	125
15	DC/DC Out Cap 1	1.5	0.99	105
16	DC/DC Out Cap 2	1.5	0.99	105
	Total	**100.5**		

Table 5.3. Component Descriptions by Number

Number	Description
1	Diode Bridge
2	PFC MOSFET
3	PFC Output Capacitor
4	Boost Inductor
5	Boost Diode
6	DC/DC Input Capacitor
7	DC/DC MOSFET 1
8	DC/DC MOSFET 2
9	Transformer
10	Secondary Diode 1
11	Secondary Diode 2
12	DC/DC Output Capacitor 1
13	DC/DC Output Capacitor 2

Table 5.4. Test Matrix of the Layout Variations Studied

Case	Layout	Description
Baseline	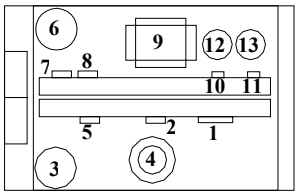	Baseline Case; Components arranged as provided by circuit designers
1	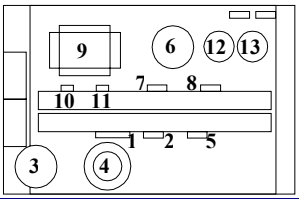	High-power components placed near fans
2	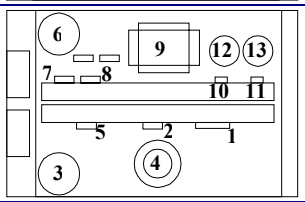	Fans spread apart to direct more air to free-standing components
3	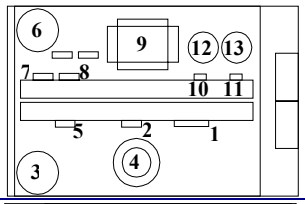	Fans moved to pull air through from left to right
4	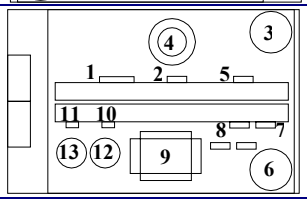	Layout rotated 180°
5	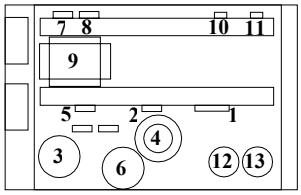	Transformer placed between heat sinks
6	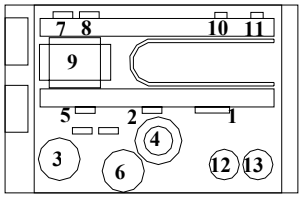	Same as case 6 but flow divider behind transformer and between heat sinks
7	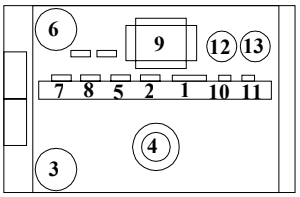	Eliminate one heat sink

Table 5.5. Test Matrix Temperature Rises

Component	Limit (°C)	Case							
		Base (°C)	1 (°C)	2 (°C)	3 (°C)	4 (°C)	5 (°C)	6 (°C)	7 (°C)
Diode Bridge	75.0	35.9	**30.1**	41.3	41.6	33.2	34.9	34.2	62.3
PFC MOSFET	75.0	32.6	34.1	37.4	37.8	36.1	31.4	**31.3**	53.9
PFC Output Cap	55.0	19.4	**14.8**	22.9	19.3	21.0	22.4	21.4	16.1
Boost Inductor	80.0	46.8	**41.3**	50.5	51.6	49.6	53.2	43.0	44.0
Boost Diode	75.0	27.0	33.5	31.3	32.0	37.4	**26.1**	26.8	49.0
DC/DC Input Cap	55.0	21.2	22.7	25.0	19.7	25.9	**15.1**	17.5	18.3
DC/DC MOSFET 1	75.0	**33.4**	36.9	37.4	38.1	46.1	34.7	33.5	39.9
DC/DC MOSFET 2	75.0	**33.4**	36.2	37.4	38.2	44.6	35.1	33.5	44.2
Transformer	60.0	49.6	44.8	52.6	54.3	53.4	40.3	**37.6**	51.1
Secondary Diode 1	75.0	47.8	**37.6**	53.0	54.0	43.2	53.5	47.0	68.1
Secondary Diode 2	75.0	52.5	**38.8**	56.8	58.7	44.9	59.1	51.2	69.4
DC/DC Output Cap 1	55.0	33.2	**24.1**	35.4	38.2	28.1	30.3	27.4	41.4
DC/DC Output Cap 2	55.0	33.0	**24.2**	35.3	37.3	25.3	32.1	28.3	40.1

Table 5.6. % Margin for Test Matrix Components

$$\%\ \text{margin} = \frac{T_{limit} - T_{comp}}{T_{limit} - T_{air}} \cdot 100\% \qquad (5.1)$$

Component	Case							
	1 (BL)	2	3	4	5	6	7	8
Diode Bridge	52%	60%	45%	45%	56%	53%	54%	**17%**
PFC MOSFET	57%	55%	50%	50%	52%	58%	58%	**28%**
PFC Output Cap	65%	73%	58%	65%	62%	59%	61%	71%
Boost Inductor	42%	48%	37%	36%	38%	34%	46%	45%
Boost Diode	64%	55%	58%	57%	50%	65%	64%	35%
DC/DC Input Cap	61%	59%	55%	64%	53%	73%	68%	67%
DC/DC MOSFET 1	55%	51%	50%	49%	39%	54%	55%	47%
DC/DC MOSFET 2	55%	52%	50%	49%	41%	53%	55%	41%
Transformer	**17%**	**25%**	**12%**	**10%**	**11%**	33%	37%	**15%**
Secondary Diode 1	36%	50%	**29%**	**28%**	42%	**29%**	37%	**9%**
Secondary Diode 2	30%	48%	**24%**	**22%**	40%	**21%**	32%	**7%**
DC/DC Output Cap 1	40%	56%	36%	31%	49%	45%	50%	**25%**
DC/DC Output Cap 2	40%	56%	36%	32%	54%	42%	49%	**27%**

Table 5.7. % Enhancement for the Test Matrix Results

$$\%\,\text{enhancement} = \frac{T_{Baseline} - T_{comp}}{T_{Baseline} - T_{air}} \cdot 100\% \tag{5.2}$$

Component	Case							
	Base	1	2	3	4	5	6	7
Diode Bridge		16%	**-15%**	**-16%**	8%	3%	5%	**-74%**
PFC MOSFET		**-5%**	**-15%**	**-16%**	**-11%**	4%	4%	**-65%**
PFC Output Cap		24%	**-18%**	1%	**-8%**	**-15%**	**-10%**	17%
Boost Inductor		12%	**-8%**	**-10%**	**-6%**	**-14%**	8%	6%
Boost Diode		**-24%**	**-16%**	**-19%**	**-39%**	3%	1%	**-81%**
DC/DC Input Cap		**-7%**	**-18%**	7%	**-22%**	29%	17%	14%
DC/DC MOSFET 1		**-10%**	**-12%**	**-14%**	**-38%**	**-4%**	0%	**-19%**
DC/DC MOSFET 2		**-8%**	**-12%**	**-14%**	**-34%**	**-5%**	0%	**-32%**
Transformer		10%	**-6%**	**-9%**	**-8%**	19%	24%	**-3%**
Secondary Diode 1		21%	**-11%**	**-13%**	10%	**-12%**	2%	**-42%**
Secondary Diode 2		26%	**-8%**	**-12%**	14%	**-13%**	2%	**-32%**
DC/DC Output Cap 1		27%	**-7%**	**-15%**	15%	9%	17%	**-25%**
DC/DC Output Cap 2		27%	**-7%**	**-13%**	23%	3%	14%	**-22%**

Table 5.8. Transformer Temperature Change Explanations

$$\Delta T = (T_{transformer\_case\#} - T_{air}) - (T_{transformer\_Baseline} - T_{air}) \tag{5.3}$$

Case	ΔT	Reason
1	-4.8	Transformer moved closer to fans
2	+3.0	Possible higher pressure drop across components
3	+4.7	Fans sucking air produce much lower mass flow rate
4	+3.8	Transformer in wake of output capacitors
5	-9.3	More air impinging on transformer
6	-12.0	Higher air velocity past transformer sides
7	+1.5	Decreased pressure drop on other side of enclosure

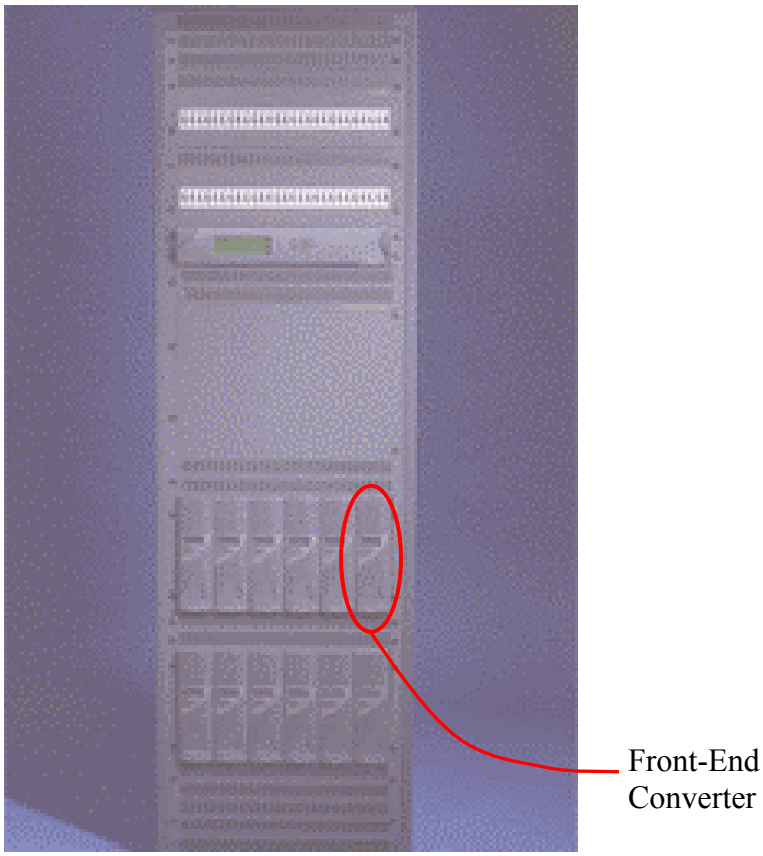

Figure 5.1. The front-end converter uses a high-voltage AC input to supply power to the rest of the system.

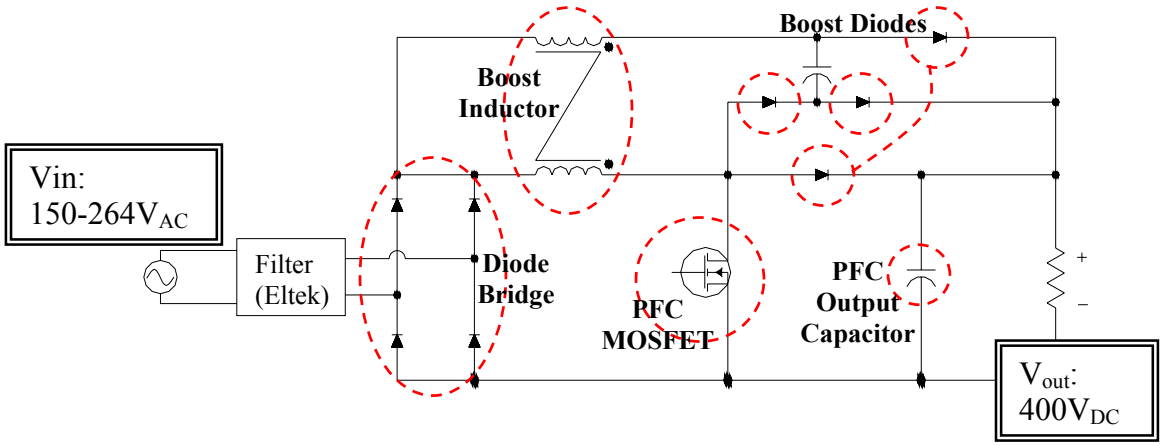

Figure 5.2. The PFC filter converts the input signal from AC to DC.

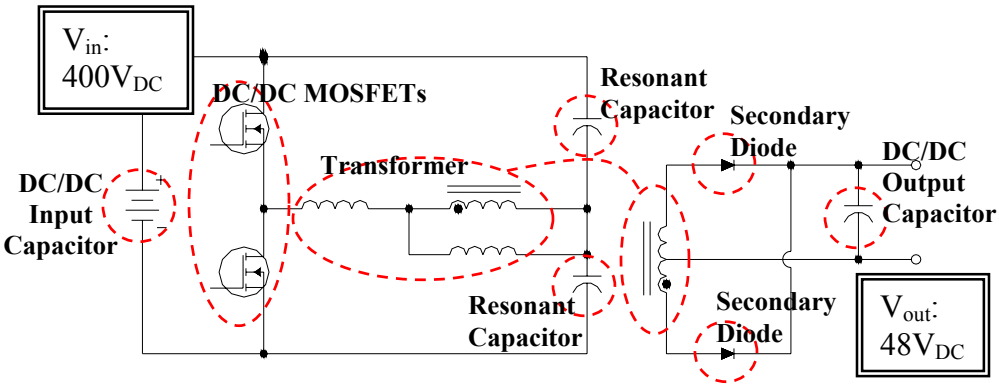

Figure 5.3. The DC/DC buck converter steps the input voltage down to a useful level.

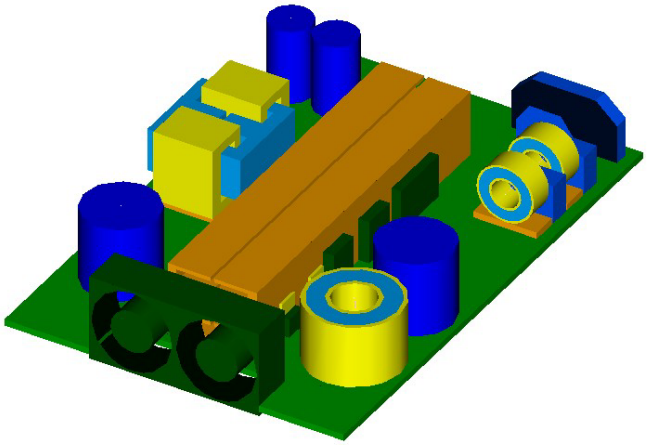

Figure 5.4. The Eltek DC/DC converter consists of two stages, an input PFC Filter stage, and an output DC/DC converter stage.

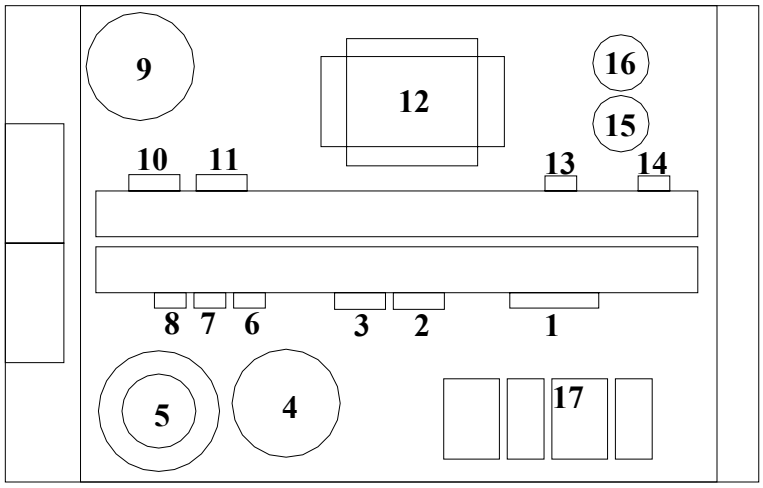

Figure 5.5. The discrete components performing the power conversion operations of the system are each assigned a specific power loss value.

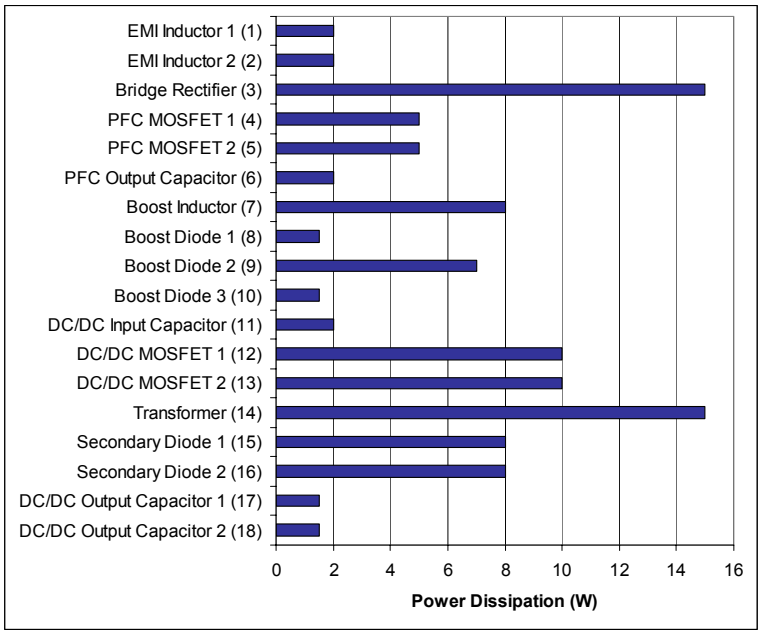

Figure 5.6. A heat load is assigned individually to each component in the converter.

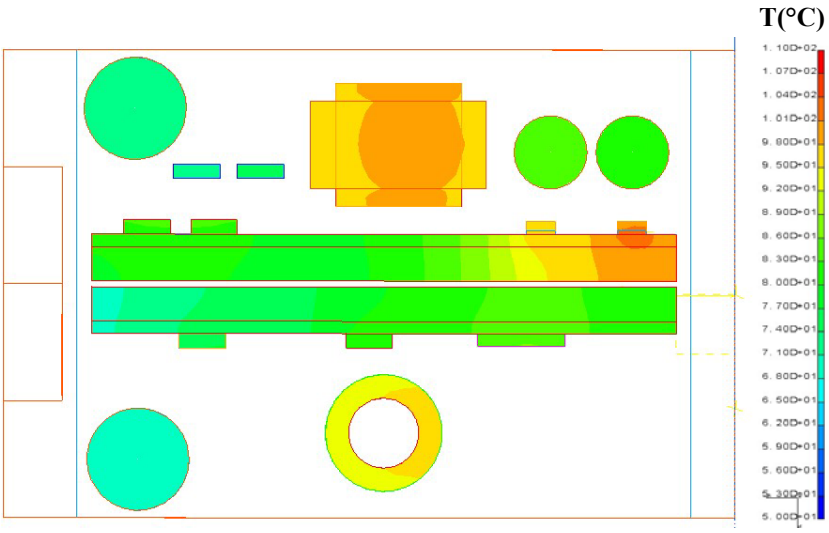

Figure 5.7. The temperatures from the baseline simulation range from a minimum of 70°C to a maximum of 103°C.

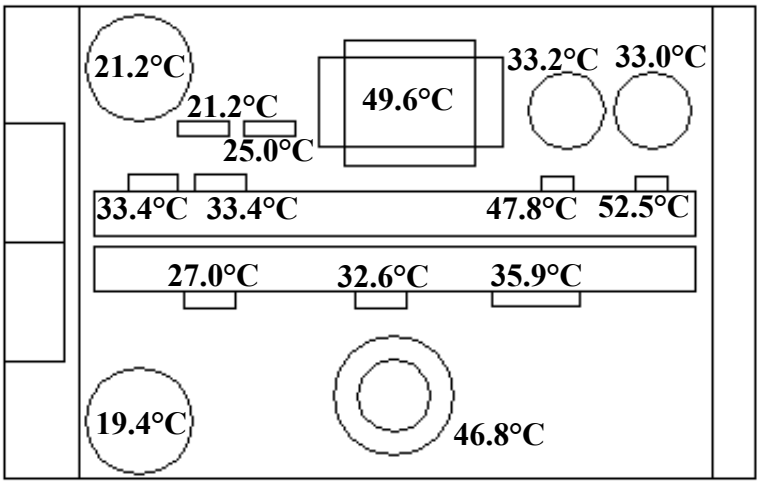

Figure 5.8. The baseline component temperature rises over a 50°C inlet temperature were predicted by I-deas.

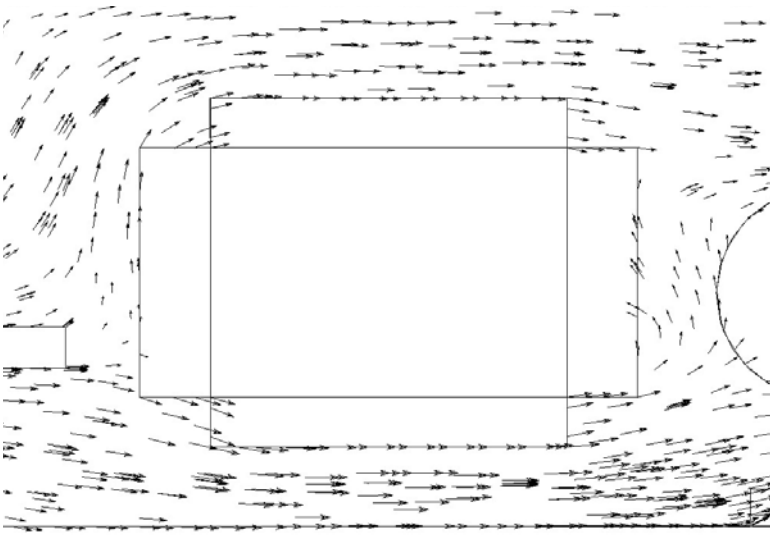

Figure 5.9. The air along the sides of the transformer was not adequate to cool it down to significantly below the operation temperature limit.

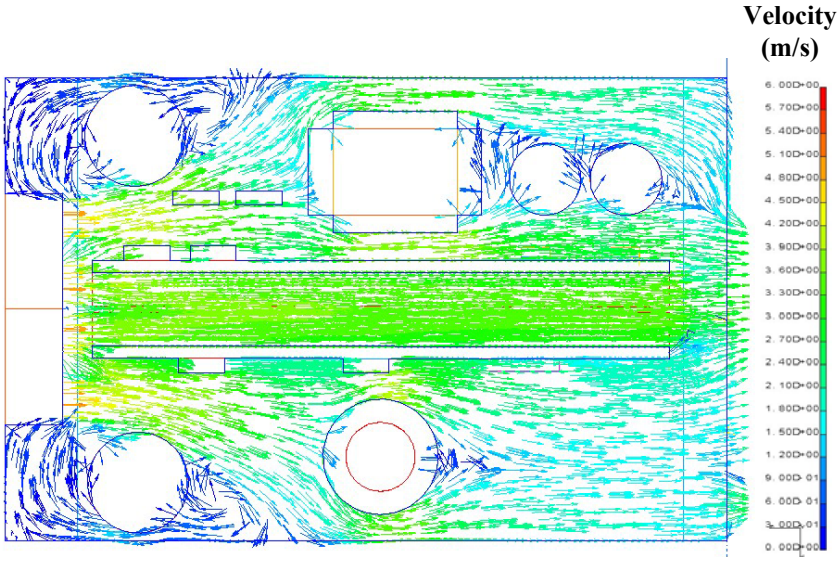

Figure 5.10. The flow field was predicted alongside component temperatures with I-deas CFD.

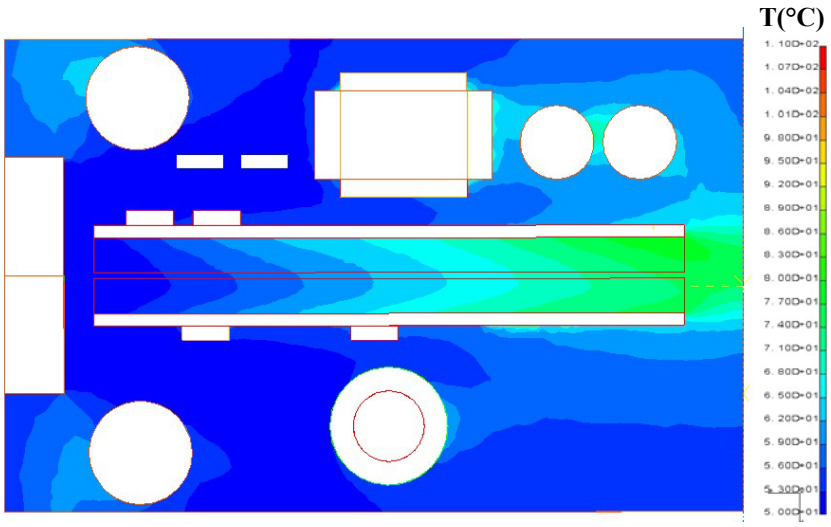

Figure 5.11. The air temperature predictions can also provide valuable insight into thermal performance.

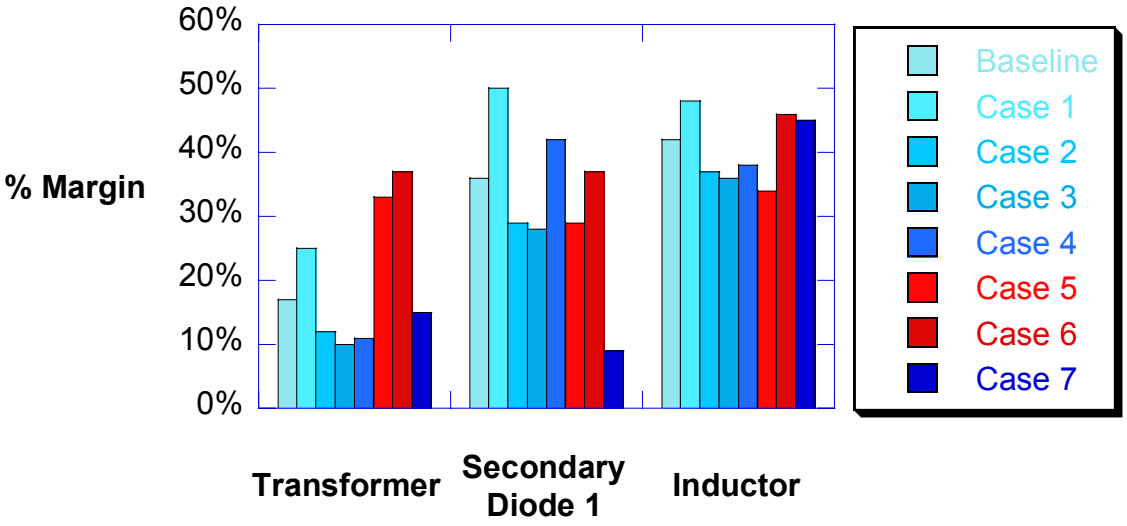

Figure 5.12. A comparison of the % margin of three of the critical components shows promising potential for Cases 5 and 6.

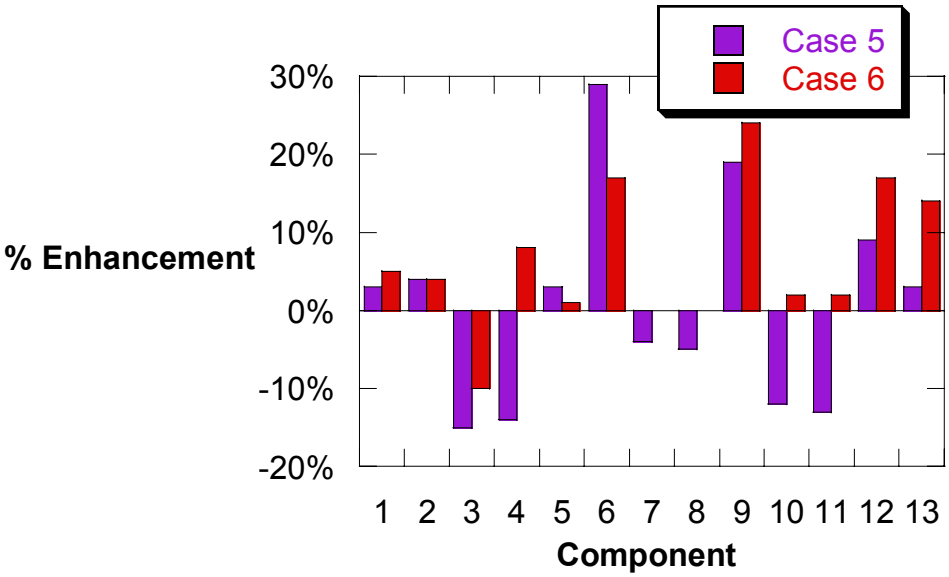

Figure 5.13. The % enhancement for Cases 5 and 6 shows that several components operated with lower temperatures in the improved cases.

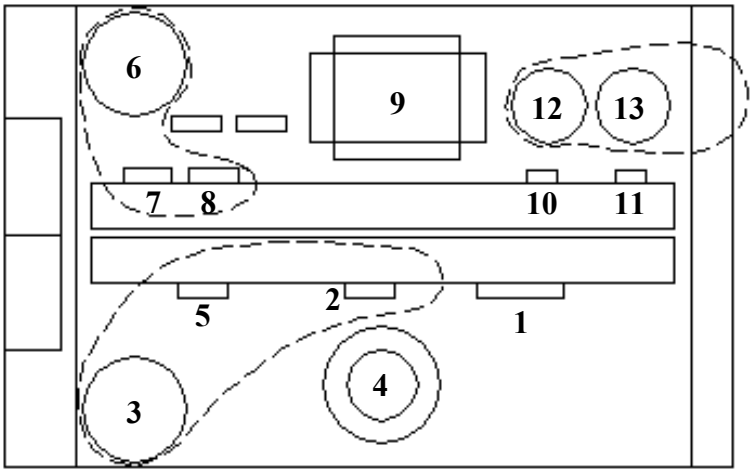

Figure 5.14. Three electrical constraints govern the overall layout of the converter.

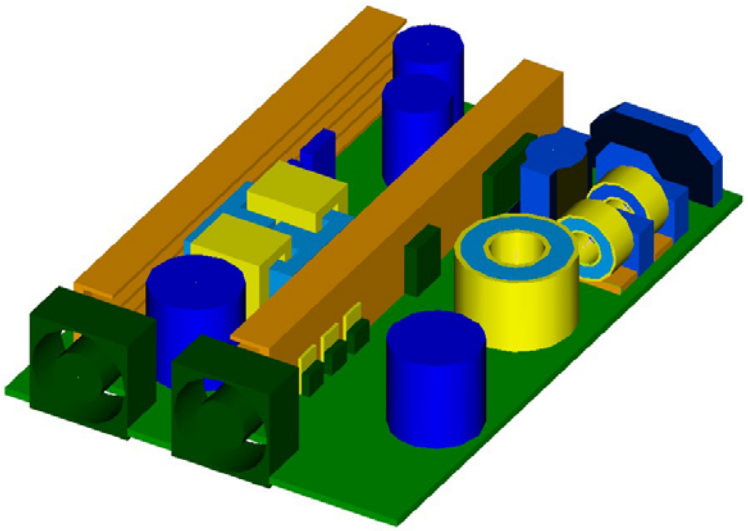

Figure 5.15. The suggested layout is a product of both electrical and thermal design.

Chapter 6 – Conclusions

Trends in power electronics toward a steady increase in power density are reaching a point where limitations arise out of thermal and electromagnetic design rather than in electrical innovation. New developments in IPEMs have taken steps towards modularization and standardization of power electronics and have introduced the necessity of system level thermal analysis. The goal of this project was to lay a foundation for this system level thermal analysis using a commercial software package called I-deas (I-deas, 2001). A front-end 1.2kW power converter was used as the subject of a number of studies including both computational parametric studies and experimental benchmarking. Results from experiments designed to quantify the temperature prediction ability of I-deas were helpful in understanding the strengths and weakness of the code. Future work should continue to explore the prediction capability of I-deas and prepare more benchmarking experiments to further verify predicted results.

The primary goal of this project was to establish the use of I-deas as a system level temperature prediction tool for power electronics systems designed by CPES. Secondary goals included the thermal prediction of component temperatures of the state-of-the-art front-end power converter designed for telecommunications and computing applications as well as creating a layout for improved thermal performance with a parametric study taking into account both electrical and thermal performance. Characterizing the temperature prediction capability of I-deas was a goal addressed by several experimental benchmarking studies designed for comparison of I-deas predictions with matching experiments. Finally, establishing a methodology for the use of radiation heat transfer analysis in power electronics was an objective stemming from a lack of ability to confidently include radiation in system level analysis because of the simplifying assumptions needed for traditional methods, which are also complicated and difficult to implement in a complex system.

The front-end power supply shown in Figure 6.1 was used as the subject of the experimental, computational, and parametric studies. The system consisted of a number

of heat-dissipating components, some free-standing and others mounted to a central channel formed by two heat sinks.

Two fans produced the cooling flow, which was the most significant factor in determining the steady-state component temperatures because convection was the primary heat transfer effect studied in this project. Assumptions were made on the system boundary conditions, including adiabatic enclosure walls, a fan curve describing the flow rate, and an open exit vent releasing air to atmospheric pressure and inlet temperature. This system was the baseline system for nearly most studies in the project.

I-deas was used to predict component temperatures. Figure 6.1 is the geometric model of the baseline system as modeled in I-deas. I-deas functions were used for finite element meshing as well as boundary condition definition, solution generation, and post processing.

An experiment comparing I-deas temperature predictions to measurements taken of two experimental test circuits, each representing half of the converter, produced inaccurate results. Though prediction trends compared well, exact prediction of temperatures was not obtained. A number of unknowns prevented a good comparison, encouraging the formation of more controlled experiments.

A comparison of I-deas predictions with lab experiments performed by Pang (2001) resulted in justification of modeling no thermal interface between the semiconductors and heat sinks. Modeling a resistive thermal coupling at the interface of mounted components produced slightly more accurate results, but the results were not enough of an improvement to necessitate adding the complexity of thermal couplings to the semiconductor modeling.

A third experiment involved using an atomizer to introduce flow into a system that could be visualized and photographed to verify the existence of flow field effects observed in the I-deas predictions. Comparisons showed the existence of vortices and flow field irregularities predicted by I-deas, though predicted velocity vectors did not exactly describe the flow seen in the experiments. For a system level tool, I-deas was accepted as capable of predicting a flow field accurately enough to predict bulk component temperatures. Predicting local heat transfer coefficients would not be accurate in most locations in the flow field.

Finally, a controlled experiment was set up using a known inlet flow rate introduced into a model of the converter including a DC heater capable of both producing a constant known heat flux on its walls and measuring its wall temperatures. Results in comparisons with I-deas were varied. Predictions of temperatures in some areas such as the front of the component and the downstream sides of the component were found to be the most accurate. The back side of the component was typically the least accurately predicted because of the inability of I-deas to accurately predict the trailing stagnant regions immediately behind the heater.

A thermal management methodology has been established for initial prediction of thermal performance, but comparisons with experiments have revealed that modeling accuracy still needs to be addressed. Once an initial simulation in I-deas has been obtained, a number of advanced options are available for improving accuracy. Two of the biggest areas not explored in this project include grid refinement and turbulence modeling. For the simulations in this project, free meshing was used to create a system mesh for the air volume, and this mesh was reduced in size uniformly until simulations could no longer be completed because of mesh size and computer limitations. The goal of refining the mesh was to decrease the size to the point where temperature predictions no longer depended on mesh size, but as mentioned in Chapter 1, accurate system level grid generation often requires an unrealistic number of cells. In order to continue increasing the accuracy resulting from proper grid sizing, local grid refinement and mapped meshing options in I-deas should be explored.

Another important area that should be carefully studied is in I-deas turbulent modeling. Though Reynolds numbers are somewhat low in most situations, the complex geometry often trips boundary layers and causes turbulent flow. Studies have shown turbulent simulation models to be more accurate than laminar models in electronics enclosures, and the turbulent flow predictions of I-deas should be thoroughly examined and tested.

A few of the studies in this project were done on single aspects of the system and then included into the system simulations, such as studying thermal interfaces on a small scale or focusing only on fan flow prediction. More small-scale studies should be performed outside of the system. For example, the thermal performance of the

transformer in the front-end converter is extremely complicated. Obtaining an approximate local velocity of surrounding air from the system level predictions and running simulations only on the transformer will allow grid size to be reduced and manipulated with ease and simulation times to be shorter while local effects are being studied. This would allow for more work to be accomplished on local aspects of the system without having to waste time keeping the model consistent with the rest of the system.

Though computational modeling of power electronics at the system level has not been perfected, the ability of CFD simulation and finite element modeling has made great strides in the ability to predict component temperatures. The experiments in this project have shown that computational temperature predictions are extremely helpful in identifying key components and comparing design alternatives. The predictions in a controlled experiment showed promise in the trends predicted. As Reynolds Number increased, prediction capabilities improved, and at the maximum flow rate nearly all temperatures predicted were measured to within ±5°C. The ability of I-deas to predict component temperatures at the system level is an important asset to power electronics engineers, and can save tremendous amounts of time and money on the front end of electronics system design.

Finally, system level modeling must keep up with current advances in power electronics. System integration involves integrating IPEMs into discrete systems, greatly increasing power density. Any experimental data obtained should be carefully questioned for accuracy and used for benchmarking simulations for thermal operations. The accuracy of system level modeling should be continually studied and improved. As power electronics continue to push the limits for higher power density levels, the thermal performance and characterization will become necessary for the success of all new electronics designs. As electronics design reaches closer to this point, thermal analysis must be capable of accurately handling any difficult situations introduced at the system level.

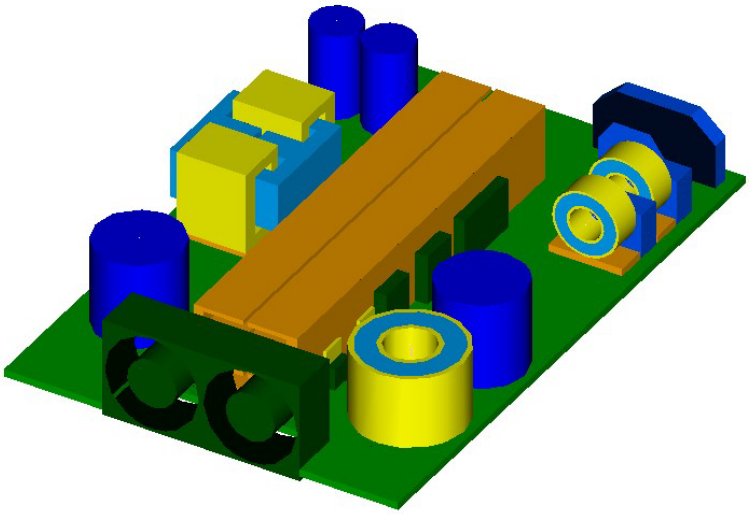

Figure 6.1. The front-end power supply was used as the basis for the thermal studies in this project.

References

Dong, W., (2002), CPES Research Assistant at Virginia Tech, personal correspondence.

Fernandez, X., Coimbra, A., Pinto, J., Antunes, C., Donsion, M., (1998) "Thermal Analysis of an Induction Motor Fed by Unbalanced Power Supply Using a Combined Finite Element – Symmetrical Components Formulation," IEEE Paper No. 0-7803-4754, pp. 620-624.

Flotherm, (1994), software by Flometrics.

Grimes, R., Davies, M., Punch, J., Dalton, T., Cole, R. (2001) "Modeling Electronic Cooling Axial Fan Flows," *Transactions of the ASME*, Vol. 123, pp. 112-119.

Gusev, V., Pustovalov, A., Borshchevsky, A., Chmielewski, A., (2000) "Experimental Confirmation of Milliwatt Power Source Concept," 18th International Conference on Thermoelectrics, pp. 500-504.

Humphrey, J., Devarakonda, R., Queipo, N., (1992) "Interactive Computational-Experimental Methodologies (ICEME) for Thermofluids Research: Application to the Optimized Packaging of Heated Electronic Components," ASME EEP., ASME, New York, vol. 1, pp. 179-191.

I-deas, (2001), Version 8, software by Electronic Data Systems.

Incropera, F., DeWitt, D., 1996, Fundamentals of Heat and Mass Transfer. New York: John Wiley & Sons.

Lall, B., (1998) "Concurrent Thermal Design for High-Power Electronics," Fourteenth IEEE SEMI-THERM Symposium, pp. 95-103.

Lasance, C., (2001) "The Conceivable Accuracy of Experimental and Numerical Thermal Analysis of Electronic Systems," Seventeenth IEEE SEMI-THERM Symposium, pp. 180-198.

Lee, T., (1994) "Application of a CFD Tool for System-Level Thermal Simulation," *IEEE Transactions on Components, Packaging, and Manufacturing Technology*, Part A, Vol. 17, No. 4, pp. 564-571.

Lee, F., Barbosa, P., (2001) "The State-of-the-Art Power Electronics Technologies and Future Trends," IEEE Paper No. 0-7803-7285-9, pp. 1188-1193.

Liang, F., Wolf, K., Thottuvelil, J., Alameel, G., (2002) "An Evaluation of Board-Mounted Power Module Packages," IEEE Paper No. 0-7803-7404-5, pp. 112-118.

Mahan, J., (2002), Radiation Heat Transfer: A Statistical Approach. New York: John Wiley & Sons.

Nevárez-Ayala, F. (2001), *Functional Enviroment for Longwave Infrared eXchange (FELIX)*.

Pang, Y., (2001) *Integrated Thermal Design and Optimization Study for Active Integrated Power Electronic Modules (IPEMs)*, M.S. Thesis, Virginia Tech.

Queipo, N., Humphrey, J., Ortega, A., (1998) "Multiobjective Optimal Placement of Convectively Cooled Electronic Components on Printed Wiring Boards," *IEEE Transactions on Components, Packaging, and Manufacturing Technology*, Part A, Vol. 21, No. 1, pp. 142-153.

Saber Designer, (2001), software by Avant!

Soule, C., (1994) “Yesterday’s cooling won’t work on tomorrow’s electronics,” *PCIM Magazine*, Nov., 1994, pp. 34-36.

VanWyk, J., (2002), Electrical Engineering professor at Virginia Tech, personal correspondence.

Yang, B., Lee, F., Cheng, R., (2001) “LLC Resonant Converter for Front End DC/DC Conversion,” 2001 Virginia Tech Center for Power Electronics Seminar, pp. 44-48.

Zhang, M., Jovanovic, M., Lee, F., (1997) “Design and Analysis of Thermal Management for High-Power-Density Converters in Sealed Enclosures,” IEEE Paper No. 0-7803-3704-2, pp. 405-412.

Zhao, Q., Tao, F., Zhang, J., Lee, F., (2001) “Single-Switch Parallel Power Factor Correction AC/DC Converters,” 2001 Virginia Tech Center for Power Electronics Seminar, pp. 238-244.

Appendix A – State-of-the-art in Electronics Cooling

Air Cooling References:

Ro, P., Loh, B., (2001) "Feasibility of Using Ultrasonic Flexural Waves as a Cooling Medium," IEEE Transactions on Industrial Electronics, Vol. 48, No. 1, pp. 143-150.

Zhang, H., Huang, X., (2001) "Heat Transfer Studies of a Porous Heat Sink Characterized by Straight Circular Ducts," International Journal of Heat and Mass Transfer 44, pp. 1593-1603.

Lundquistz, C., Carey, V., (2001) "Microprocessor-Based Adaptive Thermal Control for an Air-Cooled Computer CPU Module," 17th IEEE SEMI-THERM Symposium, pp. 168-173.

Klett, J., Klett, L., Burchell, T., Walls, C., (2000) "Graphitic Foam Thermal Management Materials for Electronics Packaging," ASME Paper No. 2000-01-1576.

Brignoni, L., Garimella, S., (2000) "Heat Transfer from a Finned Surface in Ducted Air Jet Suction and Impingement," Transactions of the ASME, Vol. 122, pp. 282-285.

Copeland, D., (2000) "Optimization of Parallel Plate Heatsinks for Forced Convection," 16th IEEE SEMI-THERM Symposium, pp. 266-272.

Chu, R., (1999) "A Review of IBM Sponsored Research and Developmenet Projects for Computer Cooling," 15th IEEE SEMI-THERM Symposium, pp. 151-165.

Vafai, K., Zhu, L., (1999) "Analysis of Two-Layered Micro-Channel Heat Sink Concept in Electronic Cooling," International Journal of Heat and Mass Transfer 42, pp. 2287-2297.

Zhang, K., Sorgo, M., (1998) "Design and Use of Heat Spreaders to Cool Low to Moderate Power Plastic Packages," 14th IEEE SEMI-THERM Symposium, pp. 57-62.

Black, W., Hartley, J., (1998) "Heat Transfer Modules for Cooling Electronics Packages," International Symposium on Advanced Packaging Materials, pp. 209-214.

Aranyosi, A., Bolle, L., Buyse, H., (1997) "Compact Air-Cooled Heat Sinks for Power Packages," IEEE Transactions on Components, Packaging, and Manufacturing Technology, Part A, Vol. 20, No. 4, pp. 442-451.

Stockholm, J., (1997) "Current state of Peltier cooling," 16th International Conference on Thermoelectrics, pp. 37-46.

Copeland, D., (1997) "High Performance Heatsinks for Processors and Power Electronics: Beyond Extrusions," IEEE Paper No. 0-7803-4303-4, pp. 146-149.

Copeland, D., Behnia, M., Nakayama, W., (1997) "Manifold Microchannel Heat Sinks: Isothermal Analysis," IEEE Transactions on Components, Packaging and Manufacturing Technology, Part A, Vol. 20, No. 2, pp. 96-102.

Flynn, E., Johnson, C., Lee, S., (1997) "Surface Mount Technology Heat Sinks for D^2PAK and D^3PAK Power Semiconductors," 13th IEEE SEMI-THERM Symposium, pp. 142-148.

Garner, S., (1996) "Heat Pipes for Electronics Cooling Applications," Electronics Cooling, September 1996, Article 2, pp. 1-10.

Kleiner, M., Keuhn, S., Haberger, K., (1995) "High Performance Air-Cooling Scheme Using Ducted Microchannel Parallel Plate-Fin Heat Sinks," 11th IEEE SEMI-THERM Symposium, pp. 122-130.

Liquid Cooling References:

McShane, C., (2002) "Vegetable-Oil-Based Dielectric Coolants," IEEE Industry Applications Magazine, May 2002, pp. 34-41.

Bhavnani, S., Fournelle, G., Jaeger, R., (2001) "Immersion-Cooled Heat Sinks for Electronics: Insight from High-Speed Photography," IEEE Transactions on Components and Packaging Technologies, Vol. 24, No. 2, pp. 166-176.

Gopinath, D., Joshi, Y., Azarm, S., (2001) "Multi-Objective Placement Optimization of Power Electronic Devices on Liquid Cooled Heat Sinks," 17th IEEE SEMI-THERM Symposium, pp. 117-119.

Baumann, H., Heinemeyer, P., Staiger, W., Topfer, M., Unger, K., Muller, D., (2001) "Optimized Cooling Systems for High-Power Semiconductor Devices," IEEE Transactions on Industrial Electronics, Vol. 48, No. 2, pp. 298-306.

Quadir, G., Leong, C., Krishnan, G., Seetharamu, K., (2000) "Performance of Wire-On-Tube Heat Exchangers Used in Immersion Cooling for Electronic Packages," Electronics Packaging Technology Conference, pp. 445-451.

Lee, T., (1998) “Design Optimization of an Integrated Liquid-Cooled IGBT Power Module Using CFD Technique,” InterSociety Conference on Thermal Phenomena, pp. 337-342.

Angirasa, D., Peterson, G., (1996) “Numerical Modeling of High-Performance Metallic Fibrous Heat Sinks for External Cooling,” IEEE InterSociety Conference on Thermal Phenomena, pp. 203-210.

Appendix B – Computer Solution Times

This appendix outlines the solution times of many of the computational simulations performed in this project. The number of elements in the numerical model is compared to the simulation time, and the results show somewhat linear behavior. The specifications of the computer system used are outlined at the top of the page.

SPECint is a benchmark to measure system efficiency during integer operations. It consists of twelve operations which are extremely computation-intensive and concentrate on the CPU and memory. Other components, such as disk I/O and network, are not measured by this benchmark. SPECfp2000 is a benchmark for measuring a system's ability to calculate floating point data, used to calculate very large numbers, or numbers that include fractions.

The computer running the simulations in this project was a Dell Precision 330, with a 1.7GHz Pentium 4 CPU and 512 Mbytes of memory. Its SPECint2000 rating is 591, and its SPECfp2000 rating is 607.

Current computing times range from two hours to eleven hours for full-sized models. This does not work well for users in industry planning on relying on numerical simulations for temperature predictions. The rate of increase in computing power, however, promises to bring these times down significantly. Computer manufacturers are speculating that computers will reach SPECint2000 ratings of over 4000 within a few years! With that kind of increase in processing power, simulations that take multiple hours on today's machines will become extremely practical for the work place. Therefore, just because these simulations take multiple hours does not mean I-DEAS does not belong in industry. With an increase in computational power, I-DEAS will become a quick, efficient design tool for thermal design of tomorrow's power electronics.

The objective of this worksheet is to compare simulation run times on a computer.

Computer Specs -- Dell Precision 330 running Windows 2000:

SPECint2000:	591 (574 base)
SPECfp2000:	607 (591 base)
CPU:	1.7 GHz Pentium 4
Memory:	512 Mbytes (PC800, Expandable to 2G)
Bus Speed:	400 MHz (32-bit, 3.2GBytes/sec)
Hard Disk:	36 Gbytes ultra 160/M SCSI (10,000rpm)

File	Air Elements	Solid Elements	Total Elements	Run Time
101	228883	112589	341472	4:18:00
102	253745	112589	366334	4:23:33
103	200522	112589	313111	3:35:54
104	232303	121361	353664	4:35:17
105	253328	147982	401310	6:06:41
107	225206	108472	333678	4:11:58
205	263203	127259	390462	7:40:59
207	263104	129380	392484	7:04:42
208	286709	135543	422252	7:28:57
209	301105	144741	445846	8:23:27
210	302445	147196	449641	9:10:54
212	350149	150309	500458	9:22:43
215	286162	156666	442828	7:49:56
216	286162	156666	442828	7:27:45
218	286285	160097	446382	7:01:49
219	286450	158316	444766	7:17:52
220	302445	147196	449641	9:12:42
220	302445	147196	449641	9:12:42
221	285774	159281	445055	7:24:57
222	302445	147196	449641	9:08:43
224	302445	147196	449641	8:55:15
225	302445	147196	449641	8:47:09
226	302445	147196	449641	9:04:52
227	302445	147196	449641	9:09:37
301	232303	121361	353664	3:37:43
302	232303	121361	353664	3:48:30
303	232303	121361	353664	4:10:35
304	192160	98191	290351	4:04:37
305	237690	122258	359948	4:13:37
307	179435	76844	256279	2:26:05
308	232303	121361	353664	4:04:43
309	232303	121361	353664	4:46:07
310	232303	121361	353664	5:09:17
311	232303	121361	353664	5:50:19
312	232303	121361	353664	5:07:29
313	232303	121361	353664	7:32:02

The following graph shows the computational times versus the number of elements included in the models.

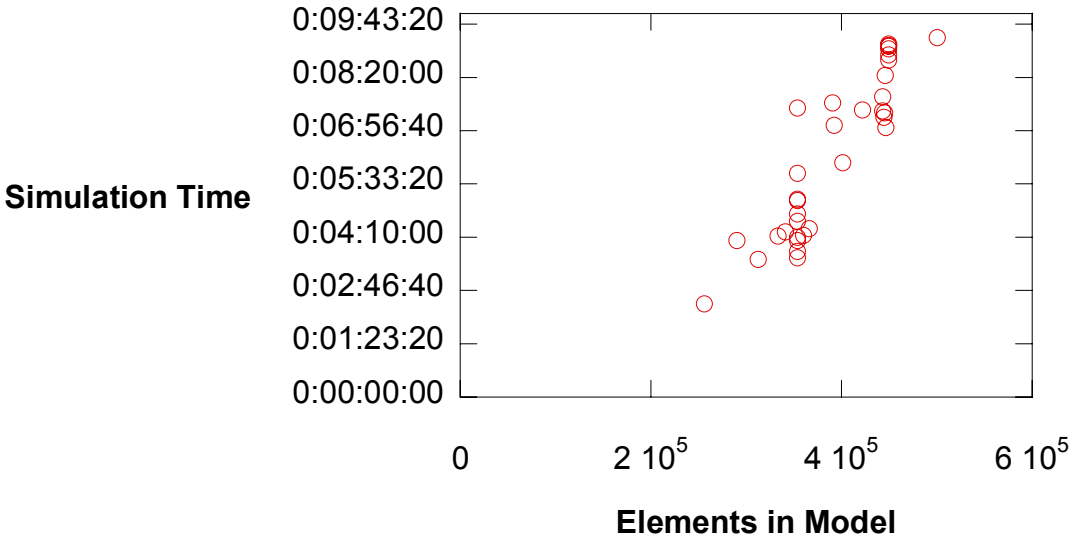

Appendix C -- Analytical Calculation of Pang's (2001) Model

This sheet was created to assist in verifying the I-DEAS simulations of Ying Feng Pang's model of two MOSFETs mounted to a single heat sink. It includes part and heat sink dimensions, MOSFET heat loads, and convection calculations based on air velocity. The goal was to calculate the juction temperature rise of the MOSFETs, but other temperatures, such as the package temperature or heat sink temperature, could be found.

Overall Inputs:

$T_{amb} := 24 \cdot C$

$P_{dissipated} := 4.308 \cdot W$

$Q := 0.05 \cdot \frac{m^3}{s}$

System Dimensions:

MOSFET:

$length_M := 16 \cdot mm$

$width_M := 2 \cdot mm$

$height_M := 21 \cdot mm$

Box Area:

$side := 150 \cdot mm$

$depth := 400 \cdot mm$

$cross\_sectional\_area := side^2$

$velocity := \frac{Q}{cross\_sectional\_area}$

Heat Sink:

$length_B := 78 \cdot mm$

$width_B := 40 \cdot mm$

$height_B := 7.5 \cdot mm$

$number_F := 10$

$thickness_F := 2 \cdot mm$

$spacing_F := 6 \cdot mm$

$height_F := 25 \cdot mm$

$$\text{perimeter}_F := \text{length}_B + 2\cdot\text{height}_B + 2\cdot\text{number}_F\cdot\text{height}_F + \text{number}_F\cdot\text{thickness}_F + \text{number}_F\cdot\text{spacing}_F$$

$$\text{flow\_area} := \text{perimeter}_F\cdot\text{width}_B$$

Flow Characteristics (at 300K, from Incropera DeWitt):

$$\upsilon := 1.589\cdot10^{-5}\cdot\frac{m^2}{s}$$

$$k := 0.0263\cdot\frac{W}{m\cdot C}$$

$$Pr := 0.707$$

$$Re_x := \frac{\text{velocity}\cdot x}{\upsilon}$$

Formulas and solutions (Heat Sink Convection):

$$Nu := 0.332\cdot Re^{\frac{1}{2}}\cdot Pr^{\frac{1}{3}}$$

$$\frac{h\cdot x}{k} := Nu$$

$$h\_avg := \frac{1}{\text{flow\_area}}\cdot\text{perimeter}_F\cdot\int_0^{0.04} 0.332\cdot k\cdot\left(\frac{\text{velocity}\cdot x\cdot m}{\upsilon}\right)^{\frac{1}{2}}\cdot Pr^{\frac{1}{3}}\cdot\left(\frac{1}{x\cdot m}\right)dx\cdot m$$

$$h\_avg = 29.089\circ\frac{W}{m^2\cdot C}$$

Formulas and solutions (MOSFET surface Convection):

$$\text{perimeter}_M := \text{length}_M + 2 \cdot \text{width}_M$$

$$\text{flow\_area}_M := \text{perimeter}_M \cdot \text{height}_M$$

$$Nu := 0.332 \cdot Re^{\frac{1}{2}} \cdot Pr^{\frac{1}{3}}$$

$$\frac{h \cdot x}{k} := Nu$$

$$\text{h\_avg}_M := \frac{1}{\text{flow\_area}_M} \cdot \text{perimeter}_M \cdot \int_0^{0.025} 0.332 \cdot k \cdot \left(\frac{\text{velocity} \cdot y \cdot m}{\upsilon} \right)^{\frac{1}{2}} \cdot Pr^{\frac{1}{3}} \cdot \left(\frac{1}{y \cdot m} \right) dy \cdot m$$

$$\text{h\_avg}_M = 43.804 \, \frac{W}{m^2 \cdot C}$$

Thermal Resistance Calculations:

Convection:

$$R_{Sink} := \frac{1}{h\_avg \cdot flow\_area}$$

$$R_{M} := \frac{1}{h\_avg_{M} \cdot flow\_area_{M}}$$

Other Thermal Resistance:

$$R_{CS} := 0.323 \cdot \frac{C}{W}$$

$$R_{JC} := 0.5 \cdot \frac{C}{W}$$

$$R_{JA} := 30 \cdot \frac{C}{W}$$

Total Thermal Resistance Through Top and Bottom of Chip:

$$R_{top} := R_{M} + R_{JA}$$

$$R_{bottom} := R_{JC} + R_{CS} + R_{Sink}$$

Parallel Resistance:

$$R_{eq} := \frac{R_{top} \cdot R_{bottom}}{R_{top} + R_{bottom}}$$

Results Summary:

$T_{amb} = 24\ C$

$P_{dissipated} = 4.308\ W$

$Q = 0.05\ \frac{m^3}{s}$

$R_{Sink} = 1.277\ \frac{C}{W}$ $R_{CS} = 0.323\ \frac{C}{W}$ $R_{top} = 84.355\ \frac{C}{W}$

$R_{M} = 54.355\ \frac{C}{W}$ $R_{JC} = 0.5\ \frac{C}{W}$ $R_{bottom} = 2.1\ \frac{C}{W}$

$R_{JA} = 30\ \frac{C}{W}$ $R_{eq} = 2.049\ \frac{C}{W}$

Junction Temperature Rise:

$T_{J\_Rise} := P_{dissipated} \cdot R_{eq}$

$T_{J\_Rise} = 8.827\ C$

Junction Temperature:

$T_{J} := T_{amb} + T_{J\_Rise}$

$T_{J} = 32.827\ C$

Heat Flow to Air Through Package:

$$H_{air} := \frac{T_J - T_{amb}}{R_M + R_{JA}}$$

$H_{air} = 0.105\ W$

Heat Flow to Air through Sink:

$$H_{sink} := \frac{T_J - T_{amb}}{R_{JC} + R_{CS} + R_{Sink}}$$

$H_{sink} = 4.203\ W$

Surface Temperature:

$$T_{surface} := T_J - H_{air} \cdot R_{JA}$$

$T_{surface} = 29.688\ C$

Case Temperature:

$$T_{case} := T_J - H_{sink} \cdot R_{JC}$$

$T_{case} = 30.725\ C$

Heat Sink Temperature:

$$T_{sink} := T_J - H_{sink} \cdot R_{Sink}$$

$T_{sink} = 27.459\ C$

Appendix D

Comparison of DC Heater Experiments and Computations

Q = 10cfm

Component Temperature Rises Given

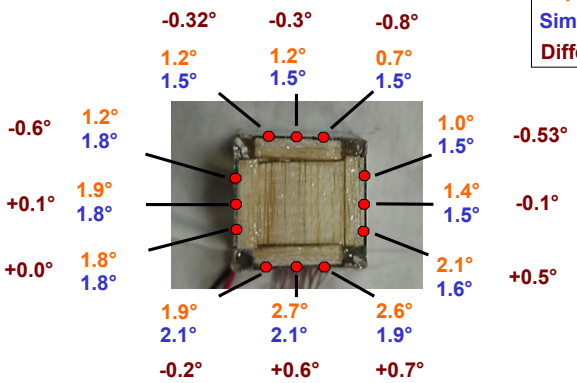

$P_{dissipated}$ = 0.311W

Q = 10cfm

Component Temperature Rises Given

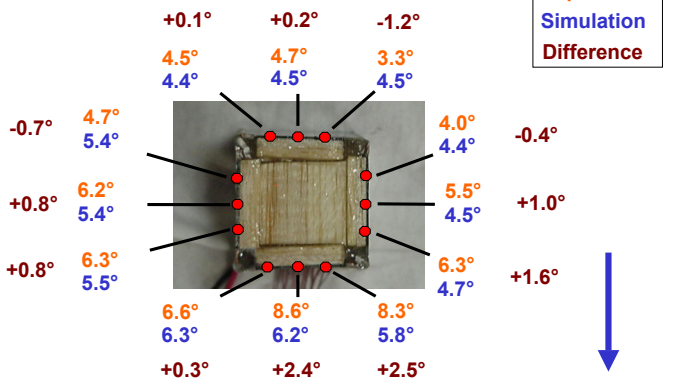

$P_{dissipated}$ = 0.941W

Q = 10cfm

Component Temperature Rises Given

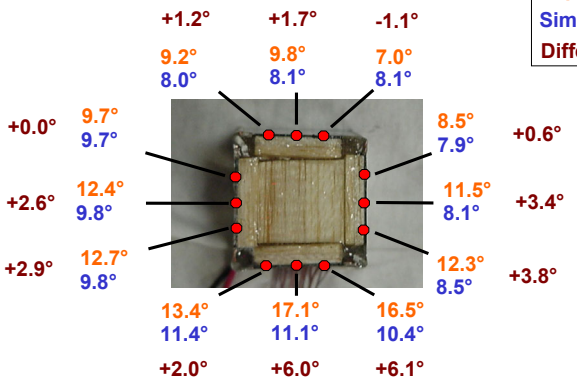

$P_{dissipated}$ = 1.692W

Q = 10cfm

Component Temperature Rises Given

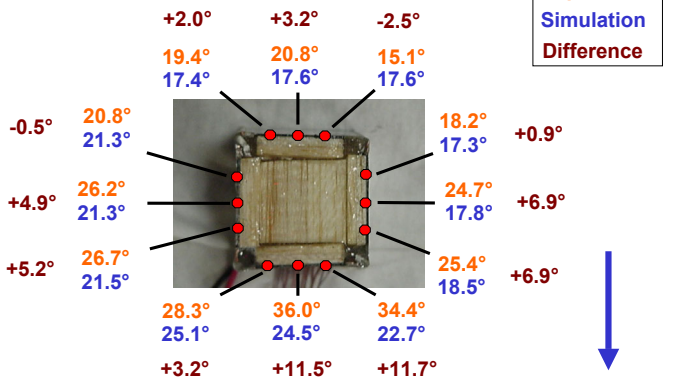

$P_{dissipated}$ = 3.692W

Q = 20cfm

Component Temperature Rises Given

Experiment
Simulation
Difference

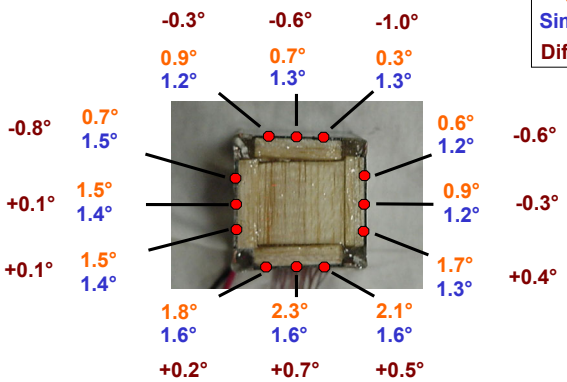

Flow Rate = 20cfm

$P_{dissipated}$ = 0.311W

Q = 20cfm

Component Temperature Rises Given

Experiment
Simulation
Difference

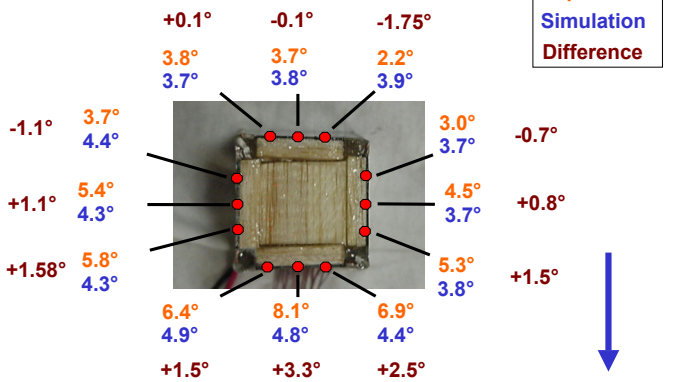

Flow Rate = 20cfm

$P_{dissipated}$ = 0.941W

Q = 20cfm

Component Temperature Rises Given

Experiment
Simulation
Difference

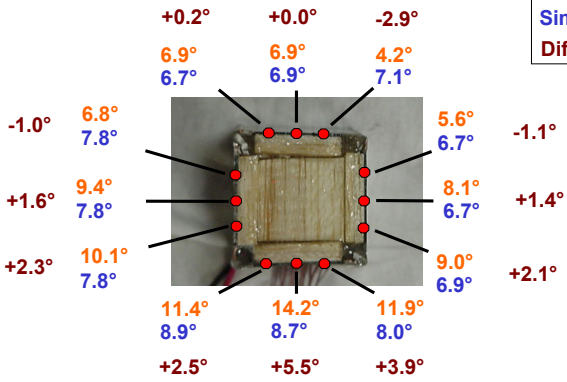

Flow Rate = 20cfm

$P_{dissipated}$ = 1.692W

Q = 20cfm

Component Temperature Rises Given

Experiment
Simulation
Difference

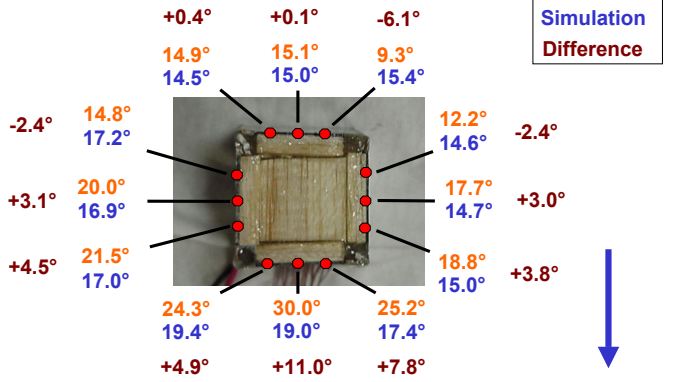

Flow Rate = 20cfm

$P_{dissipated}$ = 3.692W

Q = 20cfm (+Uncertainty)

Component Temperature Rises Given

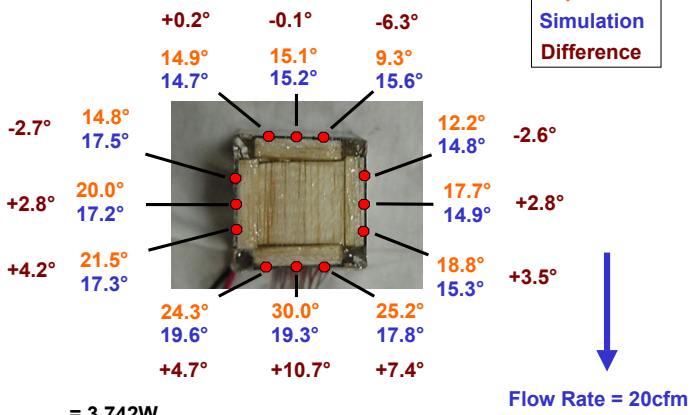

$P_{dissipated}$ = 3.742W

Q = 20cfm (-Uncertainty)

Component Temperature Rises Given

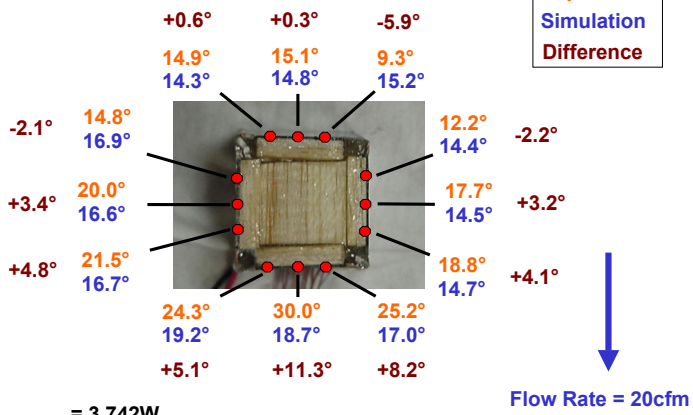

$P_{dissipated}$ = 3.742W

Appendix E – Radiation Calculations

Surface	Emissivity	Specularity	Emission	T_{MAX} (°C)	Area (mm^2)
Base	0.80	0.8		50.0	40000
PCB	0.80	0.8		70.0	36800
Fans	0.98	0.0		50.0	4800
Heat Sinks	0.40	0.8		92.0	28480
Inductor	0.20	0.1	✔	107.9	5582
PFC Output Cap	0.90	0.6	✔	73.3	3471
Boost Diode 1	0.90	0.2	✔	69.2	297
Boost Diode 2	0.90	0.2	✔	71.5	297
Boost Diode 3	0.90	0.2	✔	71.1	297
PFC MOSFET 1	0.95	0.0	✔	83.4	608
PFC MOSFET 2	0.95	0.0	✔	85.7	608
PFC Diode Bridge	0.95	0.0	✔	97.6	950
EMI Plug	0.98	0.0		50.0	3638
EMI Caps	0.90	0.2		60.2	2784
EMI Inductor	0.90	0.0	✔	73.4	4488
EMI Transformer	0.95	0.2		50.0	3124
DC/DC Input Cap	0.90	0.6	✔	68.5	3471
Transformer Winding	0.90	0.0	✔	89.1	5208
Transformer Magnets	0.90	0.4		88.8	5792
DC/DC MOSFET 1	0.90	0.0	✔	99.2	608
DC/DC MOSFET 2	0.90	0.0	✔	100.4	608
Secondary Diode 2	0.90	0.0	✔	97.5	608
Secondary Diode 1	0.90	0.0	✔	95.7	608
DC/DC Output Caps	0.90	0.6	✔	89.4	3600
Box Left Side	0.50	0.8		50.0	10000
Box Right Side	0.50	0.8		50.0	10000
Box Entrance	0.50	0.8		50.0	6400
Box Exit	0.25	0.8		50.0	6400
Box Top	0.50	0.8		50.0	40000

Evan Sewall
SURFACE INFORMATION

Model: Surface Model
Rays: 5,000,000 Rays

Surface Name	Surface Number	Area	#of Emitted Rays
Base	1	40000.0	0
PCB	2	36800.0	0
Fans	3	4800.0	0
Heat Sinks	4	28480.0	0
Inductor	5	5582.2	890452
PFC Output Capacitor	6	3470.9	556220
Boost Diode 1	7	297.4	47747
Boost Diode 2	8	297.4	47694
Boost Diode 3	9	297.4	47572
PFC MOSFET 1	10	607.8	96907
PFC MOSFET 2	11	607.8	97537
PFC Diode Bridge	12	950.0	151671
EMI Plug	13	3638.0	0
EMI Capacitors	14	2784.0	0
EMI Inductors	15	4488.3	715343
EMI Transformer	16	3124.0	0
DCDC Input Capacitor	17	3470.9	554124
Transformer Windings	18	5208.0	831861
Transformer Magnets	19	5792.0	0
DCDC MOSFET 1	20	607.8	97121
DCDC MOSFET 2	21	607.8	97029
Secondary Diode 2	22	607.8	97323
Secondary Diode 1	23	607.8	96974
DCDC Output Caps	24	3600.0	574425
Box_Left_Side	25	10000.0	0
Box_Right_Side	26	10000.0	0
Box_Entrance	27	6400.0	0
Box_Exit	28	6400.0	0
Surface28	29	0.0	0
Surface29	30	0.0	0
Box_Top	31	40000.0	0

Total number of Emitted Rays: 5000000

SURFACE TO SURFACE Dij MATRIX (5,000,000 Rays)

Surf(i)	Surf(j)	#of Absorbed Rays	Dij
5	1	24828	0.02788247
5	2	104548	0.11741003
5	3	100517	0.11288312
5	4	31642	0.03553476
5	5	148740	0.16703876
5	6	83917	0.09424090
5	7	13195	0.01481832
5	8	9700	0.01089334
5	9	5350	0.00600818
5	26	117291	0.13172074
5	27	46099	0.05177034
5	31	187344	0.21039203
6	2	124954	0.22464852
6	4	32845	0.05905038
6	5	84688	0.15225630
6	6	51938	0.09337672
6	9	7598	0.01366006
6	10	14459	0.02599511
6	11	8035	0.01444572
6	12	6275	0.01128151
6	14	8783	0.01579051
6	16	7509	0.01350005
6	26	107338	0.19297760
6	31	76723	0.13793643
7	1	137	0.00286929
7	2	10435	0.21854776
7	3	5548	0.11619578
7	4	2946	0.06170021
7	5	13294	0.27842587
7	6	3831	0.08023541
7	7	3567	0.07470626
7	8	1765	0.03696567
7	14	235	0.00492178
7	26	435	0.00911052
7	27	377	0.00789578
7	31	4655	0.09749304
8	2	11957	0.25070239
8	3	1453	0.03046505
8	4	3474	0.07283935
8	5	9746	0.20434436
8	6	6035	0.12653583
8	7	1721	0.03608420
8	8	3648	0.07648761
8	9	1009	0.02115570
8	14	342	0.00717071
8	15	252	0.00528368
8	26	1345	0.02820061
8	31	6022	0.12626326

SURFACE TO SURFACE Dij MATRIX (5,000,000 Rays)

Surf(i)	Surf(j)	#of Absorbed Rays	Dij
9	2	13080	0.27495165
9	3	683	0.01435718
9	4	3445	0.07241655
9	5	5472	0.11502565
9	6	7528	0.15824435
9	8	1011	0.02125200
9	9	3520	0.07399311
9	10	1989	0.04181031
9	14	521	0.01095182
9	15	490	0.01030018
9	26	2194	0.04611957
9	31	6882	0.14466493
10	2	30383	0.31352740
10	4	8596	0.08870360
10	5	4956	0.05114182
10	6	13569	0.14002084
10	9	1859	0.01918334
10	10	1402	0.01446748
10	11	3310	0.03415646
10	14	1619	0.01670674
10	15	2217	0.02287760
10	16	1145	0.01181545
10	26	7560	0.07801294
10	31	18036	0.18611659
11	2	29799	0.30551483
11	4	7988	0.08189713
11	5	1558	0.01597343
11	6	7627	0.07819597
11	10	3247	0.03328993
11	11	1523	0.01561459
11	12	6834	0.07006572
11	14	2733	0.02802014
11	15	5036	0.05163169
11	16	2402	0.02462655
11	26	9126	0.09356449
11	31	18658	0.19129151
12	2	41748	0.27525367
12	4	8736	0.05759835
12	5	801	0.00528117
12	6	5878	0.03875494
12	11	6676	0.04401632
12	12	2872	0.01893572
12	13	677	0.00446361
12	14	10168	0.06703984
12	15	11759	0.07752965
12	16	22731	0.14987044
12	26	9545	0.06293227
12	31	28004	0.18463648

SURFACE TO SURFACE Dij MATRIX (5,000,000 Rays)

Surf(i)	Surf(j)	#of Absorbed Rays	Dij
15	2	152217	0.21278883
15	4	9348	0.01306786
15	6	3398	0.00475017
15	11	5279	0.00737968
15	12	18102	0.02530534
15	13	24810	0.03468266
15	14	130932	0.18303387
15	15	100503	0.14049624
15	16	68620	0.09592601
15	26	83449	0.11665593
15	28	2437	0.00340676
15	31	109452	0.15300632
17	1	15232	0.02748843
17	2	117812	0.21260945
17	3	71596	0.12920574
17	4	22543	0.04068223
17	17	41575	0.07502833
17	18	38036	0.06864168
17	19	10737	0.01937653
17	20	20825	0.03758184
17	21	11568	0.02087619
17	25	91401	0.16494684
17	27	32117	0.05795995
17	31	75183	0.13567902
18	2	173083	0.20806721
18	3	9408	0.01130958
18	4	22047	0.02650323
18	17	41961	0.05044232
18	18	21535	0.02588774
18	19	60782	0.07306750
18	20	7486	0.00899910
18	21	9630	0.01157645
18	22	10342	0.01243237
18	24	37882	0.04553886
18	25	98087	0.11791273
18	31	108741	0.13072016
20	1	605	0.00622934
20	2	25753	0.26516407
20	3	8897	0.09160738
20	4	7538	0.07761452
20	17	20527	0.21135491
20	18	7152	0.07364010
20	19	1697	0.01747305
20	20	1378	0.01418849
20	21	2964	0.03051863
20	25	4730	0.04870213
20	27	1756	0.01808054
20	31	13863	0.14273947

SURFACE TO SURFACE Dij MATRIX (5,000,000 Rays)

Surf(i)	Surf(j)	#of Absorbed Rays	Dij
21	2	28827	0.29709674
21	3	1736	0.01789156
21	4	8583	0.08845809
21	17	11647	0.12003628
21	18	9280	0.09564151
21	19	8481	0.08740686
21	20	2873	0.02960970
21	21	1413	0.01456266
21	23	591	0.00609096
21	24	639	0.00658566
21	25	6826	0.07035010
21	31	15321	0.15790125
22	2	30325	0.31159130
22	4	7845	0.08060787
22	16	502	0.00515808
22	17	348	0.00357572
22	18	10026	0.10301779
22	19	6240	0.06411640
22	22	1563	0.01605992
22	23	2718	0.02792762
22	24	12566	0.12911645
22	25	7241	0.07440173
22	28	955	0.00981269
22	31	16474	0.16927140
23	2	25383	0.26175057
23	3	479	0.00493947
23	4	8873	0.09149875
23	17	1072	0.01105451
23	18	1986	0.02047972
23	19	30079	0.31017592
23	21	556	0.00573350
23	22	2770	0.02856436
23	23	2008	0.02070658
23	24	5252	0.05415885
23	25	5665	0.05841772
23	31	12068	0.12444573
24	2	170644	0.29706924
24	4	18041	0.03140706
24	13	12957	0.02255647
24	16	16530	0.02877660
24	18	34922	0.06079471
24	19	9242	0.01608913
24	22	12538	0.02182704
24	23	4737	0.00824651
24	24	101805	0.17722940
24	25	67853	0.11812334
24	28	27023	0.04704357
24	31	91807	0.15982417

Surface i	#	Surface j	#	D_{ij}	T_j	q
Inductor	5	Base	1	0.02788247	50	16
		PCB	2	0.11741003	70	83
Tmax:		Fans	3	0.11288312	50	63
107.9		Heat Sinks	4	0.03553476	92	32
		Inductor	5	0.16703876	108	180
Area:		PFC Output Capacitor	6	0.09424090	73	69
5582		Boost Diode 1	7	0.01481832	69	10
		Boost Diode 2	8	0.01089334	72	8
Emissivity:		Boost Diode 3	9	0.00600818	71	4
0.90		Box Right Side	26	0.13172074	50	73
		Box Entrance	27	0.05177034	50	29
q_e (W/m^2):		Box Top	31	0.21039203	50	117
1076				Total D_{ij}:		q_a (W/m^2):
				0.981		684
					Q_{net} (W):	2.185

Surface i	#	Surface j	#	D_{ij}	T_j	q
PFC Output Cap	6	PCB	2	0.22464852	70	159
		Heat Sinks	4	0.05905038	92	54
Tmax:		Inductor	5	0.15225630	108	164
73.3		PFC Output Capacitor	6	0.09337672	73	69
		Boost Diode 3	9	0.01366006	71	10
Area:		PFC MOSFET 1	10	0.02599511	83	21
3471		PFC MOSFET 2	11	0.01444572	86	12
		PFC Diode Bridge	12	0.01128151	98	11
Emissivity:		EMI Capacitors	14	0.01579051	60	10
0.90		EMI Transformer	16	0.01350005	50	8
		Box Right Side	26	0.19297760	50	107
q_e (W/m^2):		Box Top	31	0.13793643	50	77
735				Total D_{ij}:		q_a (W/m^2):
				0.955		701
					Q_{net} (W):	0.119

Surface i	#	Surface j	#	D_{ij}	T_j	q
Boost Diode 1	7	Base	1	0.00286929	50	2
		PCB	2	0.21854776	70	155
Tmax:		Fans	3	0.11619578	50	65
69.2		Heat Sinks	4	0.06170021	92	56
		Inductor	5	0.27842587	108	300
Area:		PFC Output Capacitor	6	0.08023541	73	59
297		Boost Diode 1	7	0.07470626	69	52
		Boost Diode 2	8	0.03696567	72	27
Emissivity:		EMI Capacitors	14	0.00492178	60	3
0.90		Box Right Side	26	0.00911052	50	5
		Box Entrance	27	0.00789578	50	4
q_e (W/m^2):		Box Top	31	0.09749304	50	54
701				Total D_{ij}:		q_a (W/m^2):
				0.989		781
					Q_{net} (W):	-0.024

Surface i	#	Surface j	#	D_{ij}	T_j	q
Boost Diode 2	8	PCB	2	0.25072390	70	177
		Fans	3	0.03046505	50	17
Tmax:		Heat Sinks	4	0.07283935	92	66
71.5		Inductor	5	0.20434436	108	220
		PFC Output Capacitor	6	0.12653583	73	93
Area:		Boost Diode 1	7	0.03608420	69	25
297		Boost Diode 2	8	0.07648761	72	55
		Boost Diode 3	9	0.02115570	71	15
Emissivity:		EMI Capacitors	14	0.00717071	60	5
0.90		EMI Inductors	15	0.00528368	73	4
		Box Right Side	26	0.02820061	50	16
q_e (W/m^2):		Box Top	31	0.12626326	50	70
720				Total D_{ij}:		q_a (W/m^2):
				0.986		763
					Q_{net} (W):	**-0.013**

Surface i	#	Surface j	#	D_{ij}	T_j	q
Boost Diode 3	9	PCB	2	0.27495165	70	195
		Fans	3	0.01435718	50	8
Tmax:		Heat Sinks	4	0.07241655	92	66
71.1		Inductor	5	0.11502565	108	124
		PFC Output Capacitor	6	0.15824435	73	116
Area:		Boost Diode 2	8	0.02125200	72	15
297		Boost Diode 3	9	0.07399311	71	53
		PFC MOSFET 1	10	0.04181031	83	34
Emissivity:		EMI Capacitors	14	0.01095182	60	7
0.90		EMI Inductors	15	0.01030018	73	8
		Box Right Side	26	0.04611957	50	26
q_e (W/m^2):		Box Top	31	0.14466493	50	81
717				Total D_{ij}:		q_a (W/m^2):
				0.984		732
					Q_{net} (W):	**-0.004**

Surface i	#	Surface j	#	D_{ij}	T_j	q
PFC MOSFET 1	10	PCB	2	0.31352740	70	234
		Heat Sinks	4	0.08870360	92	85
Tmax:		Inductor	5	0.05114182	108	58
83.4		PFC Output Capacitor	6	0.14002084	73	109
		Boost Diode 3	9	0.01918334	71	15
Area:		PFC MOSFET 1	10	0.01446748	83	13
608		PFC MOSFET 2	11	0.03415646	86	31
		EMI Capacitors	14	0.01670674	60	11
Emissivity:		EMI Inductors	15	0.02287760	73	18
0.95		EMI Transformer	16	0.01181545	50	7
		Box Right Side	26	0.07801294	50	46
q_e (W/m^2):		Box Top	31	0.18611659	50	109
871				Total D_{ij}:		q_a (W/m^2):
				0.977		734
					Q_{net} (W):	**0.083**

Surface i	#	Surface j	#	D_{ij}	T_j	q
PFC MOSFET 2	11	PCB	2	0.30551483	86	273
		Heat Sinks	4	0.08189713	92	78
Tmax:		Inductor	5	0.01597343	108	18
85.7		PFC Output Capacitor	6	0.07819597	73	61
		PFC MOSFET 1	10	0.03328993	83	29
Area:		PFC MOSFET 2	11	0.01561459	86	14
608		PFC Diode Bridge	12	0.07006572	98	71
		EMI Capacitors	14	0.02802014	60	19
Emissivity:		EMI Inductors	15	0.05163169	73	40
0.95		EMI Transformer	16	0.02462655	50	14
		Box Right Side	26	0.09356449	50	55
q_e (W/m^2):		Box Top	31	0.19129151	50	112
893				Total D_{ij}:		q_a (W/m^2):
				0.990		785
					Q_{net} (W):	**0.066**

Surface i	#	Surface j	#	D_{ij}	T_j	q
PFC Diode Bridge	12	PCB	2	0.27525367	70	206
		Heat Sinks	4	0.05759835	92	55
Tmax:		Inductor	5	0.00528117	108	6
97.6		PFC Output Capacitor	6	0.03875494	73	30
		PFC MOSFET 2	11	0.04401632	86	39
Area:		PFC Diode Bridge	12	0.01893572	98	19
950		EMI Plug	13	0.00446361	50	3
		EMI Capacitors	14	0.06703984	60	45
Emissivity:		EMI Inductors	15	0.07752965	73	60
0.95		EMI Transformer	16	0.14987044	50	88
		Box Right Side	26	0.06293227	50	37
q_e (W/m^2):		Box Top	31	0.18463648	50	108
1018				Total D_{ij}:		q_a (W/m^2):
				0.986		696
					Q_{net} (W):	**0.305**

Surface i	#	Surface j	#	D_{ij}	T_j	q
EMI Inductors	15	PCB	2	0.21278883	70	151
		Heat Sinks	4	0.01306786	92	12
Tmax:		PFC Output Capacitor	6	0.00475017	73	3
73.40		PFC MOSFET 2	11	0.00737968	86	6
		PFC Diode Bridge	12	0.02530534	98	24
Area:		EMI Plug	13	0.03468266	50	19
4488		EMI Capacitors	14	0.18303387	60	115
		EMI Inductors	15	0.14049624	73	103
Emissivity:		EMI Transformer	16	0.09592601	50	53
0.90		Box Right Side	26	0.11665593	50	65
		Box Exit	28	0.00340676	50	2
q_e (W/m^2):		Box Top	31	0.15300632	50	85
736				Total D_{ij}:		q_a (W/m^2):
				0.990		640
					Q_{net} (W):	**0.431**

Surface i	#	Surface j	#	D_{ij}	T_j	q
DC/DC Input Cap	17	Base	1	0.02748843	50	15
		PCB	2	0.21260945	70	150
Tmax:		Fans	3	0.12920574	50	72
68.5		Heat Sinks	4	0.04068223	92	37
		DC/DC Input Capacitor	17	0.07502833	69	52
Area:		Transformer Windings	18	0.06864168	89	60
3471		Transformer Magnets	19	0.01937653	89	17
		DC/DC MOSFET 1	20	0.03758184	99	37
Emissivity:		DC/DC MOSFET 2	21	0.02087619	100	21
0.90		Box Left Side	25	0.16494684	50	92
		Box Entrance	27	0.05795995	50	32
q_e (W/m^2):		Box Top	31	0.13567902	50	76
695				Total D_{ij}:		q_a (W/m^2):
				0.990		661
					Q_{net} (W):	**0.118**

Surface i	#	Surface j	#	D_{ij}	T_j	q
Transformer Windings	18	PCB	2	0.20806721	70	147
		Fans	3	0.01130958	50	6
Tmax:		Heat Sinks	4	0.02650323	92	24
89.1		DC/DC Input Capacitors	17	0.05044232	69	35
		Transformer Windings	18	0.02588774	89	23
Area:		Transformer Magnets	19	0.07306750	89	64
5208		DC/DC MOSFET 1	20	0.00899910	99	9
		DC/DC MOSFET 2	21	0.01157645	100	12
Emissivity:		Secondary Diode 2	22	0.01243237	98	12
0.90		DC/DC Output Caps	24	0.04553886	89	40
		Box Left Side	25	0.11791273	50	66
q_e (W/m^2):		Box Top	31	0.13072016	50	73
879				Total D_{ij}:		q_a (W/m^2):
				0.592		510
					Q_{net} (W):	**1.919**

Surface i	#	Surface j	#	D_{ij}	T_j	q
DCDC MOSFET 1	20	Base	1	0.00622934	99	6
		PCB	2	0.26516407	70	188
Tmax:		Fans	3	0.09160738	50	51
99.2		Heat Sinks	4	0.07761452	92	70
		DC/DC Input Capacitor	17	0.21135491	69	147
Area:		Transformer Winidngs	18	0.07364010	89	65
608		Transformer Magnets	19	0.01747305	89	15
		DC/DC MOSFET 1	20	0.01418849	99	14
Emissivity:		DC/DC MOSFET 2	21	0.03051863	100	30
0.90		Box Left Side	25	0.04870213	50	27
		Box Entrance	27	0.01808054	50	10
q_e (W/m^2):		Box Top	31	0.14273947	50	79
981				Total D_{ij}:		q_a (W/m^2):
				0.997		703
					Q_{net} (W):	**0.169**

Surface i	#	Surface j	#	D_{ij}	T_j	q
DCDC MOSFET 2	21	PCB	2	0.29709674	70	210
		Fans	3	0.01789156	50	10
Tmax:		Heat Sinks	4	0.08845809	92	80
100.4		DC/DC Input Capacitor	17	0.12003628	69	83
		Transformer Windings	18	0.09564151	89	84
Area:		Transformer Magnets	19	0.08740686	89	77
608		DC/DC MOSFET 1	20	0.02960970	99	29
		DC/DC MOSFET 2	21	0.01456266	100	14
Emissivity:		Secondary Diode 1	23	0.00609096	96	6
0.90		DC/DC Output Caps	24	0.00658566	89	6
		Box Left Side	25	0.07035010	50	39
q_e (W/m^2):		Box Top	31	0.15790125	50	88
994				Total D_{ij}:		q_a (W/m^2):
				0.992		727
					Q_{net} (W):	**0.162**

Surface i	#	Surface j	#	D_{ij}	T_j	q
Secondary Diode 2	22	PCB	2	0.31159130	70	220
		Heat Sinks	4	0.08060787	92	73
Tmax:		EMI Transformer	16	0.00515808	50	3
97.5		DC/DC Input Capacitor	17	0.00357572	69	2
		Transformer Windings	18	0.10301779	89	91
Area:		Transformer Magnets	19	0.06411640	89	56
608		Secondary Diode 2	22	0.01605992	98	15
		Secondary Diode 1	23	0.02792762	96	26
Emissivity:		DC/DC Output Caps	24	0.12911645	89	114
0.90		Box Left Side	25	0.07440173	50	41
		Box Exit	28	0.00981269	50	5
q_e (W/m^2):		Box Top	31	0.16927140	50	94
963				Total D_{ij}:		q_a (W/m^2):
				0.995		742
					Q_{net} (W):	**0.134**

Surface i	#	Surface j	#	D_{ij}	T_j	q
Secondary Diode 1	23	PCB	2	0.26175057	70	185
		Fans	3	0.00493947	50	3
Tmax:		Heat Sinks	4	0.09149875	92	83
95.7		DC/DC Input Capacitor	17	0.01105451	69	8
		Transformer Windings	18	0.02047972	89	18
Area:		Transformer Magnets	19	0.31017592	89	272
608		DC/DC MOSFET 2	21	0.00573350	100	6
		Secondary Diode 2	22	0.02856436	98	28
Emissivity:		Secondary Diode 1	23	0.02070658	96	20
0.90		DC/DC Output Caps	24	0.05418558	89	48
		Box Left Side	25	0.05841772	50	33
q_e (W/m^2):		Box Top	31	0.12444573	50	69
945				Total D_{ij}:		q_a (W/m^2):
				0.992		771
					Q_{net} (W):	**0.106**

Surface i	#	Surface j	#	D_{ij}	T_j	q
DCDC Output Caps	24	PCB	2	0.29706924	70	210
		Heat Sinks	4	0.03140706	92	28
Tmax:		EMI Plug	13	0.02255647	50	13
89.4		EMI Transformer	16	0.02877660	50	16
		Transformer Windings	18	0.06079471	89	53
Area:		Transformer Magnets	19	0.01608913	89	14
3600		Secondary Diode 2	22	0.02182704	98	21
		Secondary Diode 1	23	0.00824651	96	8
Emissivity:		DC/DC Output Caps	24	0.17722940	89	156
0.90		Box Left Side	25	0.11812334	50	66
		Box Exit	28	0.04704357	50	26
q_e (W/m^2):		Box Top	31	0.15982417	50	89
882				Total D_{ij}:		q_a (W/m^2):
				0.989		701
					Q_{net} (W):	**0.652**

The net radiation heat transfer from each component is summarized in the following table:

Component:	Heat Load (W)	Radiation Heat Transfer (W)	% Radiation
Inductor	8.0	2.2	28%
PFC Output Cap	2.0	0.1	5%
Boost Diode 1	1.5	0.0	0%
Boost Diode 2	7.0	0.0	0%
Boost Diode 3	1.5	0.0	0%
PFC MOSFET 1	5.0	0.1	2%
PFC MOSFET 2	5.0	0.1	2%
PFC Diode Bridge	14.5	0.3	2%
EMI Inductors	4.0	0.4	10%
DC/DC Input Cap	2.0	0.1	5%
Transformer Windings	15.0	1.9	13%
DC/DC MOSFET 1	10.0	0.2	2%
DC/DC MOSFET 2	10.0	0.2	2%
Secondary Diode 2	8.0	0.1	1%
Secondary Diode 1	8.0	0.1	1%
DC/DC Output Caps	3.0	0.7	23%

Vita

Evan Andrew Sewall

Evan Andrew Sewall was born in Little Rock, AR, on February 7, 1979. He grew up in Little Rock and graduated from Catholic High School for Boys in 1997. In 2001, he earned his Baccalaureate degree in Mechanical Engineering from John Brown University in Siloam Springs, AR. After a year at Virginia Tech in Blacksburg, VA, he earned his Master of Science degree in Mechanical Engineering with plans to continue graduate school at Virginia Tech in pursuit of a Doctor of Philosophy degree.